Exploring Cosmology via Large Scale Structure

WHITBOURN, JOSEPH

Durham University

Exploring Cosmology via Large Scale Structure

Author:

J. R. Whitbourn

Supervisor:

Prof. T. Shanks

A thesis submitted to Durham University
in accordance with the regulations for
admittance to the Degree of Doctor of Philosophy.

January 16, 2014

Exploring Cosmology via Large Scale Structure.

J. R. Whitbourn

Abstract

This thesis presents a study of the large-scale structure (LSS) of the Universe as evidenced in observations of the cosmic microwave background (CMB) and in galaxy redshift surveys. We first investigate several anomalies reported in the Wilkinson Microwave Anisotropy Probe (*WMAP*) CMB temperature map. In particular, we have used the *Planck* Early Data Release to test the *WMAP* beam profiles. We confirm that stacked beam profiles at Q, V and particularly at W, appear wider than expected when compared to the Jupiter beam, normalised either directly to the radio source profiles or using *Planck* fluxes. We also find that the *WMAP* source fluxes demonstrate possible non-linearity with *Planck* fluxes. Additionally, we find that the stacked Sunyaev-Zel'dovich (SZ) decrements of galaxy clusters observed by *Planck* are in agreement with the *WMAP* data. We find that there is no evidence for a *WMAP* SZ deficit as has previously been reported. We conclude that beam profile systematics can have significant effects on the CMB power spectrum with potentially important implications for Cosmology parameter fitting.

We have also mapped the local density field using K and r limited galaxy redshift distributions and number counts from the 6dF Galaxy Redshift Survey (6dFGS), Two Micron All Sky Survey (2MASS), Galaxy And Mass Assembly (GAMA) and Sloan Digital Sky Survey (SDSS) redshift surveys. We find evidence for significant galaxy underdensities in three large regions of the high latitude sky. This is in agreement with the corresponding peculiar velocities which are not compatible with recovering the CMB rest frame in the volume probed. We therefore conclude that there is some consistent evidence from both counts and Hubble diagrams for a `Local Hole' with a ≈ 150h^{-1}Mpc under-density that deeper counts and redshifts in the Northern Galactic cap suggest may extend to ≈ 300h^{-1}Mpc.

Declaration

The work described in this thesis was undertaken between 2009 and 2013 while the author was a research student under the supervision of Prof. Tom Shanks and Dr. Nigel Metcalfe in the Department of Physics at Durham University. This work has not been submitted for any other degree at the Durham University or any other University.

Several portions of this work have been used in the following publications

- **J. R. Whitbourn, T. Shanks, U. Sawangwit.**, *"Testing WMAP data via Planck radio and SZ catalogues."*,
  MNRAS, 2013, doi: 10.1093/mnras/stt1912

- **J. R. Whitbourn, T. Shanks**, *"The Local Hole revealed by galaxy counts and redshifts."*,
  MNRAS, 2013, doi: 10.1093/mnras/stt2024

All the work contained within this thesis is the authors work except where noted in the text and summarised below,

- The *WMAP* and NVSS source simulations described in Chap. 2.6.1 is due to Dr. Utane Sawangwit and is also described in Sawangwit (2011).

Acknowledgements

Nothing (much) happens in a vacuum, or indeed an empty office. So I would like thank my fellow colleagues at Durham for the help, advice, knowledge they've been so generous with. In particular, my office mates at various times; Ben Chehade, Dr. Nikos Nikoloudakis, Dr. Utane Sawangwit and Dr. Michael Hill. But also fellow students, post-docs and staff, to name a few; Dr. John Lucey, Dr. Dick Fong, Dr. Nigel Metcalfe, Dr. Peter Draper, Danny Farrow, Dr. Rich Bielby and Alan Lotts. It's been great fun.

I thank STFC and the U.K. Government for the studentship that made this Ph.D possible. It has been so rewarding to be able to dedicate myself to a four-year `big think'. It's been a privilege.

The basis of this thesis has been the use of publicly available astronomical data. I would therefore like to thank various Astronomical collaborations; *Planck*, *WMAP*, IRAM, ATCA, NVSS, PMN, GB6, SDSS, 2MASS, 6dFGS, and GAMA for making their data easily accessible.

The strongest influence on my work has undoubtedly been Prof. Tom Shanks, my supervisor, who took the time, inspiration and effort to get me this far. His passion and creativity can make anything seem possible and his impossibly wide-ranging knowledge make it seem clear.

I would also like to thank all my family for more things than I could write down. I've had the best possible grounding and all the love and support I could hope for.

Finally, I thank Sarah to whom I dedicate this thesis, O.B.V.

For you,

Sarah

Beyond the dark cartoons
Are darker spaces where
Small cloudy nests of stars
Seem to float on air.

These have no proper names:
Men out alone at night
Never look up at them
For guidance or delight,

For such evasive dust
Can make so little clear:
Much less is known than not,
More far than near.

Far Out
Philip Larkin
1959

Contents

List of Figures

List of Tables

Chapter 1 | *Introduction*

The Universe had a beginning and its ultimate destiny is an infinite unending expansion. These are the current conclusions of Cosmology, the study of the Universe as a physical object.

Our observations have revealed the Universe to be complex and highly structured. Indeed, our Sun is only one of many stars which form a far larger structure, a galaxy. Yet our own Milky-way galaxy, an `island Universe', is merely one of many such which punctuate the dark sky in our deepest sky images. In turn, galaxies themselves congregate together to form clusters and even clusters of clusters, namely `superclusters'. These dense structures are complemented by regions few in galaxies termed as voids. The resulting features in the distribution of galaxies are known as `Large Scale Structure' (LSS).

Whilst the formation, evolution and variation of individual galaxies is not fully understood, the last two decades have nevertheless seen a rapidly developing consensus develop on how to describe the Universe at the largest scales available. This `Standard Model' of Cosmology describes an expanding Universe obeying the laws of General Relativity which began with the Big Bang and then underwent Inflationary expansion. However, ordinary luminous matter is a relatively minor component in this model. The dominant form of matter does not interact with light and is hence referred to as `dark matter'. Furthermore, most of the energy-density in the current Universe is not associated with matter at all. Instead, a component called `dark energy' is attributed to the intrinsic energy of space-time itself. This curious domination of the Universe by `dark' components has lead to the Standard Model as being known as `ΛCDM'.

The ΛCDM model successfully accounts for a wide variety of cosmological tests over a large range in energy, distance and cosmic time. However, this predictive power poses fundamental physical challenges since the nature of the dark matter, dark energy and inflation field are all undetermined. This introduction aims to outline

in greater detail the fundamental ideas of the ΛCDM model of Cosmology and how they relate to the LSS. We will also describe the techniques used to generate the observational predictions that we shall go on to test.

1.1 The Expansion of the Universe

The assumption that we are typical observers and hence our observations represent a fair sample underpins the whole of Cosmology. This `Cosmological Principle' simplifies our descriptions of the Universe since it implies that there are no special or privileged directions or places. Hence the Universe, at sufficiently large scales, can be described as statistically homogeneous and isotropic. In this case the unique solution to the General Relativistic (GR) field equations is the Friedmann-Lemaitre-Robertson-Walker (FLRW) metric. In the FLRW case the path length between two points can be expressed using spherical coordinates as,

$$ds^2 = c^2dt^2 - a^2(t)d\ell^2 \tag{1.1}$$

$$ds^2 = c^2dt^2 - a^2(t)\left[\frac{dr^2}{1-kr^2} + r^2(d\theta^2 + \sin^2\theta d\phi^2)\right]. \tag{1.2}$$

Here $a(t)$ is the time dependent scale factor describing the expansion of space and k is the spatial curvature constant describing departures from a Euclidean spatial geometry. This metric successfully accounts for all current laboratory, celestial and cosmological tests of gravity. However, the most fundamental evidence for such a changing Universe comes from the observation of a `redshift'-distance relation. Redshift, z, is defined as the relative change in wavelength between time of emission and observation,

$$z = \frac{\lambda_{obs} - \lambda_{emit}}{\lambda_{emit}}. \tag{1.3}$$

The redshift can be interpreted as the change in the wavelength created by the expansion of the underlying space. In the case of the FLRW metric it is possible to derive the relation between λ and the scale factor $a(t)$ (Strauss & Willick, 1995),

$$\frac{\dot{a}}{a} = \frac{\dot{\lambda}}{\lambda}, \quad \rightarrow \quad \lambda(t) \propto a(t). \tag{1.4}$$

We can then relate the redshift to the scale factors at the time of emission, t_e, and the time of observation, t_0,

$$\frac{a(t=t_0)}{a(t=t_e)} = \frac{\lambda_{obs}}{\lambda_{emit}} = 1 + z. \tag{1.5}$$

It is also useful to define two parameters, the Hubble constant and the deceleration parameter using the spacetime interval s,

$$H_0 = \frac{1}{s}\frac{ds}{dt}\bigg|_{t=t_0} = \frac{\dot{a}}{a}\bigg|_{t=t_0}, \tag{1.6}$$

$$q_0 = -\frac{\ddot{a}a}{\dot{a}^2}\bigg|_{t=t_0}. \tag{1.7}$$

Using these quantities it is possible to approximate the `comoving' distance r to second order as (Peacock, 1999),

$$r_c \approx \frac{c}{H_0}\left(z - \frac{1+q_0}{2}z^2\right). \tag{1.8}$$

In a Universe obeying both GR and the Cosmological Principle we therefore expect to first order a linear relation between distance and redshift. It was the revolutionary efforts of Humason, Slipher and Hubble (see Trimble (2013) and Peacock (2013) for a discussion of attributation) that lead to the first observations of such a relation. These observations were foundational to the field of extra-galactic astronomy. Not only did they imply the expansion of the Universe but the distance measurements showed that the objects previously referred to as `spiral nebulae' were in fact separate and distinct galaxies as the vast distances were `extra-galactic' in scale.

Whilst the observation of a distance-redshift relation implies an expanding Universe, understanding the history of this expansion requires solutions for the scale factor $a(t)$. This can be achieved using the GR field equations in combination with the ideal fluid assumption, $p = w\rho c^2$, we then find two equations which describe the dynamics of the Universe. These are known as the Friedmann and the acceleration equations respectively.

$$H_0^2 = \left(\frac{\dot{a}}{a}\right)^2 = \frac{8\pi G\rho}{3} - \frac{kc^2}{a^2}, \tag{1.9}$$

$$\frac{\ddot{a}}{a} = -\frac{4\pi G}{3}\left(\rho + \frac{3p}{c^2}\right), \tag{1.10}$$

where the derivative of the scale factor $a(t)$ is with respect to the proper time. We will consider the Euclidean `flat' case where $k = 0$. This selects a `critical density' in the Friedmann equation that can be used to parametrise the contribution from various forms of energy density,

$$\rho_{crit} = \frac{3H^2}{8\pi G} \quad \rightarrow \quad \Omega = \sum_i \Omega_i = \sum_i \frac{\rho_i}{\rho_{crit}} = 1 \;\; (k = 0) \tag{1.11}$$

If we combine the Friedmann and acceleration equations and normalise using present day densities of the various components we can describe the evolution of density with scale factor as,

$$\dot{\rho} = -3\left(\frac{\dot{a}}{a}\right)\left(\rho + \frac{p}{c^2}\right) \quad \rightarrow \quad \rho(t) = \rho(t_0)a^{-3(1+w)}. \tag{1.12}$$

The density ρ takes contributions from all forms of energy-density hence $\rho = \sum_i \rho_i$. The three constituents to consider are non-relativistic matter: $w_m = 0$, radiation: $w_r = \frac{1}{3}$ and a cosmological constant: $w_\Lambda = -1$. If we assume no interaction between these different components and no time evolution of the equation of state parameter w then the density evolves as

$$\Omega = \sum_i \Omega_i = \frac{\Omega_m(t_0)}{a^3} + \frac{\Omega_r(t_0)}{a^4} + \Omega_\Lambda(t_0) = \left(\frac{H(t)}{H_0(t)}\right)^2 \quad (k = 0) \tag{1.13}$$

If we substitute the expressions for $\rho(t)$ into the Friedmann equation (eq. 1.9) we now have a differential equation in the scale factor $a(t)$. The three limiting cases are,

- Radiation dominated $\rightarrow a(t) \propto t^{1/2}$,
- Matter dominated $\rightarrow a(t) \propto t^{2/3}$,
- Cosmological constant dominated $\rightarrow a(t) \propto \exp(t)$.

We see here that the scale factor in all cases is increasing with time, implying the Universe is continually expanding. We also see how the Universe transitions through all these stages, since increases in $a(t)$ progressively dilute the contributions from radiation and matter due to their a^{-4} and a^{-3} scalings respectively. This leads to the Universe asymptotically approaching the cosmological constant dominated infinite unending expansion. We also note that in early times when $a(t) << 1$ it is the contribution from radiation which dominates. This earlier era in the Universe, whilst short in duration compared to the current age of the Universe, has left an important remnant that has radically influenced Cosmology, namely the Cosmic Microwave Background (CMB).

1.2 The Cosmic Microwave Background

The Universe as an object follows the principles of thermodynamics, hence its expansion implies that it must also cool. The evolution of temperature with scale factor for the adiabatic expansion predicted by inflationary models is,

$$T(z) = T_0(1 + z) \tag{1.14}$$

which implies that in early times, where $a(t) << 1$, the Universe was both smaller and hotter. Indeed, in the early universe atoms were unable to form as they were continually ionized by the sea of photons which where sufficiently hot to do so. However, the cooling due to expansion enabled the formation of atoms at a period known as recombination at $z_{rec} \approx 1100$. The Cosmic Microwave Background (CMB) radiation is the set of photons which were last scattered at this time. These photons preserve a wealth of cosmological information about this early era in their temperature and polarisation.

The temperature signal is more readily measurable and hence has been the most studied feature. The most important aspect of the temperature data is the near perfect black-body spectrum demonstrated in Fig. 1.1 where we show the CMB spectrum as measured using the *COBE*-FIRAS instrument (Fixsen et al., 1997; Mather et al., 1994). This is amongst the most compelling evidence in Cosmology for an expanding Universe as its only feasible origin is during the emergence from a hot-dense state in

the Universe's history. However, the focus of much current research is centred on the slight imperfections in this black-body spectrum, the `anisotropies'. These are important because their angular distibution reflects the depths of the gravitational well they were seeded from, and hence the scale and strength of the primordial fluctuations. The process of comparing our observations of the anisotropies to those predicted in a given cosmological model is however a complicated one. Firstly, a temperature anisotropy $\Delta T(\hat{n})$ in the pointing $\hat{n}$ is traditionally and naturally expanded using an orthogonal spherical harmonic basis,

$$\frac{\Delta T(\hat{n})}{T} = \sum_{\ell=0}^{\infty} \sum_{m=-\ell}^{m=\ell} a_{lm} Y_{lm}(\hat{n}). \tag{1.15}$$

Over a small patch of the sky we can make a flat sky approximation, in which case spherical harmonics are equivalent to standard Fourier analysis. In this limit we can then interpret the multipole moment as analogous to a wavenumber since $\theta \approx \pi/\ell$. This implies that low multipole moments correspond to large scales and vice-versa.

Since the $a_{\ell m}$ are describing an anisotropy field they have a mean of zero. For spherical harmonics this implies that the variance, denoted C_ℓ, at a multipole ℓ is

$$C_\ell = \frac{1}{2\ell+1} \sum_{m=-\ell}^{m=\ell} |a_{lm}|^2. \tag{1.16}$$

The correlation function of these temperature anisotropies depends only on the angular separation due to isotropy. Hence the Wiener-Khinchin theorem implies that the power-spectrum is the Fourier transform of the correlation function (Peacock, 1999; Szapudi et al., 2005),

$$C(\theta) = \frac{1}{T^2} \langle \Delta T(\hat{n}_1) \Delta T(\hat{n}_2) \rangle, \tag{1.17}$$

$$C_\ell = 2\pi \int_{-1}^{1} C(\theta) P_\ell(\cos\theta) d\cos\theta. \tag{1.18}$$

In a Universe where the primordial fluctuations are Gaussian distributed all information is contained within the powerspectra C_ℓ. Hence the theoretical interpretation is that the C_ℓ is the fundamental quantity from which the $a_{\ell m}$ are sampled. The fact that we have only one `terrestrial' observation of the CMB implies that we only measure $2\ell + 1$ $a_{\ell m}$ for each C_ℓ. This limit on the number of observations imposes an

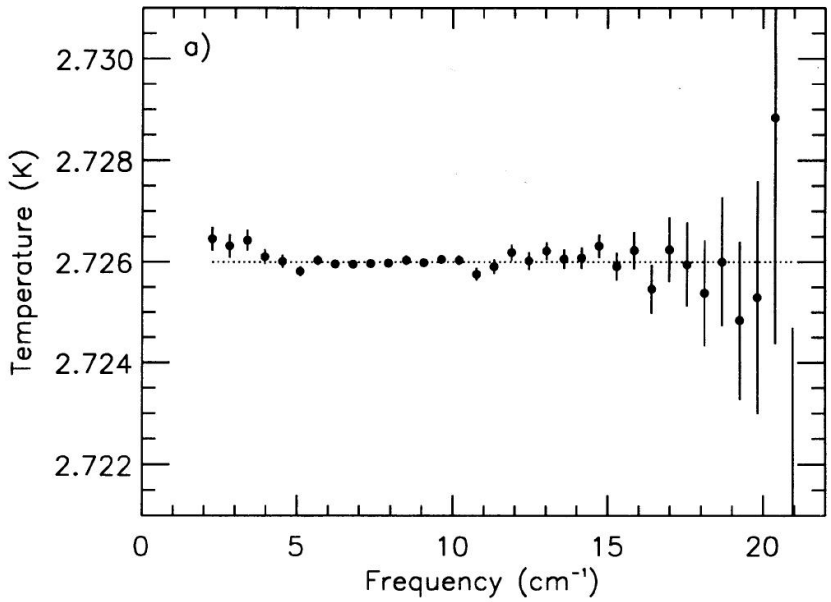

Figure 1.1: The residuals in the CMB from a black-body spectrum as a function of frequency as measured by the *COBE*-FIRAS instrument. Image credit due to Fixsen et al. (1997).

uncertainity in the measurement which is proportional to $(2\ell+1)^{-1/2}$. This becomes increasingly important at low multipoles and poses a fundamental statistical precision on our observations known as `cosmic variance'.

The estimation of the C_ℓ from a CMB experiment is an involved process. The experiment produces time ordered data (TOD) which has to be calibrated to produce a set of pointings and corresponding temperatures. This then has to be processed with a map-making algorithm to produce a single image, the `map'. There then exist a variety of methods for analysing this image to estimate the C_ℓ - for a brief overview see Jaffe (2010). Analysis of this data requires the estimation of a theoretical power spectrum in a cosmological model. This is typically done numerically, using fast Boltzmann solvers such as CAMB (Challinor & Lasenby, 1999) and CMBFAST (Seljak & Zaldarriaga, 1996). Any comparison to data C_ℓ must take account of systematic effects such as mode mixing due to incomplete sky coverage, additional smoothing due to an instrumental beam and any contaminating emission from sources such as radio galaxies.

In Fig. 1.2 we show the CMB power spectrum as reported from the first *Planck* data release (Planck Collaboration, 2013b). The peaks we observe in the C_ℓ are due to coupling between matter and radiation during the epoch of recombination. Gravity and

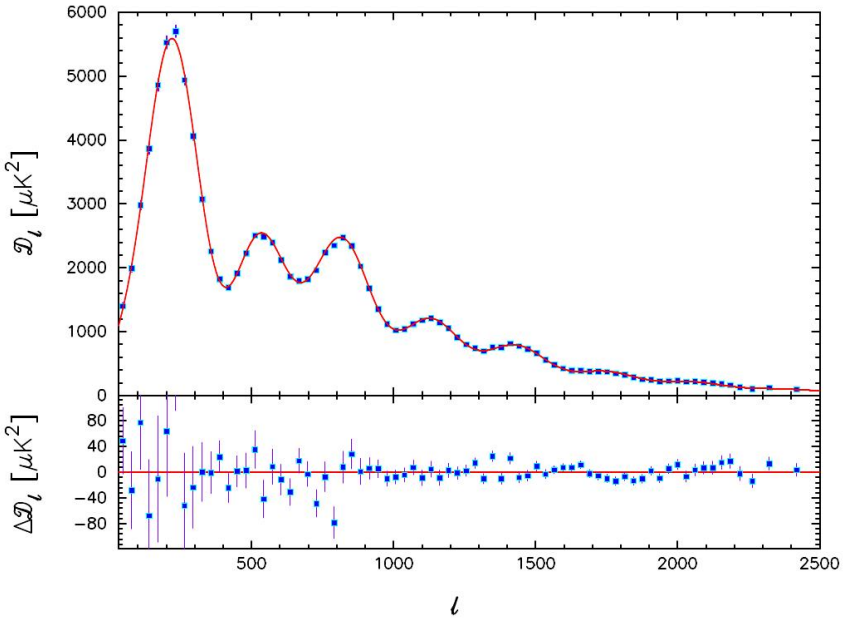

Figure 1.2: The recent *Planck* powerspectra for the first Data release. Plotted on the y-axis in the top-panel is the quantity known as `band-power' which is defined as $D_\ell = \frac{\ell(\ell+1)}{2\pi} C_\ell$. The best fit ΛCDM model is shown in red. The bottom panel displays the residuals of the data with respect to this model. Image credit due to Planck Collaboration (2013b).

radiation pressure compete and therefore cause oscillations in the matter-radiation fluid. The oscillation pattern at the time of recombination is then `frozen in' and causes peaks and troughs in the C_ℓ associated with compression and expansion respectively. The amplitudes and positions of these peaks are then determined by the energy content, spatial geometry and initial conditions of the cosmological model. For a fuller discussion of the underlying physics see Wright (2004) and Hu & Dodelson (2002). The sensitivity of the CMB power spectrum to the cosmological model is demonstrated in Fig. 1.2 where the best fit ΛCDM model is shown as the red line. This precise agreement over a wide range of multipoles is a milestone in Cosmology. Indeed, it is one of the most remarkable achievements in science that these measurements can be used to probe the nature of the initial state of the Universe, and our theories can beautifully match these observations.

1.3 Large Scale Structure & Peculiar Velocities

If the Universe were perfectly homogeneous and isotropic it would be featureless. The `gravitational collapse' paradigm attributes the existence of structure to primordial fluctuations that are seeded within the initial quantum field of the Universe and then collapse under gravity. The dynamical evolution under gravity of these fluctuations is a powerful cosmological probe because it is sensitive to the spatial geometry, matter-energy content and gravity law of the Universe. Indeed, some of the first indications of Dark Matter and the Cosmological Constant came from LSS (Zwicky, 1933; Efstathiou et al., 1990). Of particular interest is the size and amplitude of this LSS. We will therefore investigate what CMB temperature fluctuations of $1 \times 10^{-5} mK$ at $z \approx 1100$ imply for the LSS in the local $z = 0$ Universe.

Density fluctuations are typically expressed relative to the mean density $\overline{\rho}$ using a density contrast,

$$\delta(r) = \frac{\rho(r) - \overline{\rho}}{\overline{\rho}}. \tag{1.19}$$

The evolution of this density constrast is undertaken using the fluid approximation and linear theory - for a fuller review of this topic see Coles (2003) and Bernardeau et al. (2002). In short though, if we impose mass conservation, and use the force and Poisson equations, the linear growth of the density contrast can be expressed as (Carroll, 2001)

$$\delta(z) = \frac{5}{2} H_0^2 \Omega_m \frac{\dot{a}}{a} \int_0^a \left[a' H(a') \right]^{-3} da' \tag{1.20}$$

In a ΛCDM Cosmology the perturbations in the dark matter have been growing since the era of matter-radiation equality ($\Omega_m(z_{eq}) = \Omega_r(z_{eq})$ where $z_{eq} \approx 3200$). This is because dark matter sub-horizon fluctuations continue to collapse during the radiation dominated phase of the Universe since, unlike ordinary baryonic matter, they are decoupled from the radiation. The deeper gravitation wells of the dark matter act as seeds enabling enhanced gravitation collapse of the ordinary baryonic matter after decoupling of the matter and radiation components. The growth in structure from $z_{eq} \approx 3200$ to the local Universe as inferred by eq. 1.20 is therefore approximately $\delta(z = 0) \approx 2000 \times \delta(z_{eq} \approx 3200)$.

In the case of adiabatic fluctuations (as predicted by inflation) we can use the CMB to determine $\delta(z_{eq} \approx 3200)$ since temperature and density fluctuations are related as,

$$\frac{\Delta T}{T} = \frac{1}{3}\frac{\delta\rho}{\rho}. \tag{1.21}$$

Therefore, assuming fully adiabatic fluctuations and CMB temperature fluctuations $1 \times 10^{-5} mK$ we expect density fluctuations $\frac{\delta\rho}{\rho}|_{z=0} \approx 0.1$. Naively this number may seem inconsistent with the formation of present day structure which correspond to very high density contrasts. However, these structures are in fact due to `biased' non-linear structure formation occuring in the very highest overdensity regions - see Bertschinger (1998); Peacock (1999). Instead, this number describes the LSS, i.e. the typical density variations we expect. We can also use the CMB to approximate the largest spatial scales we expect this `clumpiness' in the matter to cover. This maximum fluctuation scale will be of the order of the horizon size at the time of recombination i.e. the `acoustic scale'. This is the `wavelength' of the first acoustic peak at $\ell \approx 220$ which is $\ell_a \approx 200 h^{-1} Mpc$, (Hu & Dodelson, 2002; Planck Collaboration, 2013c).

The above is only an approximate estimate of the typical scale and amplitude of LSS i.e. fluctuations of 10% at $200 h^{-1} Mpc$. However, a full theoretical treatment of this size of LSS can be provided by numerical simulations. Indeed, it is only recently that the large simulation volumes needed in order to adequately sample multiple elements of LSS have become computationally possible. The results from these Gpc scale simulation volumes suggest that the maximum size of the large scale structure is $300 h^{-1} Mpc$ (Park et al., 2012; Watson et al., 2013). These results are complemented by theoretical estimates of the size of LSS which also typically imply bounds of $300 h^{-1} Mpc$ in the ΛCDM model (Yadav et al., 2010).

1.3.1 Peculiar Velocities

Since LSS forms in the deepest gravitational potential wells we can also expect it to be associated with significant velocities. These velocities are an essential observational signal of LSS and form an important way of testing Cosmology. We can therefore make an approximate estimate of the influence of LSS on the dynamics of the Universe relative to the underlying expansion.

The velocity field in linear theory is found to have the form, Peebles (1993),

$$\underline{v}(\underline{x}) = a\frac{fH}{4\pi}\int \frac{\underline{y}-\underline{x}}{\left|\underline{y}-\underline{x}\right|^3}\delta(\underline{y})d^3y. \tag{1.22}$$

At low redshift we can usefully make the approximation $f = \frac{d\ln\delta}{d\ln a} \approx \Omega_m^{0.6}$ (Peebles, 1993). We will also make the simplifying assumption of spherical symmetry (which may well be valid for the underdense voids (Rood, 1988)). In this case the peculiar velocity solution takes the form,

$$\frac{\delta v}{H_0 r} = \frac{1}{3}\Omega_m^{0.6}\frac{\delta\rho}{\rho}. \tag{1.23}$$

It can be seen from eq. 1.23 that underdensities cause a faster local expansion, we would therefore observe a larger than expected H_0. The observational signal of a local underdensity on H_0 is,

$$\frac{\delta H}{H} = \frac{1}{3}\frac{\delta\rho}{\rho}\Omega_m^{0.6}. \tag{1.24}$$

From the estimates of the LSS we developed in Section 1.3 we therefore accordingly expect variations in H_0 of $\frac{\delta H}{H} \approx 1-2\%$. Hence we expect LSS to have a marignal effect on the expansion of the Universe in the ΛCDM model.

1.4 The ΛCDM model, successes and problems

The ΛCDM model has been remarkably successful and manages to describe[1]:

- The formation of the primordial elements (Big Bang Nucleosynthesis)
- The anisotropies we observe in the CMB
- The clustering and abundance of galaxies (LSS, the BAO and the Bullet Cluster)
- The expansion of the Universe as inferred from SNIa

This concordance is all the more impressive because a working version of the ΛCDM model can made using only seven parameters (although several extensions

[1]See Ostriker & Steinhardt 1995; Yao et al. 2006; Clowe et al. 2006; Heavens 2008.

and alternative parametrisations are possible). The spatial geometry of the Universe is described by the parameter k, the expansion of the Universe by H_0, the division of the energy content of the Universe is measured by two parameters (Ω_b, Ω_c), and two further parameters are needed to account for the scale of the initial fluctuations (σ_8) and the effect of late time physics (τ_r).

However, the Universe which the ΛCDM model describes is a Universe unfamiliar to everyday experience and indeed all our current scientific understanding. First and foremost is the Big-Bang itself, where a backward extrapolation of the expansion of the Universe would imply a singularity. The physics of this earliest moment is unclear. Shortly after the Big-Bang the Universe underwent a phase of exponential expansion which, in essence, drove the Universe from quantum-mechanical to cosmological scales. This is an important component of ΛCDM since the inflationary ultra-rapid expansion simultaneously explains why the Universe should be expected to approximate to a Euclidean spatial geometry and also obeys the Cosmological Principle that we are typical observers. However, the nature of the particle physics underpinning Inflation is unknown.

Equally, in $\Lambda CDM \approx 95\%$ of the energy-density of the current Universe is in forms that have never been observed. In particular, ΛCDM requires the majority of matter to not interact with Electromagnetic fields. This type of non-Baryonic matter is hence known as dark-matter. There exist several physically well-motivated candidates for the dark-matter and the search for the astrophysical or laboratory signal of a corresponding particle is ongoing (Bertone, 2010). This is in contrast to the Cosmological constant in ΛCDM, i.e. the intrinsic energy associated with space-time itself. The present day density of this contribution is surprising in two senses. Firstly, predictions from Quantum field theory over-predict the density ρ_Λ by many orders of magnitude. This is because ρ_Λ is sensitive to contributions from vacuum fluctuations (Carroll, 2001). Even the fact that Λ is positive is considered unlikely in alternative Physical theories such as `Supergravity', which more naturally predict negative $\Lambda$ (Witten, 2001). Secondly, our observation that $\Omega_m(a(t = t_0)) \approx \Omega_\Lambda(a(t = t_0))$ is `unnatural' in the sense that ρ_Λ remains constant whilst ρ_m decreases by a power-law. This has become known as the cosmic-coincidence problem because it implies that we are unlikely observers. Various resolutions to these 'fine-tuning' problems have been

mooted, such as Quintessence models, Cyclic Cosmologies and the Anthropic Principle (Carroll, 2001). It is currently uncertain to what extent these solutions are scientifically acceptable or themselves invoke further fine-tuning problems.

Other anomalies have been noted within the ΛCDM paradigm, and typically these focus on smaller scales or modifications to the gravity law - see Primack (2009) and Famaey & McGaugh (2012) for a discussion. However, there have also been reports of problems for ΛCDM on large scales. Although the CMB power spectrum provides powerful supporting evidence for ΛCDM it is also the case that the agreement is not perfect. In particular ΛCDM over-predicts the CMB at large scales, there is a significant hemisphere asymmetry in the CMB power, there is an unlikely alignment between the quadrupole and the octopole, and there is also a `cold-spot' which is far colder than predicted possible within ΛCDM (Planck Collaboration, 2013b,d). All these fluctuations are to some extent associated with violations of isotropy or homogeneity. However, whilst the interpretation of the anomalies is complicated by the lack of a motivating theoretical model they are of increasing importance because their detection in both *Planck* and the Wilkinson Microwave Anisotropy Probe (*WMAP*) argues against systematics errors or statistical fluctuations being responsible.

1.5 Inhomogeneity, Λ and the Cosmological Principle

The introduction of the Cosmological Constant is able to explain the relative dimming of distant SNIa since it drives an accelerating expansion of the Universe (Schmidt et al., 1998; Perlmutter et al., 1999). However, the fundamental theoretical challenges that the value of Λ cause have revived doubts about the validity of the assumption of the Cosmological Principle. This is motivated by the idea that in an inhomogeneous Universe there will be larger variations in the expansion rate than we expect on the basis of Section 1.3.1. If we were embedded within an underdensity, `a local hole', a faster expansion could possibily mimic the role of Λ in producing the dimming of the $d_{\rm l} - m$ relationship for SNIa (February et al., 2010; Krasiński, 2013). The mimicking works because it is non-obvious how to disentangle the cosmological evolution of the scale factor $a(t)$ from any possible spatial variations $a(\overline{r}, t)$. Traditionally, opposition to this complication has centred on Weinberg's theoretical result that the conservation

of photon number implies that average change in luminosity distance is zero (Weinberg, 1976). However, current views diverge on the validity and generality of this result, with some authors challenging it (Rose, 2001; Ellis et al., 1998; Kostov, 2010) and others supporting it (Kibble & Lieu, 2005). Nonetheless, in particular circumstances the perturbations to the distance modulus can be significant, such as when the source has a small angular extent (Clarkson et al., 2011), the observer is close to the void (Clifton & Zuntz, 2009), or the void has a sharp density contrast (Kostov, 2010).

A local hole inhomogeneity is a radically non-Copernican step. The observation of a nearly isotropic CMB implies that we must be very close to the centre of the hole. For a Gpc scale void this implies that our position is highly unlikely as it would only be comparable to 10^{-8} of the Hubble volume (Foreman et al., 2010). Futhermore, these models are also temporally un-Copernican as the $d_l - m$ relation is time dependent, and this therefore requires fine tuning to ensure they match the current dimming observed along our lightcone (Foreman et al., 2010). However, as some authors have noted e.g. (Moffat, 2009) there is a debate to what extent ΛCDM is non-Copernican in time, given our unlikely observation of the phase transition from a matter to Λ dominated Universe - for a review of the subject see (Clarkson & Maartens, 2010; Célérier et al., 2010; Schwarz, 2010; Heavens et al., 2011).

1.6 This Thesis

In this thesis we present results where LSS has been used to test both the ΛCDM and the underlying evidence supporting it.

In Chapters 2 and 3 we study clusters and radio sources detected in the early data release from the first ≈1.6 sky-scans of the *Planck* satellite. In particular, in Chapter 2 we test the consistency of the *Planck*-*WMAP* flux measurements of radio sources. We then go onto investigate the *WMAP* beam profile estimated using point-like radio sources and test whether this is consistent with the expectation derived from *WMAP* observations of Jupiter. In Chapter 3 we compare the *Planck* cluster data to the corresponding temperature decrements from the *WMAP* satellite in order to test a reported *WMAP* SZ deficit.

In Chapter 4 we study the local galaxy density. In particular, we use the 6dFGS,

GAMA, 2MASS and SDSS surveys to study redshift distributions, number counts and an analogue to Hubble's law to investigate a proposed local galaxy underdensity (`the local hole').

Finally, in Chapter 5 we conclude and summarise both this work and prospects for the future.

Chapter 2

Testing WMAP data via Planck radio catalogues

2.1 Introduction

CMB experiments such as *WMAP* have made significant progress in the study of the primordial temperature fluctuations. Their best fitting power spectra strongly support a spatially flat, ΛCDM, universe. This model requires relatively few parameters, yet apparently manages a compelling concordance between a variety of other cosmological data; SNIa, Large Scale Structure and Big Bang Nucleosynthesis. Although the statistical errors on these power spectra are small, this precision does not necessarily imply accuracy and there remains the potential for systematic errors to alter these conclusions.

Although radio sources are sometimes regarded as a contaminant in CMB temperature maps they prove particularly interesting in testing for systematic errors because they provide a complementary check of the beam measured by the *WMAP* team from observations of Jupiter (Page et al., 2003a; Hill et al., 2009). Jupiter has a flux of $\approx$ 1200Jy which is ≈ 3 orders of magnitude higher than radio source fluxes or CMB fluctuations. This high flux has advantages in terms of defining the wings of the beam profile but has the disadvantage that the calibrating source is much brighter than typical CMB fluctuations. Furthermore, Jupiter only checks the beam on the ecliptic whereas radio sources are spread over the sky. Sawangwit & Shanks (2010b,a) made a stacked analysis of radio point sources and found evidence for a wider beam than *WMAP* measured using Jupiter. A tentative detection of a non-linear relation between *WMAP* fluxes and ground based radio telescope fluxes was also found. A thorough analysis of possible systematics did not find an explanation and we return to these

issues later in this study. The beam profile of a CMB telescope like *WMAP* is critical because it smoothes the temperature anisotropies and therefore needs to be known accurately to produce the final power spectrum from temperature maps (Page et al., 2003a; Hill et al., 2009).

In this study we use the recent *Planck* Early Data Release and other radio source data to re-investigate both the *WMAP* radio source beam profile. The *Planck* Early Release Compact Source catalogue (ERCSC) provides the basic parameters of radio sources from the *Planck* CMB maps. We can therefore use these to compare *WMAP* and *Planck* radio source fluxes directly and also to make *WMAP* stacks centred now on the new radio source lists from *Planck*. From these stacks, the *WMAP* beam profile can be inferred. Given the higher angular resolution, lower noise and different calibration strategy for *Planck*, this comparison will allow new insight into the robustness of the *WMAP* CMB analysis.

2.2 Data

2.2.1 *Planck* Early Data Release

The *Planck* team have recently made their first release of data collected by the *Planck* satellite between 13 August 2009 and 6 June 2010 (amounting to ≈ 1.5 full sky surveys). This early data release is concerned solely with the foreground contamination in the CMB maps. In this study we shall be using the Early Release Compact Source catalogue (ERCSC).

Planck Radio Sources

The Early Release Compact Source Catalogue (ERCSC) lists all the high reliability radio sources with accurate flux determinations. The ERCSC has been quality controlled so that $\geq 90\%$ of the reported sources are reliable, $> 5\sigma$, detections and that the fluxes are determined within $\leq$30% accuracy. The catalogues are band specific and for the bands of interest ($\nu \leq 100GHz$) are created using the `PowellSnakes' method, a Bayesian multi-frequency algorithm for detecting discrete objects in a random background. Flux estimates were obtained by use of aperture photometry within a circle

of the beam's FWHM. For the case of unresolved and potentially faint point sources, the *Planck* team recommend the use of the parameter FLUX and its corresponding error, FLUX_ERR (Planck Collaboration, 2011a).

We reject any extended objects from the catalogue to maintain an unresolved sample with which to test the *WMAP* data. To do this we have used the *Planck* quality tag `EXTENDED'. This is defined by comparing the source areal profile with the 2-D *Planck* beam. An additional quality flag `CMBSUBTRACT' has also been provided, which reflects on the quality of the source detection in a map with the best estimate of the CMB removed. We minimise CMB contamination by using only CMBSUBTRACT=0 sources.

When measuring the beam profile in Section 2.5 we further cut the catalogue to ensure the best quality sample. Sawangwit & Shanks (2010a) did suggest that their faintest *WMAP* source samples were probably affected by Eddington (1913) bias. To ensure the robustness of our results against Eddington bias, we have used a $S \geq 1.1$Jy flux cut, the same limit as previously used by Sawangwit & Shanks (2010a). We have additionally rejected sources within 4° of the LMC, sources at low galactic latitude, $|b| < 5^{\circ}$ and any sources flagged by *Planck* as having high astrometric error. Finally, we tightened the *Planck* `EXTENDED' flag to remove any sources intrinsically wider than the *WMAP* beam. The *Planck* `EXTENDED' flag excludes sources with $(GAU_{FWHM\_MAJ} \times GAU_{FWHM\_MIN})^{1/2} > 1.5 \times (BEAM_{FWHM\_MAJ} \times BEAM_{FWHM\_MIN})^{1/2}$. We now ensure that the *Planck* sources are unresolved in the *WMAP* maps by imposing cuts in both the major and minor axis so that both the fitted Gaussian profiles (GAU) and the local PSF (BEAM) FWHM estimates are less than the FWHM of the *WMAP* beam in the band being studied[1].

Band and colour corrections for the *WMAP* and *Planck* fluxes have been ignored. This factor is in any case small due to the typically flat spectral indices considered (Planck Collaboration, 2011a; Wright et al., 2009). The full details of the catalogue construction and composition are described by Planck Collaboration (2011b) and briefly overviewed in Table 2.1.

[1]We relax this cut for the Q-band, here we only impose cuts on local PSF (BEAM) FWHM estimates to ensure we get a reasonable number of sources.

2.2.2 *WMAP* Data

We will be using the 7-year *WMAP* temperature maps obtained from the LAMBDA CMB resource. We work with the $N_{side} = 512$ HEALPIX maps resulting in a pixel scale of $7'$. We use the foreground unsubtracted temperature band maps for Q,V and W. Our default *WMAP* datasets are the co-added maps in Q (=Q1+Q2), V (=V1+V2) and W (=W1+W2+W3+W4). However, particularly in the W band, the increased S/N for radio source profiles obtained by using all the detector assemblies (DA's) can be regarded as a trade-off with the precision of just using the narrowest W1 (and W4) beams as previously used by Sawangwit & Shanks (2010a). In using the co-added data, the Jupiter beams have to be combined before comparison with the data. We estimate the Jupiter beam in each band by averaging the 7-year beam profiles from the various DA's, assuming the appropriate correction for pixelisation (Hinshaw et al., 2003). When working with radio point sources we use the point source catalogue mask (`wmap_point_source_catalog_mask`).

We have used the 7-year *WMAP* 5-band point source catalogue (Gold et al., 2011). These sources are detected at least the 5σ level in one *WMAP* band. For a flux density to be stated, the detection must be above the 2σ level in that band. Following Sawangwit & Shanks (2010a) we ensure that the sources are genuinely point sources by matching to the 5GHz ($\approx 4'.6$ resolution) catalogues from the Greenbank Northern sky Survey (GB6, Gregory et al. 1996), or Parkes-MIT-NRAO (PMN, Griffith & Wright 1993), surveys. The *WMAP* team also provide a 7 yr CMB-free catalogue as described by Gold et al. (2011). This catalogue has been created with the objective of detecting point sources free of boosting by CMB fluctuations. We proceed with the raw 5-band catalogue with 471 sources and a CMB-free catalogue with 417 sources.

2.3 Cross-correlation methods

2.3.1 Conversion of Radio Flux to Temperature Profiles

The *Planck* ERCSC provides us with the source flux density, error and a few parameters on the source characteristics and detection. To enable us to translate the *Planck* fluxes into *WMAP* observables we need to convert the source flux density, S_{tot}, into

Freq [GHz]	FWHM (′)	Flux Limit [Jy]
100	9.94	0.344
70	13.01	0.481
44	27.00	0.781

Table 2.1: Summary of the *Planck* bandpass parameters and the flux range of the sample we use from the ERCSC, (Planck Collaboration, 2011a).

Band	Freq [GHz]	FWHM (′)	Ω (sr)	Γ^{ff} $[\mu K Jy^{-1}]$	$g(\nu)$
W	94	12.6	$2.097{\cdot}10^{-5}$	179.3	1.245
V	61	19.8	$4.202{\cdot}10^{-5}$	208.6	1.099
Q	41	29.4	$8.978{\cdot}10^{-5}$	216.6	1.044

Table 2.2: Summary of the *WMAP* bandpass parameters taken from Hill et al. (2009) and Jarosik et al. (2011) - see text for definitions.

an observed peak Rayleigh-Jeans antenna temperature using the conversion factor $\Gamma^{ff}(\nu)$ (Page et al., 2003b),

$$\Delta T_{RJ}(0) = S_{tot}\Gamma^{ff}(\nu), \tag{2.1}$$

where

$$\Gamma^{ff}(\nu) = \frac{c^2}{2k_b\nu_e^2}\frac{1}{\Omega_{beam}(\nu)}. \tag{2.2}$$

Here ν_e is the effective frequency of the bandpass and the *ff* superscript denotes the fact that the majority of the *WMAP* sources have a spectral index $\alpha \approx -0.1$, approximately that of free-free emission.

The *WMAP* temperature maps are given in terms of the thermodynamic temperature. At the *WMAP* frequencies and CMB temperature, the Rayleigh-Jeans temperature is appreciably different from this. We therefore correct between the two temperature

differences, using eq. 2.3, where $x' = h\nu/k_b T_{cmb}$ and $T_{cmb} = 2.725$K is the monopole temperature of the CMB (Jarosik et al., 2003).

$$\begin{aligned} \Delta T_t &= \frac{(e^{x'}-1)^2}{x'^2 e^{x'}} \Delta T_{RJ}, \\ &= g(\nu) \Delta T_{RJ}. \end{aligned} \tag{2.3}$$

The observed *WMAP* temperature profiles therefore take the form,

$$\begin{aligned} \Delta T(\theta) &= \Delta T(0) b^s(\theta), \\ &= g(\nu) \Gamma^{ff} S_{tot} b^s(\theta). \end{aligned} \tag{2.4}$$

We see the beam dependence of the observed profile is twofold. The shape is dependent on the symmetrized beam profile $b^s(\theta)$ (normalised to unity at $\theta = 0^\circ$), while the scale is normalised by the beam solid angle associated with Γ^{ff}. A summary of the assumed values of $g(\nu)$ and Γ^{ff} is provided in Table 2.2.

2.3.2 Stacking Positions

The choice of coordinates to use for the radio source positions and cluster centres is important. Scatter or an offset in the centroid used in the cross-correlation could cause the stacked result to appear artifically broad or induce artifacts. However, the only sample used in this study for which astrometric errors are appreciable are the *WMAP* derived radio-source catalogues where the astrometric error in both longitude and latitude is 4′ (Chen & Wright, 2009). We mitigate for this effect by using the position of the corresponding matched 5GHz source, since these have negligble astrometric error $\mathcal{O}(10'')$ (Gregory et al., 1996; Griffith & Wright, 1993). We find no evidence for an offset between the *WMAP* and 5GHz sources and hence we are confident that astrometry error will not cause new broadening of the beam. We also note that the stacking procedure we use is dominated by the brighter objects, which typically have better astrometry.

For the *Planck* radio source catalogues we have used the *Planck* positions since these are of high astrometric quality (Planck Collaboration, 2011a). In our sample

selection we have rejected sources which the *Planck* team estimate to have relatively high astrometric errors. The effect of this selection in the 100GHz band is to ensure that $\sigma < 0'.75$ for the $S \geq 1.1$Jy sample.

2.3.3 Calculation of Profiles

Our cross-correlation/stacking procedures for measuring radio point source profiles are similar to those of Myers et al. (2004), Bielby & Shanks (2007) and then as updated by Sawangwit & Shanks (2010a). Ultimately, we shall be stacking/cross-correlating *WMAP* data around radio source positions from catalogues, particularly from the *Planck* ERCSC. To estimate a temperature profile for an individual source *j* we use,

$$\Delta T_j(\theta) = \sum_i \frac{T_{ij}(\theta) - \overline{T}_j}{n_{ij}(\theta)}, \tag{2.5}$$

where the sum is over the pixels, denoted *i*, within a circular annulus of radius θ. Here n_{ij} represents the number of pixels within the annulus and T_{ij} is the temperature recorded for the pixel *i* and source *j*. $\overline{T}_j$ is the average background temperature which can either be estimated locally in a surrounding annulus in a `photometric method' or globally - see Sawangwit & Shanks 2010a. These two background estimates make no difference in the stacked results but can make a difference for individual sources. We then stack the *WMAP*7 data by averaging $\Delta T_j(\theta)$ over the sources that have pixels within the annulus θ using the statistical average, $\Delta T(\theta) = \sum_j (1/N_\theta)\Delta T_j(\theta)$. N_θ is the number of sources that have pixels within the annulus θ and is usually constant for all except the $\theta \lesssim 4'$ bins.

We have followed Sawangwit & Shanks (2010a) in using jack-knife errors, for both the radio sources, based on 6 equal area sub-fields defined by lines of constant galactic longitude and split by the galactic equator. For $N = 6$ fields denoted *k*, the errors are,

$$\sigma^2(\theta) = \frac{N-1}{N} \sum_k^N \Big(\Delta T_k(\theta) - \overline{\Delta T}(\theta)\Big)^2, \tag{2.6}$$

where $\Delta T_k(\theta)$ is the average of the fields excluding field k. We have experimented with both alternative sub-fields and methods such as bootstrap resampling finding approximately equivalent results. In Section 2.6.1 we have used simulations to test

whether our method can robustly recover the beam profile, in doing so we find that our jack-knife errors are reasonable.

2.4 Flux Comparisons

2.4.1 Gold et al. (2011) *WMAP7* and *Planck* ERCSC

We first compare *WMAP*7 sources at Q, V, W from Gold et al. (2011) to their counterparts in the *Planck* ERCSC at 100, 70 and 44 GHz. We also compare the *Planck* fluxes in the 100GHz band to the ground-based ATCA and IRAM source fluxes previously used by Sawangwit & Shanks (2010a).

In Fig. 2.1 we first focus on the comparison of the *WMAP*7 fluxes to *Planck* and also the ground-based ATCA and IRAM sources. We only consider the matches with separation less than $2'$ to avoid any possible systematic errors associated with sources that have poor astrometry. However, our results are independent of this cut up to separations of $10'$. At high fluxes we see evidence for a systematically lower *WMAP* flux, $\approx 50\%$ above 2Jy. This non-linearity is particularly prominent in the W band, the band with the greatest angular resolution.

Since there are errors in both variables we have used the Numerical Recipes (Press et al., 1992) `*fitexy*' as our fitting routine. We find best fit logarithmic slopes of $[0.70 \pm 0.04, 0.83 \pm 0.04, 0.95 \pm 0.06]$ for the [100GHz-W,70GHz-V,44GHz-Q] comparisons. To obtain realistic errors on these fits we have linearly scaled the flux errors until we obtained a χ^2 probability of 0.5 as recommended by Press et al. (1992), for data with a dominant intrinsic dispersion.

Clearly, *Planck* and *WMAP* fluxes for sources were measured at different times. Since at least $\approx 30\%$ of the *WMAP*5 radio sources exhibit some level of variability (Wright et al., 2009), we expect and observe much larger scatter than accounted for by the estimated flux uncertainty. However, we note that the brighter *WMAP* sources are fainter than the one-to-one relation, this is in the opposite sense expected if variability was biasing faint *Planck* sources into the *WMAP* catalogue when in a bright phase.

We investigate whether variability is alternatively causing a bias due to *Planck*

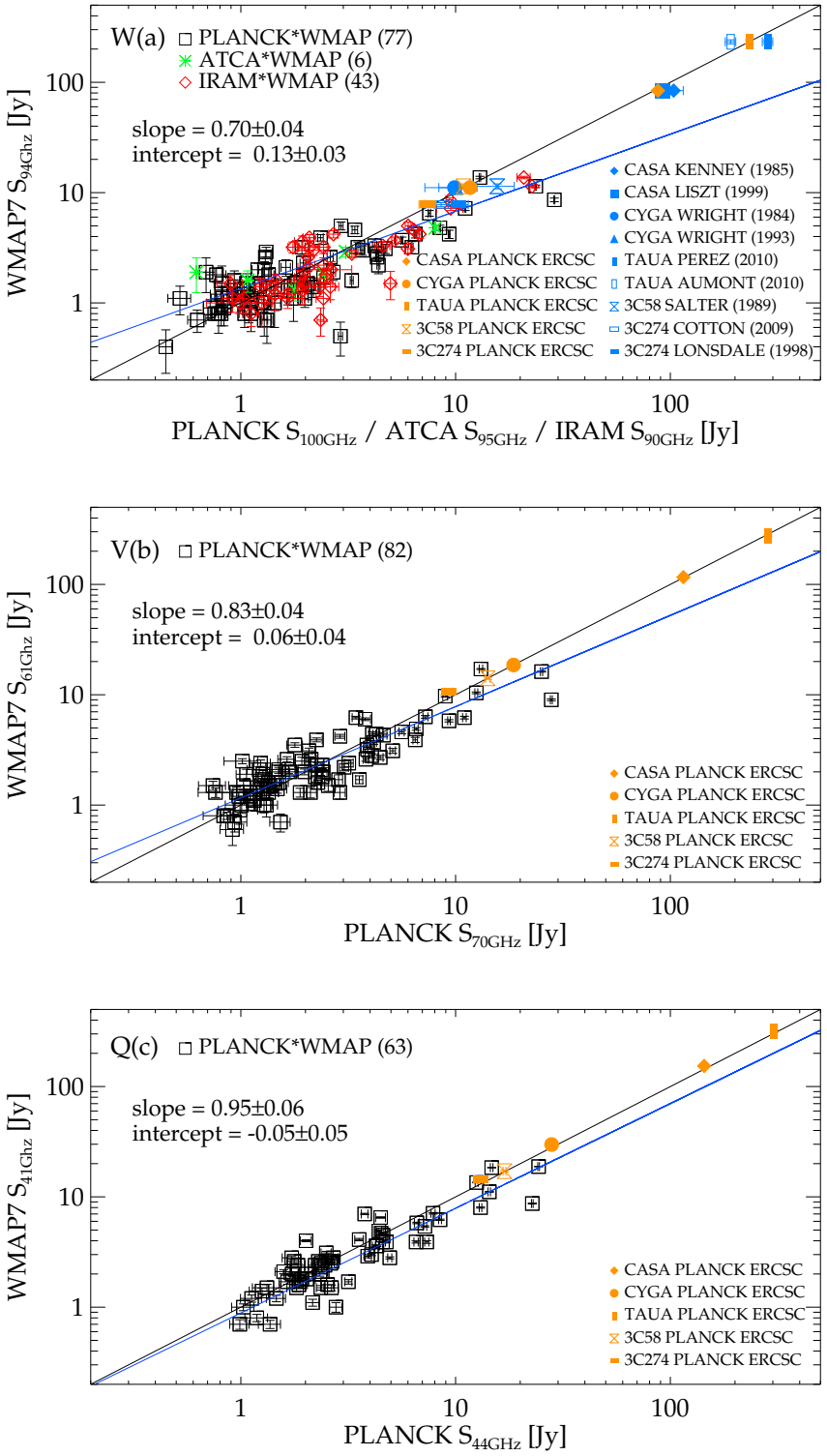

Figure 2.1: A comparison between the *WMAP*7 fluxes, *Planck* and ground based source fluxes. Also shown are the one-to-one relation (black line) and the best fit relation (blue line). Measurements of the Weiland et al. (2011) sources have been corrected to a *WMAP* epoch of 2005 and the respective *WMAP* band-centres using the Weiland et al. (2011) variability estimates and spectral indices.

dropouts by limiting the *WMAP* sample to $\geq 5\sigma$ sources. The advantage is that the *Planck* team have investigated all the *WMAP* $\geq 5\sigma$ objects that are not in the ERCSC. They conclude that for the 100GHz-W comparison the missing objects are `all' spurious and can be explained by the object having a weak or missing 5GHz ID (Planck Collaboration, 2011a). The resulting $\geq 5\sigma$ *WMAP* W-band sample of 48 sources (with $S \geq 0.8Jy$) is therefore complete in the sense of being 100% represented in the *Planck* sample with no bias due to a *Planck* dropout population. When we then repeat the *WMAP-Planck* 100GHz-W flux comparison, we find a logarithmic slope of (0.67 ± 0.05), consistent with the original result and therefore strong evidence against a highly variable source population causing dropouts that bias the *WMAP-Planck* comparison.

The disagreement between *Planck* and *WMAP* is in contrast to direct comparisons between *Planck* and ground-based ATCA/IRAM data. These instead show good agreement, as shown in Fig. 2.2 for the *Planck* 100GHz radio point sources. The best fit logarithmic slope of $[0.95 \pm 0.05]$ is statistically consistent with the one-to-one relation. However, comparing *WMAP* W-band and the ground-based ATCA/IRAM data we find evidence for non-linearity with a best fit logarithmic slope of $[0.72 \pm 0.04]$. These contrasting fits are particularly significant because the greatest *Planck-WMAP* non-linearity comes from the 100GHz-W flux comparison. Given the agreement between *Planck* and the ground-based ATCA/IRAM observations, we interpret the flux disagreement as being due to *WMAP*.

2.4.2 Further tests for bias

To test the robustness of our original comparison we have made additional bootstrap and jack-knife re-sampling tests of the *WMAP*Planck* flux-flux comparison and its error. After 1000 bootstrap resamplings we estimate logarithmic slopes of $[0.70 \pm 0.09, 0.84 \pm 0.11, 0.95 \pm 0.10]$ for the [100GHz-W,70GHz-V,44GHz-Q] comparisons. We also perform Jacknife resamplings of the *WMAP*Planck* flux-flux comparison, we estimate a logarithmic slope of $[0.70 \pm 0.10, 0.83 \pm 0.12, 0.95 \pm 0.10]$ for the [100GHz-W,70GHz-V,44GHz-Q] comparisons. These resampling results are consistent with our original samples and support the accuracy of our previous error analysis.

We have also made Monte-Carlo simulations of the flux-flux comparison. We gen-

erated samples with the same number of sources as in the real flux-flux comparison using the *WMAP* Q-band power-law distribution, $N(< S) \propto S^{-1.7}$, (Bennett et al., 2003). These fluxes are then scaled to the respective *WMAP* and *Planck* band centres on the basis of a Gaussian distribution in spectral indices, α, with mean -0.09 and standard deviation 0.176, (Wright et al., 2009). Realistic Gaussian measurement errors are then assigned as a function of flux in a manner consistent with the original *WMAP* and *Planck* samples. To include variability we start from the Wright et al. (2009) analysis of the *WMAP*5 data that measured a median rms flux variability for the 25 brightest Q-band objects of $\sigma = 0.23$ and which we therefore additionally apply to all our sources, assuming a Gaussian distribution. We then impose detection limits corresponding to the faintest source in the given band for the *WMAP* and *Planck* fluxes respectively. Finally, we compare these two flux types by measuring the best fit relation in the same way as was originally done for the *Planck*-*WMAP* comparison. After 10,000 simulations of the 100GHz-W comparison we find average logarithmic slopes and intercepts of $[0.98 \pm 0.06]$ and $[0.04 \pm 0.06]$. These results are not only in agreement with a one-to-one relation but support the errors found in our original *WMAP*-*Planck* comparison. We therefore conclude we are able to robustly recover the expected one-to-one result and hence that our comparison may be unbiased.

2.4.3 Potential contamination of *Planck* fluxes by CO emission

Planck Collaboration (2011a) have noted that the 100GHz bandpass contains the $J = 1 \rightarrow 0$ rotational CO emission line. This is a potential explanation for the flux non-linearity we report between the *WMAP* 94GHz W-band and *Planck* 100GHz bands. However, such an explanation would imply that *WMAP* and *Planck* are in agreement away from the galactic plane where CO emission is lower. However, we see no evidence for such a distinction, with galactic latitude cuts of $|b| > 5°$, $|b| > 30°$ and $|b| > 45°$ we find 100GHz-W logarithmic slopes of $[0.70 \pm 0.04]$, $[0.65 \pm 0.06]$, and $[0.72 \pm 0.08]$ respectively.

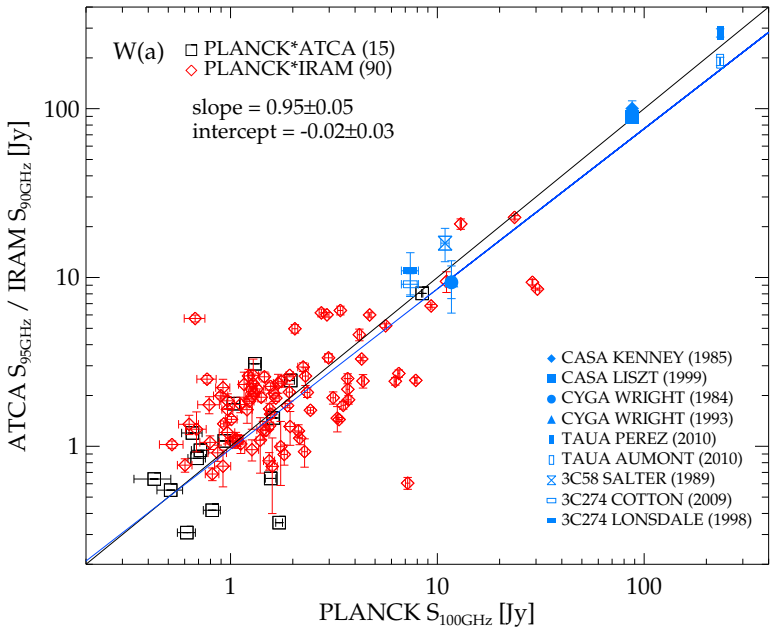

Figure 2.2: A comparison of the 100GHz *Planck* fluxes and the ground-based sources. Also shown are the one-to-one relation (black line) and the best fit relation (blue line). Measurements of the Weiland et al. (2011) sources have been corrected to a *Planck* ERCSC epoch of 2010 and the respective *Planck* band-centres using the Weiland et al. (2011) variability estimates and spectral indices.

2.4.4 Inclusion of the 5 additional Weiland et al. (2011) bright sources

Weiland et al. (2011) have made a comparison of *WMAP* fluxes of bright radio source fluxes from ground-based telescopes and claim that they support the *WMAP* flux scale. Some of the sources used are planets and have not been through the same reduction procedures as the CMB maps but five other sources, Cyg A, Cas A, Tau A, 3C58 and 3C274 have gone through the same procedures. Weiland et al. (2011) selected these sources on the basis that they were the brightest and least variable of the sources with adequate background contrast and a history of prior observation.

We now expand our flux comparisons by including these Weiland et al. (2011) sources in Fig. 2.1. We use the *WMAP* fluxes quoted by these authors and the independent ground-based fluxes that are mostly those quoted by these authors. We

see that in the W band at least, *WMAP* also underestimates the flux of these sources (blue points) and indeed Cyg A, 3C274 and 3C58 appear not inconsistent with our fitted relation. However, the underestimation for Cas A is less than predicted by extrapolating the fit to the brighter radio fluxes. If this result were to be more highly weighted then there would still be evidence for a *WMAP* flux problem, but one which now looked more like a constant offset than a scale error. However, we note that there are differences between the two ground-based observations of Cas A. Furthermore, Cas A lies close to the galactic plane ($|b| < 6^\circ$) and hence contamination might be an issue. We also note that for the brightest source, Tau-A, *WMAP* in fact overestimates the Aumont et al. (2010) measurement. However, there is a considerable difference between the Weiland et al. (2011) and Macías-Pérez et al. (2010) estimates of the *WMAP* flux. This is again likely due to the difficulty of background subtraction for a source in the galactic plane ($|b| < 6^\circ$). It may therefore be too early to infer a flux offset on the basis of these sources.

When we include the celestial sources from Weiland et al. (2011) with independent ground-based measurements[2] into the *Planck*-*WMAP* comparison we find a logarithmic slope of 0.87 ± 0.04 for the 100GHz-W comparisons. After Jack-knife and bootstrap resampling we find logarithmic slopes of 0.87 ± 0.09 and 0.86 ± 0.08 respectively for the 100GHz-W comparisons. Hence, whilst including the celestial source data changes the degree of the non-linearity, the results are still in significant disagreement with a one-to-one relation.

We finally add the *Planck* ERCSC measurements of these 5 sources to Fig. 2.1 and Fig. 2.2. This complicates the picture further since they appear to agree with the *WMAP* results more than the ground-based results. As far as we can see, the *Planck* fluxes are not calibrated via *WMAP*. If we then fit the full *Planck*-*WMAP* W band comparison we now find less evidence for a discrepancy between the two finding a 100GHz-W logarithmic slope of $[0.91 \pm 0.04]$. But just making the 100GHz-W comparison in the 3-400Jy region, the result might then again look more like a constant offset with a logarithmic slope and intercept of $[1.01 \pm 0.10]$ and $[0.16 \pm 0.12]$.

We conclude that the *WMAP* fluxes in the $S \approx 10$Jy region show systematically

[2]We do not include measurements without error estimates, this excludes the Cyg A Wright & Sault (1993) and 3C274 Lonsdale et al. (1998) measurements

lower fluxes than *Planck* and we have argued that this discrepancy is unlikely to be explained by variability, underestimated errors or inaccurate flux estimation. At lower and higher fluxes the *WMAP*-*Planck* agreement seems better, implying some non-linearity in their relative scales. If *WMAP* data are compared to ground-based data rather than *Planck*, the same discrepancy is seen at $S \approx 10$Jy and a small but significant discrepancy is seen at brighter fluxes, which would more imply a linear offset rather than a non-linearity. Similar effects are seen at Q and V but at a lower level.

2.5 *WMAP* point source profiles

2.5.1 *Planck* ERCSC radio sources

We now apply the stacking analysis of Sawangwit & Shanks (2010a) to the co-added *WMAP*7 maps, centring on the *Planck* radio point sources. *Planck* sources are selected at multiple wavebands which may be advantageous in avoiding spurious sources etc. Figs. 2.3 (a),(b),(c) are shown for completeness because these raw temperature plots demonstrate the main uncertainty in this analysis which is the accuracy of the background subtraction. We note that there is some difference between the global background and the background local to the source samples but generally this effect appears smaller in the *WMAP*7 data (eg at W) than it was in the *WMAP*5 datasets used by Sawangwit & Shanks (2010a).

Figs. 2.3 (d),(e),(f) show the same profiles now background subtracted and scaled to unity at the origin to produce $b^S(\theta)$. We have used the `photometric' subtraction to produce the radio point source temperature profile, $\Delta T_{radio}(\theta)$. For the *WMAP*7 dataset there is very little difference in the profiles resulting from global or local/photometric background subtractions.

These $b^S(\theta)$ are now compared to the *WMAP* Jupiter beam and the best fit beam to the bright *WMAP* radio source profiles found by Sawangwit & Shanks (2010a) (dashed orange line in their Fig. 2). There is again evidence that the *Planck* selected radio sources suggest a wider beam than the Jupiter beam, particularly in the W band, although the *Planck* sources lie slightly below the profile fits from Sawangwit & Shanks (2010a). We further note that the statistical significance of the deviations from the

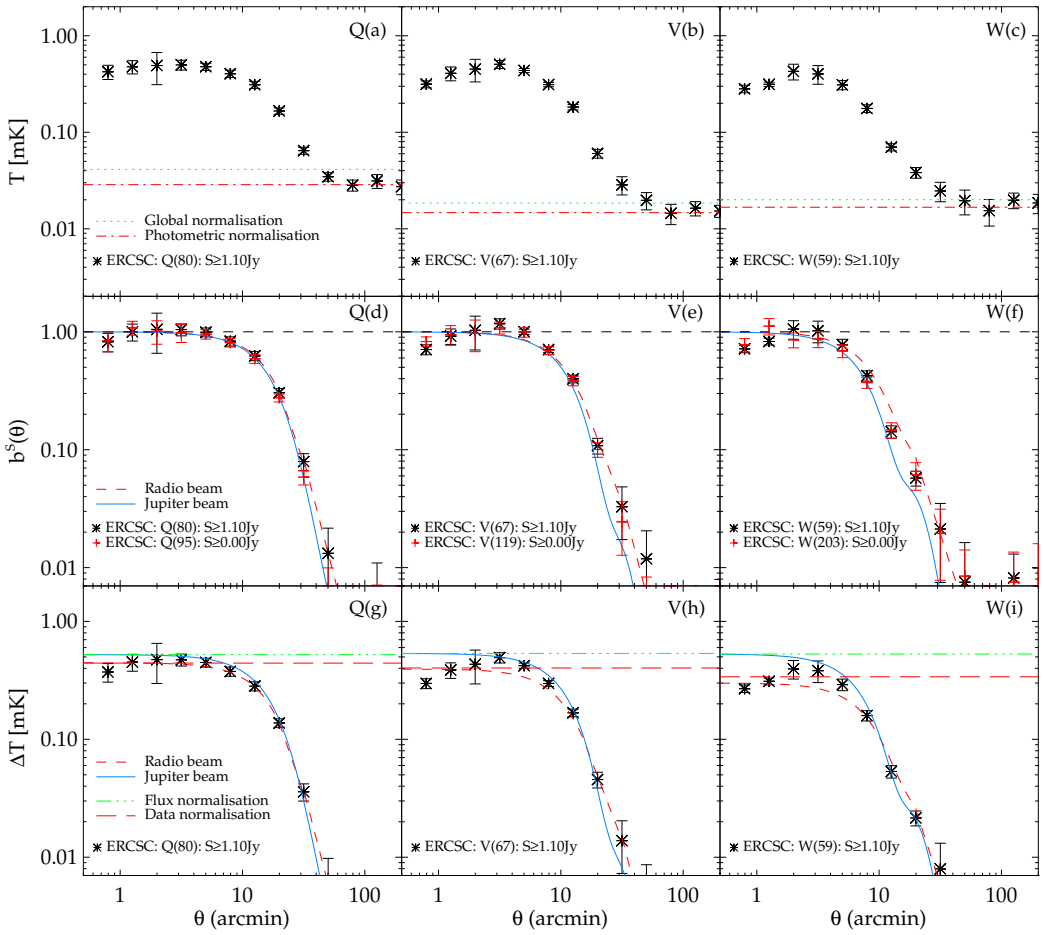

Figure 2.3: (a),(b),(c): The raw stacked *WMAP*7 [Q,V,W] temperature profiles for the *Planck* [44,70,100] GHz band sources with the global mean and photometric background temperatures of the map plotted as dashed (green, red) lines. (d),(e),(f): The photometrically subtracted, stacked and re-normalised *WMAP*7 [Q,V,W] $b^s(\theta)$ profiles for the *Planck* [44,70,100] GHz band sources. Also shown are the $b^s(\theta)$ for the Jupiter beam (blue, solid) and the radio source fit (red, dashed) of Sawangwit & Shanks (2010a). Any sensitivity to Eddington bias is shown in the profiles without the flux limit of $S \geq 1.1$Jy (lighter red, cross). (g),(h),(i): The photometrically subtracted and stacked *WMAP*7 [Q,V,W] $\Delta T(\theta)$ profiles for the *Planck* sources. Also shown are the $\Delta T(\theta)$ for the Jupiter beam (blue, solid) and the radio source fit (red, dashed) of Sawangwit & Shanks (2010a), now absolutely normalised via the *Planck* flux.

Jupiter beam for the *Planck* selected sources at $12'.6-19'.9$ is only modest at $\approx 2-3\sigma$ for the W band.

The normalisation of $b^S(\theta)$ to unity at small scales forms a further uncertainty in these beam comparisons. In Figs. 2.3 (g),(h),(i) we have applied the formalism of Section 2.3.1 and attempted to make absolute normalisations of the various model profiles, using the *Planck* ERCSC listed fluxes. We assume in turn the Jupiter profile and then the radio source profile of Sawangwit & Shanks (2010a) in calculating the resulting Γ^{ff} factor. These give respectively the blue and red lines. Hence, if the radio sources followed the Jupiter profile, for example, we should see the same peak temperature for the stacked model profile and the stacked data. We see that the *Planck* peak temperatures, particularly in the W band, tend to lie between the Jupiter profile and the previous *WMAP* bright radio source fits. These results suggest that the previous radio source fit may be too wide at $\theta > 30'$ where it is essentially an extrapolation, unconstrained by the data, and this will affect the accuracy of its absolute normalisation i.e. there is a large error in Ω_{beam}. Otherwise, the conclusion is similar to that from Figs. 2.3 (d),(e),(f) in that the *Planck* data is suggesting that the Jupiter beam is a poor fit to the radio source profiles particularly at W.

The question of Eddington bias was discussed by Sawangwit & Shanks (2010a) and has also been suggested by Schultz & Huffenberger (2012) as a possible explanation of the wide radio profiles. In terms of the *Planck* sources an Eddington bias of ≈0.02mK is required to explain our results. However our pre-selection of these sources as being point-like at *Planck* resolution and our rejection of both faint ($S < 1.1$Jy) and CMB-contaminated sources mean that it is difficult to see how Eddington bias could be affecting these results. In Figs. 2.3 (d),(e),(f) we have also presented the source sample without the $S \geq 1.1$Jy flux cut. The consistency of the full source and brighter source samples indicates that Eddington bias is not significantly affecting these samples.

2.5.2 *WMAP7* radio sources

We next repeat the analysis of Sawangwit & Shanks (2010a) using the co-added *WMAP*7 maps and source catalogue (Gold et al., 2011). The results are shown in Fig. 2.4. We see that the results again tend to lie between the Jupiter profile and the previous *WMAP*

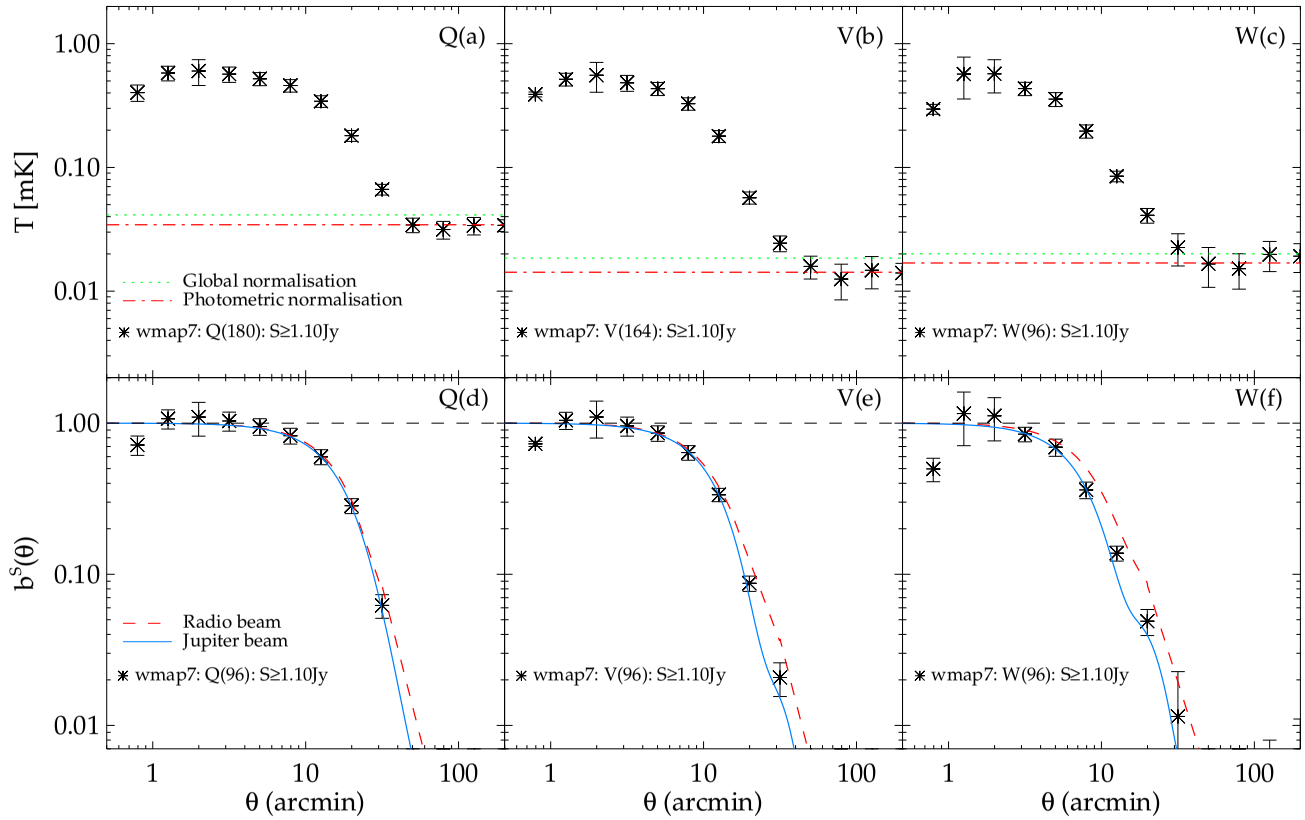

Figure 2.4: (a),(b),(c): The raw stacked *WMAP*7 [Q,V,W] temperature profiles for the *WMAP*7 sources of Gold et al. (2011) with the global mean and photometric background temperatures of the map plotted as dashed (green, red) lines. (d),(e),(f): The photometrically subtracted, stacked and re-normalised *WMAP*7 [Q,V,W] $b^s(\theta)$ profiles for the *WMAP*7 sources of Gold et al. (2011). Also shown are the $b^s(\theta)$ for the Jupiter beam (blue, solid) and the radio source fit (red, dashed) of Sawangwit & Shanks (2010a).

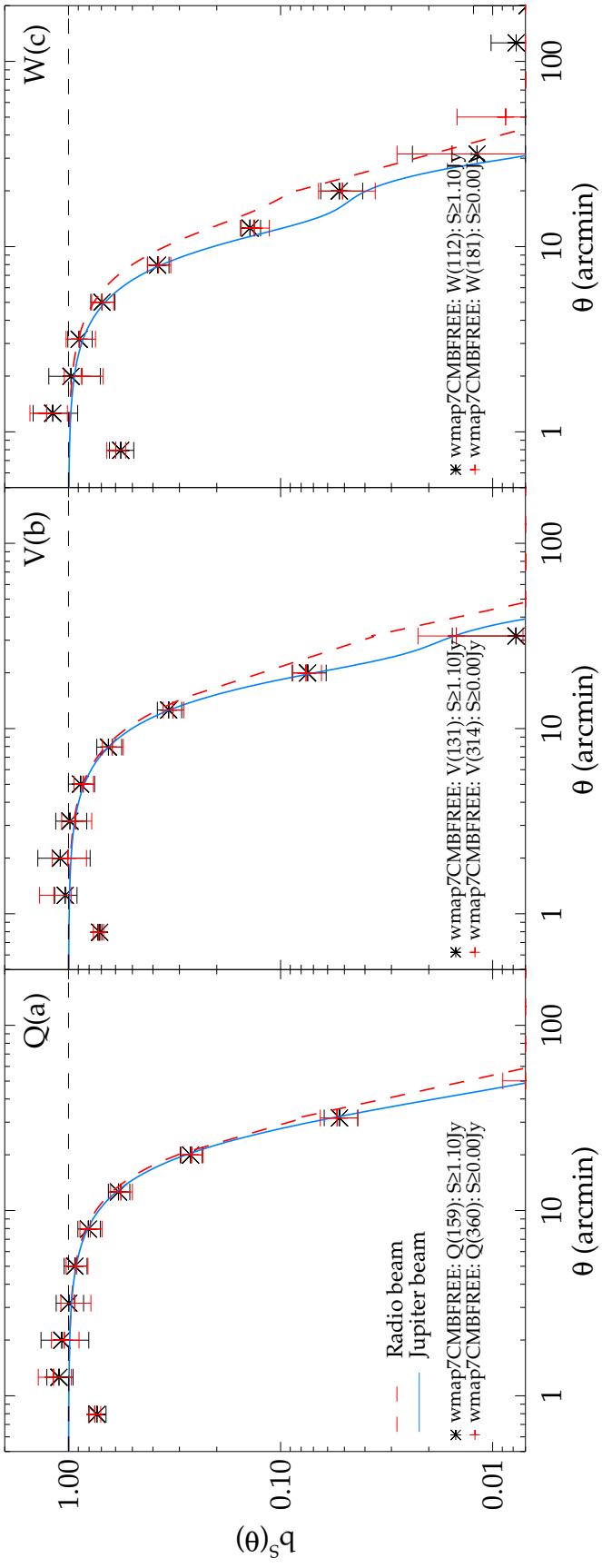

Figure 2.5: (a),(b),(c): The photometrically subtracted, stacked and re-normalised *WMAP7* [Q,V,W] $b^s(\theta)$ profiles for the CMB-free *WMAP7* catalogues of Gold et al. (2011). Also shown are the $b^s(\theta)$ for the Jupiter beam (blue, solid) and the radio source fit (red, dashed) of Sawangwit & Shanks (2010a). Any sensitivity to Eddington bias is shown in the profiles without the flux limit of $S \geq 1.1$Jy (lighter red, cross).

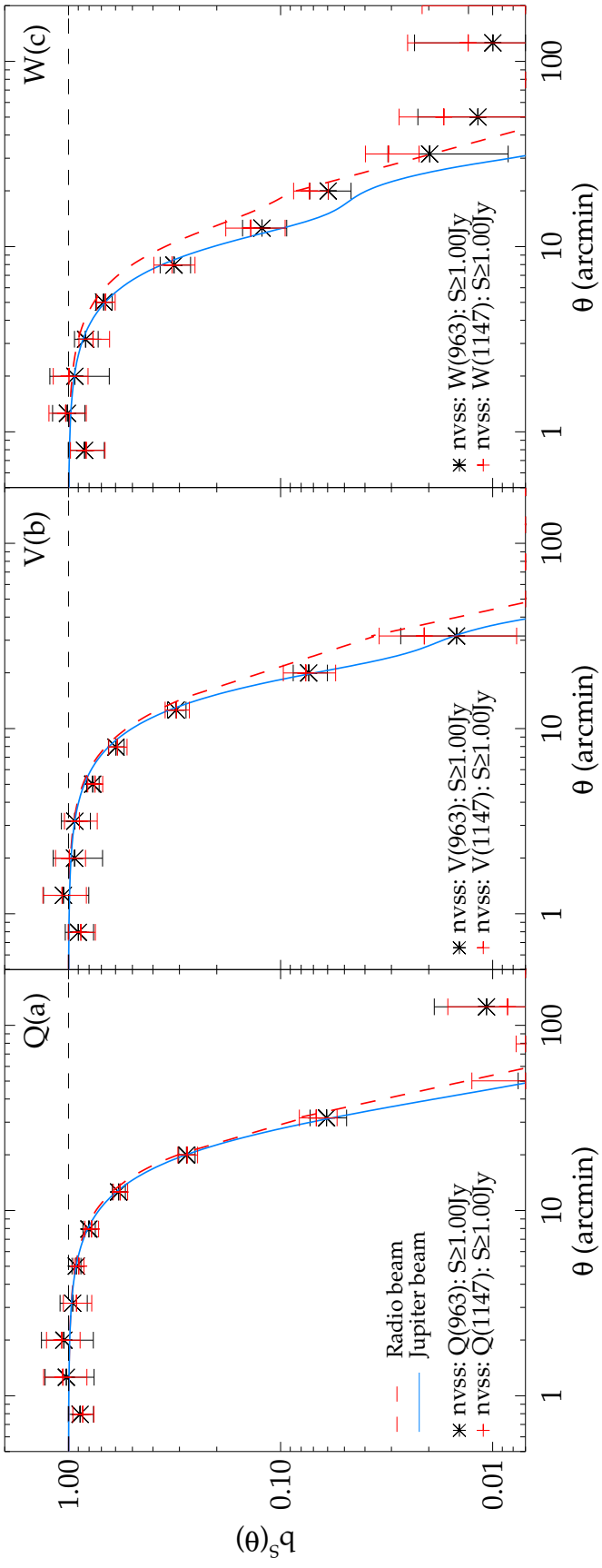

Figure 2.6: (a),(b),(c): The photometrically subtracted stacked *WMAP7* [Q,V,W] $b^s(\theta)$ profiles for the NVSS sources. Also shown are the $b^s(\theta)$ for the Jupiter beam (blue, solid) and the radio source fit (red, dashed) of Sawangwit & Shanks (2010a). Any sensitivity to close-pairs is shown in the profiles where sources with a neighbour within $< 1^\circ$ have been excluded (lighter red, cross).

bright radio source fits by Sawangwit & Shanks (2010a). This may in part be due to the *WMAP*7 profiles returning to zero at large scales more uniformly than *WMAP*5, making the differences between the photometric and global profile estimates more marginal. However, we also found that using the *WMAP*5/*WMAP*7 catalogue in the *WMAP*7/*WMAP*5 temperature maps gives profiles more consistent with the Sawangwit & Shanks (2010a) fits. We therefore attribute the difference between Fig. 2.4 and the results of Sawangwit & Shanks (2010a) to a possible systematic difference between *WMAP*5 and *WMAP*7, with perhaps a contribution from statistical fluctuations.

Following Sawangwit & Shanks (2010a) we minimised any effect of Eddington bias for this sample by pre-selecting only sources that appear in the 5GHz GB6 and PMN radio samples. We have only used 5GHz coordinates for the radio sources, with their sub-30″ accuracy to minimise any positional error in our analysis. Although Eddington bias may well be affecting the faintest *WMAP* sources, as was also noted in Sawangwit & Shanks (2010a), we have used a flux limit of $S \geq 1.1$Jy. In Section 2.6.1 we shall check for the presence of Eddington bias in this particular dataset using random simulations.

2.5.3 *WMAP*7-CMBfree radio sources

In the `CMB-free' method (Chen & Wright, 2009),*WMAP* sources are selected using the Q,V,W bands simultaneously to form an internal linear combination map (ILC) with weights chosen to cancel out the CMB anisotropy signal. Again, any Eddington bias due to CMB fluctuations should be reduced in the case of this point source catalogue. We therefore repeated our stacking analysis with the 417 QVW sources from the Gold et al. 2011 *WMAP*7 `CMB-free' catalogue - see Fig. 2.5. Overall we again see wider-than-expected profiles at W, broadly consistent with the results in Figs. 2.3, 2.4. Finally, we have also presented these results without the $S \geq 1.1$Jy flux limit, we note that the result is unchanged. This consistency is evidence for robustness of the result to Eddington bias.

2.5.4 NVSS radio sources

Point source catalogues made at significantly lower frequencies than the *WMAP* bands are unlikely to be affected by Eddington bias due to CMB fluctuations, if identification is

done independently of the *WMAP*7 point source catalogue. For example, point sources selected at 1.4 GHz will have Rayleigh-Jeans temperature $\approx 4500\times$ higher than a source with similar flux density selected at W-band (≈ 94 GHz), i.e. $T_{\rm RJ} \propto \Omega_{\rm beam}^{-1}\nu^{-2}$, whereas the rms Rayleigh-Jeans temperature due to the CMB fluctuations stays roughly the same between the two frequency bands, (Bennett et al., 2003). Therefore, we now stack co-added *WMAP*7 temperature data centred around the positions of the 1147 $S_{1.4} > 1$ Jy NRAO VLA Sky Survey (NVSS) point sources. Fig. 2.6 shows the resulting Q, V and W profiles. We see that they are consistent with those measured using *WMAP*5 total/bright sources in Fig. 2 of Sawangwit & Shanks (2010a). However, the profiles do not appear as wide as the *WMAP*5 faintest subsample despite the average flux of the NVSS sample at *WMAP* bands being $\approx 3\times$ lower.

Many of the NVSS sources are resolved into multiple components (Blake & Wall, 2002b). However, this is unlikely to cause the widening of the beam beyond $\theta \gtrsim 6'$. Here, as a precautionary measure, we shall test the beam profile measured using the NVSS by excluding any source that has neighbouring source(s) within 1°. This extra condition reduces the number of $S_{1.4} > 1.0$ Jy sources outside the *WMAP*7 `point source catalogue' mask to 963. The resulting co-added beam profiles are also shown in Fig. 2.6. We see that the beam profiles are in good agreement with the previous results.

2.6 *WMAP* and NVSS source catalogue simulations

2.6.1 Description

We made 100 Monte Carlo simulations to check our method and the robustness of the results. These simulations are due to Sawangwit (2011) who made them in the context of his test of the W1 beam in the *WMAP*5 dataset. Thus they are conservative in terms of both the errors they imply and the test of Eddington bias they make in our new context of the averaged DA's (W1-W4 in the W-band case) and the *WMAP*7 dataset. We followed the procedures described by Wright et al. (2009) - see also (Chen & Wright, 2009). For each set of simulations, $\approx 10^6$ point sources are generated with a power-law distribution, $N(> S) \propto S^{-1.7}$, at *WMAP* Q-band (Bennett et al., 2003; Chen

& Wright, 2009). Their spectral indices, α, are drawn from a Gaussian distribution with a mean -0.09 and standard deviation 0.176 as characterised by the *WMAP*5 point source catalogue (Wright et al., 2009). The flux density for each object is scaled to the centre of the other four bands using the relation $S_\nu \propto \nu^\alpha$. The source positions are then randomly distributed on the sky and each source is assigned to a pixel in a HEALPix $N_{side} = 2048$ map. For a source with flux density S_ν, the peak Rayleigh-Jeans temperature difference, $\Delta T_{RJ}(0)$, is given by eqs. 2.1, 2.2, but with the Ω_{beam} replaced by $\Omega_{pix} = 2.5 \times 10^{-7}$ sr, solid angle of a $N_{side} = 2048$ pixel. The publicly available *WMAP* maps (Section 2.2.2) are given in thermodynamic temperature (Limon, 2009). For a direct comparison with our results, we thus convert the simulated source's $\Delta T_{RJ}(0)$ to $\Delta T_t(0)$ using eq. 2.3.

Five temperature maps, one for each band, are then smoothed with the corresponding *WMAP* beam transfer function (Hill et al., 2009) before being downgraded to $N_{side} = 512$. The simulated CMB temperature map (smoothed with an appropriate beam transfer function) constructed from *WMAP*5 best-fit C_ℓ and pixel noise are then added to the source temperature maps. The pixel noise is modelled as a Gaussian distribution with zero mean and standard deviation $\sigma = \sigma_0/\sqrt{N_{\rm obs}}$, where $N_{\rm obs}$ is the number of observations in each pixel and σ_0 is given for each DA and frequency band (Limon, 2009). Here, we use the *WMAP*5 $N_{\rm obs}$ map to generate pixel noise for its corresponding band map.

2.6.2 Source Detection

Next, we applied the five-band detection technique following procedures utilised by *WMAP* team (Bennett et al., 2003; Gold et al., 2011). Firstly, the temperature maps are weighted by the number of observations in each pixel, $N_{\rm obs}^{1/2}$. The weighted map is then filtered in harmonic space by $b_\ell/(b_\ell^2 C_\ell^{\rm CMB} + C_\ell^{\rm noise})$ (e.g. Tegmark & de Oliveira-Costa, 1998; Refregier et al., 2000) where $C_\ell^{\rm CMB}$ is the CMB power spectrum and $C_\ell^{\rm noise}$ is the noise power, and b_ℓ is the beam transfer function (Hill et al., 2009). The filter is designed to suppress fluctuations due to the CMB at large scales and pixel noise at scales smaller than the beam width. We used the *WMAP*5 best-fit C_ℓ for $C_\ell^{\rm CMB}$. The $C_\ell^{\rm noise}$ are determined from pixel noise maps constructed using σ_0 and five-year

$N_{\rm obs}$ for each band as described above. We then search the filtered maps for peaks which are $> 5\sigma$. Peaks detected in any band are fitted to a Gaussian profile plus a planar baseline in the unfiltered maps for all other bands. The recovered source positions are set to the best-fit Gaussian centres in W-band. The best-fit Gaussian amplitude is converted to Rayleigh-Jeans temperature, using the relation given in eq. 2.3, and then to a flux density using conversion factors, $\Gamma^{ff}(\nu)$, given in Table 4 of Hill et al. (2009). In any given band, we only use sources that are $> 2\sigma$ and the fitted source width smaller than 2x the beamwidth, following the *WMAP* team. The number of detected sources from 100 realisations are consistent with *WMAP*5 point source analyses by Wright et al. (2009) and Chen & Wright (2009). Our simulations also recover the input power-law $N(> S)$ distribution down to the expected *WMAP*5 limit, $S \approx 1$ Jy, remarkably well - see Sawangwit (2011).

2.6.3 *WMAP* simulation results

For each simulation we applied our beam profile analysis outlined in Section 2.3 (including a flux cut of $S > 1.1$Jy). The average beam profiles derived from 100 simulations are plotted in Figs. 2.7(a)-(c) where the error bar represents their standard deviation in each angular bin. We found that even profiles as narrow as the W1-band Jupiter profile can be retrieved remarkably well out to $30'$. The estimated uncertainties using these Monte Carlo simulations are consistent with the jack-knife error estimations. Note that the Monte Carlo error converges after ≈60-70 simulations. The Monte Carlo simulations we performed here suggests that our method for recovering beam profile by stacking temperature maps around point sources is robust and the jack-knife error estimation is reliable.

2.6.4 NVSS simulation results

Although we argued above that sources (i.e. their identifications and positions) selected at NVSS frequency are robust against the CMB fluctuations compared to *WMAP* bands, our beam analysis is still carried out using *WMAP* temperature maps. As we noted, the average flux of the $S_{1.4} > 1$Jy NVSS sources in the *WMAP* bands is ≈ 3x lower than the *WMAP* sample. Therefore it is important to check whether the *WMAP*

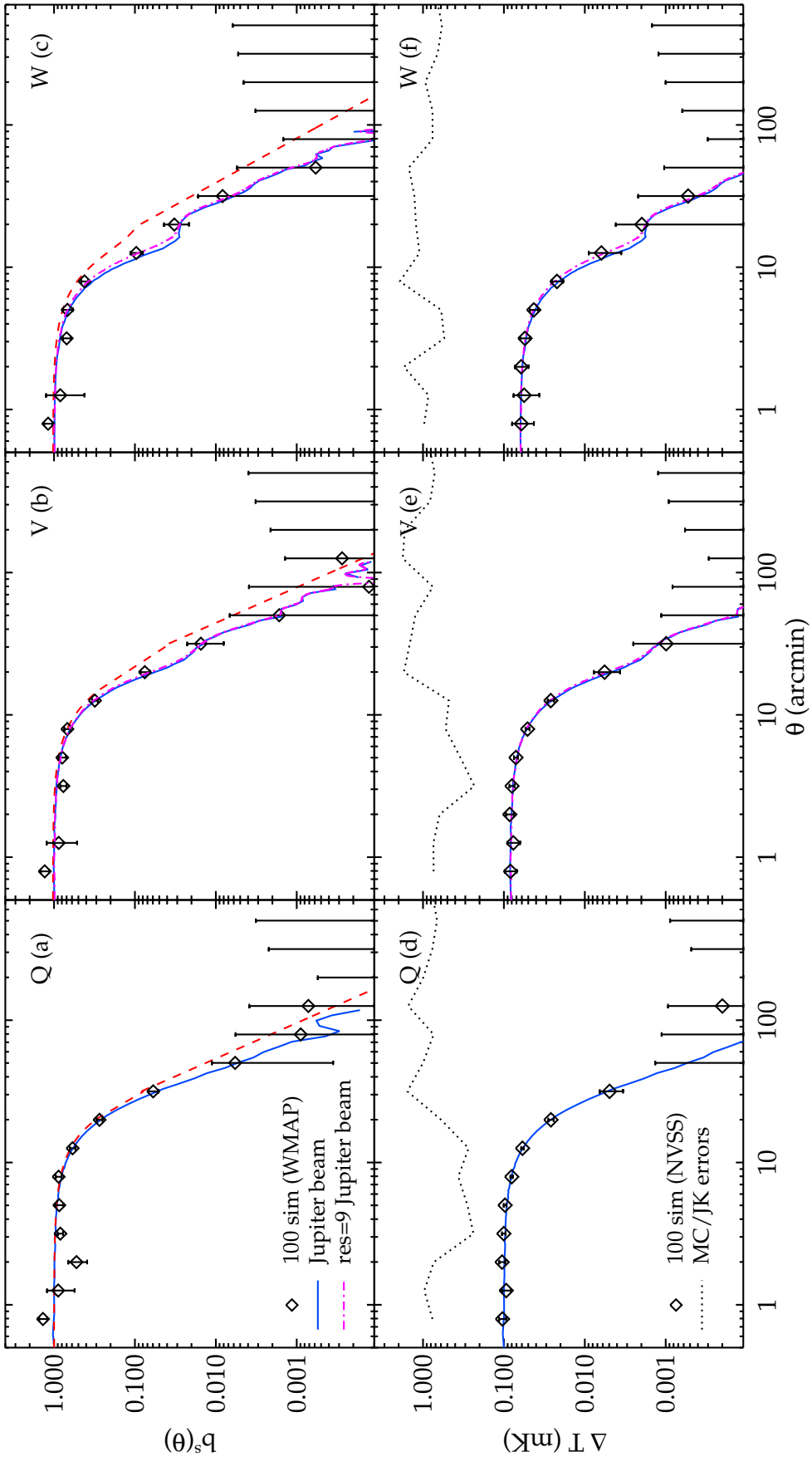

Figure 2.7: (a),(b),(c): The recovered [Q1,V1,W1] beam profiles using simulated *WMAP* point sources. The error bars are 1σ rms of 100 simulations. The effect of pixelisation on the profile measurement is shown by the magenta dot-dashed lines. (d),(e),(f): Similar to (a-c) but now using $S_{1.4} > 1$ Jy NVSS sources and without the re-normalisation. The ratios between Monte Carlo and jack-knife errors are shown as the dotted lines.

beam profiles can be robustly recovered using these NVSS sources. Again the results come from Sawangwit (2011) and were only applied to the W1 detector assembly and use *WMAP*5 data.

We again created 100 Monte Carlo simulations similar to those described above but without the five-band detection procedure since these sources are pre-detected by NVSS with high positional accuracy ($\lesssim 1''$, Condon et al. 1998). The 963 NVSS source positions are used and fluxes at 1.4 GHz are extrapolated to *WMAP* Q, V and W bands assuming a mean spectral index, α, of -0.45 in order to mimic the average flux density observed in these bands. The temperature maps are smoothed with the corresponding *WMAP* (Jupiter) beam profiles. The simulated CMB fluctuations and radiometer noise are then added to the source temperature maps as described above. For each *WMAP* band, we applied our beam profile analysis to each of the 100 simulated maps (including a flux cut of $S_{1.4} > 1$Jy). The results are shown in Figs. 2.7(d)-(f). The plot shows that with these NVSS radio sources the *WMAP* beam profiles can be robustly recovered out to $30'$ and are not affected by the source clustering consistent with the semi-empirical calculation presented in Sawangwit & Shanks (2010a). We then take the standard deviation of the 100 simulated results in each angular bin as the 1σ error. The ratio of the Monte Carlo error to the jack-knife error is shown as the dotted line in Figs. 2.7(d)-(f). The Monte Carlo and jack-knife errors are in good agreement except at scales $< 10'$ where jack-knife errors are somewhat over-estimates in Q and V bands.

The simulations suggest that when flux limited at $S \geq 1.1Jy$, the *WMAP* selected source profiles are unaffected by Eddington bias. The simulations also support the accuracy of our empirical errors. The simulations suggest the same conclusions apply when dealing with flux-limited ($S_{1.4} > 1$Jy) NVSS data.

2.7 A central deficit in radio source profiles?

A characteristic dip in the profile near the beam centre ($\theta < 2'$), a `blunting', is noticable in Fig. 2.8. This effect is consistent between samples and is robust to the choice of band and DA. Indeed, this blunting was noticed in a similar study (Schultz & Huffenberger, 2012) with their CMBfree sample in all bands (see the start of their Section

3.3). In Schultz & Huffenberger (2012) the effect was only noted but not explored in detail, it was potentially attributed to additional covariance between angular bins due to positional errors. Schultz & Huffenberger (2012) discounted any explanation due to map artifacts/method systematics as the blunting was absent in their W3 NVSS sample, as it is in ours (see Fig. 2.9(c)). However, we note that in the other *WMAP* W band DA's (1,2,4) the NVSS sample does show signs of an inner profile blunting. This suggests that positional uncertainties are not responsible for the blunting since we have stacked on the NVSS 1.4GHz position where any positional uncertainity is $\approx 1''$ (Condon et al., 1998). To further investigate the plausibility of positional offsets/errors as a possible cause for this effect we have convolved a realistic Jupiter beam with an increasingly broad Rayleigh distribution. We find that we cannot mimic the central blunting in this way, even with very large positional scatter.

To test whether the effect is an artifact due to biases in our stacking procedure or *WMAP* pointing inaccuracy we have performed a map stack at random positions. Here no positional error can be responsible for any inner profile blunting. We find a uniform distribution of points even into the inner profile. We conclude that we are uncertain of the source of this effect. However, we do also note firstly that our simulations don't show any sign of this blunting of the inner profile (Fig. 2.7). Secondly, it is unsuprising that the blunting is replicated between the different samples shown in Fig. 2.8 since they are not independent and are largely drawn from the same underlying set of sources.

2.8 Possible explanations of wide radio source profiles

We now briefly consider possible explanations for the radio source profiles we have observed. We start by accepting that in the *WMAP*7 data the profiles are less wide than found in the *WMAP*5 data discussed by Sawangwit & Shanks (2010a). We regard our best current result to come from comparison with the *Planck* radio sources where we have checked the sources against spatial extension at *Planck* resolution and also rejected any that are contaminated by the CMB. This sample still rejects the W-band Jupiter beam at $\approx 2-3\sigma$ significance at $12'.6 - 19'.9$, about the same as the rejection of the previous best fit model from Sawangwit & Shanks (2010a). Therefore it is

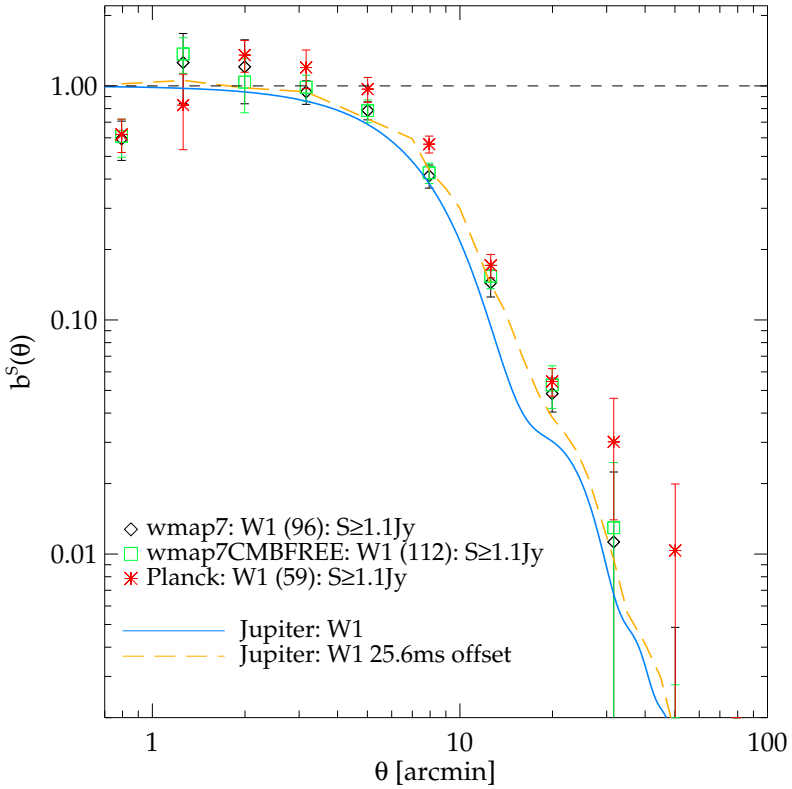

Figure 2.8: The photometrically subtracted, stacked and re-normalised *WMAP*7 [Q1,V1,W1] $b^s(\theta)$ profiles for the *Planck*, *WMAP*7 and CMB-free *WMAP*7 catalogues. Also shown are the $b^s(\theta)$ for the Jupiter beam (blue, solid) and a model showing the effect of a 25.6ms timing offset on the W1 Jupiter beam (orange, dashed) Sawangwit (2011).

not outside the bounds of possibility that the previous result may be explained by a statistical fluctuation in the *WMAP*5 data. However, we have now evaluated the rejection significance of the Jupiter beam using the full covariance matrix from our simulations, fitting in the range $4' < \theta < 20'$. For the Jupiter beam in the 7yr coadded maps we find formal rejection significances from the χ^2 distribution of [1.5×10^{-3}, 3×10^{-2}, 1.5×10^{-2}, 9×10^{-2}] for *Planck*, *WMAP*7, *WMAP*7-CMBfree and NVSS respectively. Although we note that the overlap between these samples means that these results cannot be simply combined, the *Planck* sample itself represents an $\approx 3\sigma$ rejection of the Jupiter beam. The low significance of the NVSS result simply reflects the larger errors associated with this fainter sample.

It is therefore still worth considering whether a wider beam could be related to other possible *WMAP* data problems. The first of these is the possible disagreement in *WMAP* flux comparisons with ground-based and *Planck* datasets noted by Sawangwit & Shanks (2010a) and also in this study. Certainly a non-linearity like we first fitted to Fig. 2.1 goes in the right direction to explain a flatter than expected profile. Indeed, if the addition of Cas A, Cyg A, Tau A, 3C274 and 3C58 does imply that *WMAP* fluxes are simply offset from *Planck* and ground-based fluxes, then flux comparisons would be consistent with the wide beam. A logarithmic intercept of ≈ -0.1 implies the *WMAP* flux is ≈80% of the corresponding *Planck* flux. Equally, we find the W-band *WMAP* Jupiter beam solid angle is ≈80% of the 25.6 ms timing offset derived beam's Ω_{beam}. This is in agreement with the expectation from eq. 2.1 that at fixed temperatures (ie: those provided in the *WMAP* maps) $S_{tot} \propto \Omega_{beam}$.

However, more data at brighter fluxes is needed to check if the *WMAP* flux is non-linear or simply offset with respect to other datasets. We note that Malik (2011) has used the CMB dipole to look for non-linearity in the *WMAP* temperature scale and failed to find any evidence for such an effect.

The second possible explanation for the wider than expected radio source profiles focused on the possibility that there was a timing offset between the *WMAP* antenna pointing and temperature data, as proposed by Liu & Li (2011). As well as causing effects at large scale due to a wrongly subtracted dipole, this scan pattern offset would cause a wider beam profile - see Moss et al. 2011a. Sawangwit (2011) have calculated the beam pattern that a 25.6 ms timing offset would cause in the W band.

The effect is approximately equivalent to a $3'$ Gaussian broadening of the beam. The calculation assumes the W1 Jupiter beam and takes into account its initial asymmetry on the sky. After creating simulated *WMAP* TOD that include point sources distributed in ecliptic latitude and then applying mapmaking to these data, Sawangwit (2011) found the azimuth averaged beam profiles shown in Fig. 2.8 for both zero timing offset and the 25.6ms timing offset with the latter giving a reasonable fit to the *Planck* data. More details are presented by Sawangwit (2011). These include further results based on using the dependence of beam shape with ecliptic latitude to try and determine the timing offset which marginally prefer zero timing offset. We note that Roukema (2010) made similar tests based on bright *WMAP* sources and found no evidence for a timing offset at the map-making stage. On the other hand, Liu & Li (2011) checked between offsets by minimising dipole residuals and found strong evidence for a non-zero offset - see Sawangwit et al (in prep). We note that the *WMAP* team have indicated that they use a timing offset of zero in which case the above agreement would simply represent a coincidence.

2.9 Discussion

The main criticism that was made of the previous results of Sawangwit & Shanks (2010a) was that the wide *WMAP* radio source profiles may be caused by Eddington bias (Eddington, 1913). Essentially, low S/N sources detected in the *WMAP* data may be contaminated by upwards CMB fluctuations and not balanced by downwards fluctuations. This could explain the wider than expected profiles, particularly at faint fluxes.

There may be some evidence for Eddington bias in the faintest *WMAP*5 W band source sub-sample that was initially used by Sawangwit & Shanks (2010a). However, it was because of this the faintest sources were not used in Sawangwit & Shanks (2010a) fits of the beam profile and that a flux limit of $S \geq 1.1$Jy has been used in calculating our radio source profiles. We also note that the *Planck* sources show the wider beam independent of whether the CMBSUBTRACT flag applies. We further note that we have restricted the *Planck* sources to have a FWHM strictly less than the *WMAP* W band beam profile width and find a wider than expected beam profile for these clearly

point sources. *WMAP* sources selected from a `CMB-free' map and NVSS selected sources at low frequency also show the same wider than expected beam.

Furthermore, we have also run Monte Carlo re-simulations of the source detection, producing artifical source catalogues extracted from simulated CMB maps. Here, after applying the same cross-correlation technique as for the data, the *WMAP* beam was recovered as input (see Fig. 2.7), again arguing that these sources are little affected by Eddington bias.

The *Planck* data also confirms the non-linearity of *WMAP* fluxes, particularly in the W band, in the range previously used. Decreasingly non-linear effects are also seen at Q and V. But when ground-based and *Planck* data for the bright Weiland et al. (2011) sources are included in these comparisons the evidence for non-linearity becomes less and it could still be that the discrepancy corresponds more to a constant offset.

Given that the beam profile widening is smaller in the *WMAP*7 data than in *WMAP*5, a scan pattern timing offset as discussed by Liu & Li (2011) becomes a more plausible explanation for this effect. We have seen that the effect, originally invoked as an explanation for the alignment of the low order multipoles with the ecliptic, also provides a reasonable fit to the W band beam profiles - see Fig. 2.8.

We note the Integrated Sachs-Wolfe (ISW) effect is a negligible effect for radio sources, as observed by (Nolta et al., 2004; Sawangwit et al., 2010) where it is shown to be $\approx 0.3\mu K$ effect. It is therefore highly unlikely to cause any bias to our radio source analyses.

We have also compared our results to those of Schultz & Huffenberger (2012). We compare our results directly to theirs in Fig. 2.9. The *WMAP*7 W3 graph they use as an example is significantly wider than any profile shown by Sawangwit & Shanks (2010a) or here. This is because they have used a sample with no cut at all in terms of significance of detection or flux and clearly these data will be strongly affected by Eddington bias. We repeat that at the flux limits used here, the simulations show no sign of such bias and so we are confident that this criticism does not apply to our results. We note that there are additional quality cuts that Schultz & Huffenberger (2012) have made with respect to our work, such as an expanded mask and a culling of close pairs. However, we find that our results are unchanged when we apply them as well. We find that their *WMAP*7-CMBfree and NVSS beam profiles are very comparable

to ours for the W3 band and they are wider than the Jupiter profile as can be seen. Schultz & Huffenberger (2012) suggest that the *WMAP*7-CMBfree profiles are wider due to errors on the radio source positions. However, their assumed positional errors may be overestimates for their stacked radio source profiles since the stacks are weighted towards the brighter radio sources which have more accurate positions. The fact that we are using 5GHz GB6 and PMN positions accurate to sub-$0.'5$ accuracy in the *WMAP* case and obtain *WMAP*7-CMBfree profiles consistent with Schultz & Huffenberger (2012) suggests that positional errors cannot be the explanation. The main difference with the NVSS results of Schultz & Huffenberger (2012) is their larger errors. Our NVSS sample is ≈ 4x larger than theirs due to our 1.4GHz flux limit of 1Jy compared to their 2Jy limit, this (as well as our larger binning) explains most of the difference in errors. Otherwise the results appear entirely consistent.

We finally show in Fig. 2.10 the effect wide *Planck* radio source profiles (see Fig. 2.3f) has on the *WMAP* W1/W2 C_l. We take here the model with the 25.6ms timing offset that gave a reasonable fit to the data in Fig. 2.8. Otherwise without the model, we would need to extrapolate a fit out to large angles. Then debeaming the raw W1/W2 C_l from PolSpice (Szapudi et al., 2001) via eqs. 1,2 of Sawangwit & Shanks (2010a), we see that the C_ℓ shows a modest increase in amplitude at $\ell <$400, with a larger increase at $\ell >$400. This reflects where the Jupiter and timing offset beam are different. At $\ell <$400 there is very little difference between the Jupiter and the timing offset beam. We note that this region is essentially unconstrained by the radio source profiles. So the lack of change to the first acoustic peak is tied to the specific details of the timing offset model. A different model could give significantly different results and therefore *WMAP*7 first acoustic peak's amplitude and position relies heavily on the accuracy of the observed Jupiter beam beyond 30′ scales, which is untested by our observations. However, it should be noted that although the timing-offset model reproduces the general form of the Silk damping tail, in detail there are significant differences at $\ell > 500$ between this and the ground based observations from the South Pole Telescope (SPT, Keisler et al. (2011)) and the Atacama Cosmology Telescope (ACT, Das et al. (2013)). We also note that it has been reported that there is agreement between *WMAP* and these ground-based observations (Hajian et al., 2011; Keisler et al., 2011). Indeed, we also see a similar disagreement between the timing-offset model and

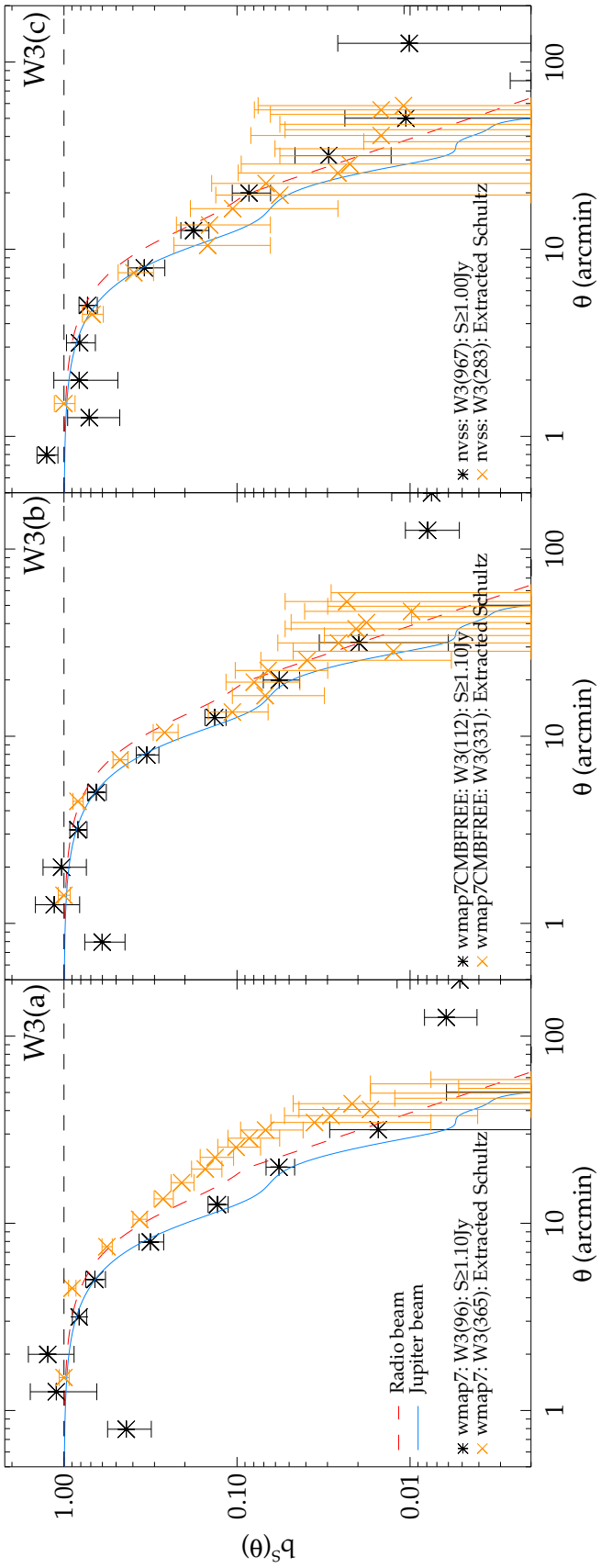

Figure 2.9: (a),(b),(c): The photometrically subtracted stacked *WMAP7* W3 $b^s(\theta)$ profiles for *WMAP7*, *WMAP7* CMB-free and NVSS catalogues as compared to the corresponding W3 results from Schultz & Huffenberger (2012) as taken from their Fig. 5. Also shown are the $b^s(\theta)$ for the Jupiter beam (blue, solid) and the radio source fit (red, dashed) of Sawangwit & Shanks (2010a).

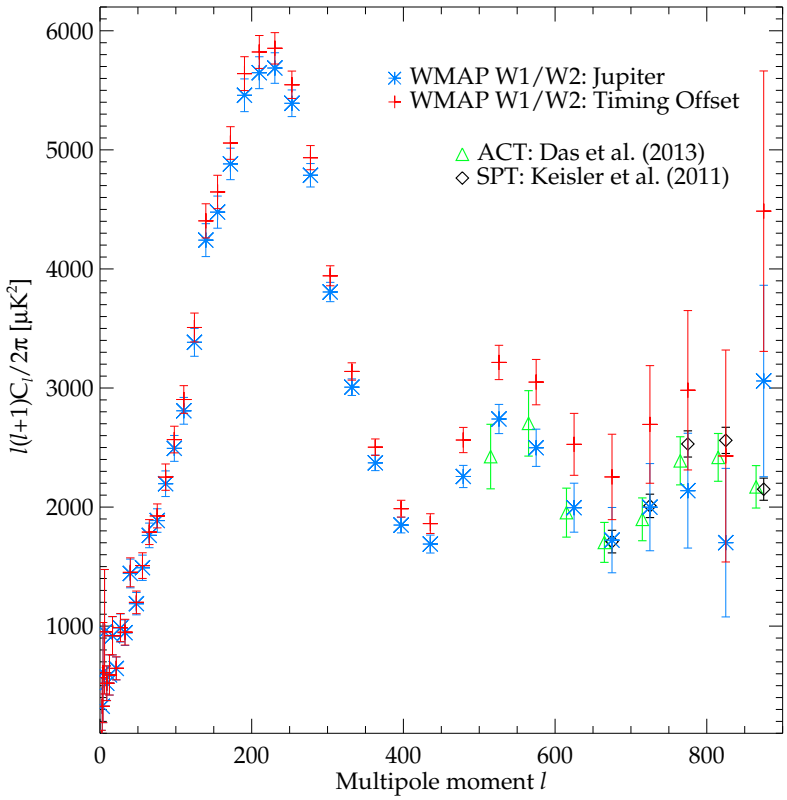

Figure 2.10: The *WMAP* W1/W2 C_l result from debeaming with the Jupiter beam (blue, stars) as compared to the result from debeaming with the timing offset derived beam from Sawangwit (2011) and also shown in Fig. 2.8 (red, crosses).

the recently released *Planck* CMB power spectrum (Planck Collaboration, 2013b). But the main point of Fig. 2.10 is simply to illustrate that such a beam profile can affect the CMB power spectrum.

2.10 Conclusions

We have investigated the beam profile of *WMAP* by comparing beam profiles from radio sources with the Jupiter beam profile. We have compared sources from *Planck*, *WMAP*, *WMAP* CMB-free and NVSS catalogues. We find that in all cases the radio sources show wider profiles than the Jupiter beam with little indication of Eddington bias or dependence on the method of normalisation. Applying our cross-correlation to realistic simulations strongly supports the accuracy of our beam profile measure-

ments. However, it must be said that in the *WMAP*7 data the W radio source profiles are less wide than previously found by Sawangwit & Shanks (2010a) in the *WMAP*5 release. The rejection of the Jupiter beam is now only $\approx 3\sigma$ in the *Planck* radio source comparison. But the rejection of the Jupiter beam is reasonably consistent between the admittedly overlapping radio source samples from *Planck*, *WMAP* and NVSS. We have therefore considered explanations for the wide profiles assuming that they are not statistical fluctuations. Two such possibilities are a non-linearity in the *WMAP* temperature scale and a timing offset in the *WMAP* scan pattern as discussed by Liu & Li (2011). The narrower profiles measured here compared to the Sawangwit & Shanks (2010a) *WMAP*5 profiles increase the possibility of their being explained by a timing offset. However, we note that assuming a timing-offset derived beam results in a *WMAP* power-spectrum which is in strong disagreement with independent ground based observations from SPT and ACT.

We have also found discrepancies between *WMAP* fluxes compared to *Planck* and ground-based fluxes. For $S < 30$Jy the *WMAP* fluxes look to have a non-linear relation with *Planck* fluxes. However, when the further very bright sources discussed by Weiland et al. (2011) with ground-based and *Planck* measurements are included then this flux-flux discrepancy appears more like a linear than a non-linear offset.

We have shown that transforming the Jupiter beam using a model that fits the radio source profiles results in small but significant changes to the *WMAP* C_ℓ. At the least, a wider beam would imply a much larger uncertainty in the normalisation and hence the estimate of σ_8 from *WMAP*. Unfortunately, faint radio sources cannot check the *WMAP* beam at scales larger than $30'$ and a wider beam at these scales could, in principle, change the position, as well as the normalisation, of even the first acoustic peak. Clearly it is important to continue to test the calibration and beam profile of *WMAP*, particularly in the W band. It will also be important to apply similar radio source beam profile checks to the recently released *Planck* maps.

Chapter 3

Testing WMAP data via Planck SZ catalogues

3.1 Introduction

Although *WMAP* has played a vital role in establishing the ΛCDM model several anomalies between ΛCDM and the *WMAP* data have been discussed. Typically these have involved the large-scale temperature multipoles eg: (Bennett et al., 2011; Liu & Li, 2011). However, other anomalies in the CMB at smaller scales have also been detected, connected in particular with the SZ decrements from galaxy clusters (Myers et al., 2004; Bielby & Shanks, 2007). SZ decrements are created when CMB photons inverse Compton scatter off hot electrons in galaxy clusters. Myers et al. (2004) first stacked *WMAP* data at the positions of galaxy clusters and suggested that the profiles were more extended than expected. Lieu et al. (2006) and Bielby & Shanks (2007) then found that the SZ decrements from *WMAP* were reduced compared to X-ray predictions, possibly due to the *WMAP* beam being wider than expected. Bielby & Shanks (2007) also found that the *WMAP* decrements were significantly lower than the ground-based SZ measurements by Bonamente et al. (2006) in 38 X-ray luminous clusters.

In their ESZ sample, the *Planck* team find excellent agreement with the self-similar X-ray estimates of the SZ decrement (Planck Collaboration, 2011c,d). This is corroborated by the ground based South Pole Telescope Collaboration with their blind SZ selected cluster sample (Mroczkowski et al., 2009). This compounds the question of why *WMAP* SZ analyses from Lieu et al. (2006) and Bielby & Shanks (2007) failed to find such an agreement.

In this study we therefore revisit the question of the *WMAP* SZ deficit using the

recent *Planck* Early Data Release and X-ray data of Bonamente et al. (2006). The *Planck* Early Release Compact Source catalogue (ERCSC) and in particular the Early SZ (ESZ) catalogue only provide the basic parameters of the SZ clusters detected in the *Planck* CMB maps. We therefore use the SZ template and profile parameters which are the basis of the *Planck* SZ flux estimation to invert the total SZ flux into an expected *Planck* profile. We go onto compare this to *WMAP* SZ signal that we measure around the clusters to test whether the *WMAP* and *Planck* SZ signals are consistent.

3.2 Data

3.2.1 *Planck* Early Data Release

As noted in Section 2.2 the *Planck* Early Data Release consists of data on sources that provide foreground contamination to the CMB signal. Of particular interest for this study is the *Planck* SZ catalogue which consists of the SZ clusters detected in the *Planck* maps and their corresponding profile parameters.

Planck SZ Catalogue

The Early SZ (ESZ) catalogue lists all the robust and extensively verified SZ detections in the first data release. As described by Melin et al. (2006), the *Planck* team extract the integrated SZ signal, the *Y* parameter, using a Multifrequency Matched filter (MMF3) method (Planck Collaboration, 2011b). The algorithm is run blindly on all-sky maps, assuming the characteristic SZ spectral signature and self-similar cluster profile.

In the Early Release of the *Planck* SZ catalogue, only data from the 100GHz frequency channel or higher has been used to study the SZ effect. This is to avoid the detrimental effect on S/N from beam dilution caused by the larger beam sizes of the lower frequency channels. At the higher frequencies, the *Planck* beam FWHM is typically $\approx 4.'5$. The full details of the catalogue construction and composition are described by the Planck Collaboration (2011b).

The catalogue provides estimates of the SZ flux, extent, redshift and position. It consists of 189 clusters, all detected at high S/N (≥ 6) with 95% reliability. Whilst the sample is primarily composed of known clusters (169/189), it provides a wealth of new

information as it gives the first SZ measurements for $\approx 80\%$ of the clusters. In this study we only make use of clusters which have been pre-detected in the X-ray and have redshifts. We therefore, after masking, consider 151 clusters, including Coma. For this sample the redshift range spans $z \in [0.0126, 0.546]$ with a mean redshift of $\overline{z} = 0.18$.

3.2.2 *WMAP* Data

As in Chapter 2 we use the 7-year *WMAP* temperature maps obtained from the LAMBDA CMB resource. We again use foreground unsubtracted maps at $N_{side} = 512$. To maximise the S/N we use the co-added band maps and adopt the same method of estimating a corresponding co-added beam function as detailed in Section 2.2.2. To avoid Galactic contamination for the SZ analyses we have instead used the extended temperature mask (`wmap_ext_temperature_analysis_mask`) which admits 71% of the sky.

3.3 Cross-correlation methods

We again use the same stacking procedure and error estimation outlined in Section 2.3.3 to estimate the SZ profile around the *Planck* and Bonamente et al. (2006) clusters in the *WMAP* maps. We have adopted the `photometric' method of subtracting the background signal. We find this makes marginal difference to the stacked results but can be significant in the case of a single cluster - such as Coma.

For the *Planck* ESZ objects we have taken the *Planck* estimated positions rather than the X-ray derived positions as the cluster centres. We do this to avoid the complications associated with rare but potentially large offsets between the SZ and X-ray signals which are likely caused by merging events (Planck Collaboration, 2011b).

3.3.1 *Planck* SZ Decrements

Planck presents its observed decrements using an SZ model fit parameterised by the total SZ signal within the cluster extent. Here we briefly describe this model so that the *Planck* results can be compared to the stacked *WMAP* temperature decrements.

Clusters are significant reservoirs of gas which will result in a SZ distortion to the CMB described by the Compton *y* parameter,

$$\Delta T(\theta) = T_{cmb} j(x') y(\theta). \tag{3.1}$$

Here, $j(x')$ is the spectral function, where $x' = h\nu/k_b T_{cmb}$ (Sunyaev & Zeldovich 1980),

$$j(x') = \frac{x'(e^{x'}+1)}{e^{x'}-1} - 4. \tag{3.2}$$

The integrated *Y* parameter is the total SZ signal, which is simply the integration of the Compton y parameter on the sky,

$$Y = \int y d\Omega. \tag{3.3}$$

Alternatively, if we integrate over the cluster volume,

$$Y = \frac{\sigma_t}{m_e c^2} \int P dV. \tag{3.4}$$

However, we are observing a 2-D projection of the cluster[1] on the sky. The angle θ we observe on the sky, corresponds in 3-D to a cylindrical bore through the cluster of radius $R = \theta D_a(z)$, where D_a is the angular diameter distance. The observed integrated *Y* parameter therefore takes the form (Arnaud et al., 2010),

$$\begin{aligned} Y_{cyl}(R) &= \frac{\sigma_t}{m_e c^2} \int_0^R 2\pi r dr \int_r^{R_{tot}} \frac{2P(r')r'dr'}{(r'^2 - r^2)^{1/2}}, \\ &= Y_{sph}(R_{tot}) - \frac{\sigma_t}{m_e c^2} \int_R^{R_{tot}} 4\pi P(r)(r^2 - R^2)^{1/2} r dr. \end{aligned} \tag{3.5}$$

To predict the SZ effect implied by eq. 3.5 we have to make a choice of the pressure profile, $P(r)$. Historically it has been common to fit the SZ profile with an isothermal β model, (Cavaliere & Fusco-Femiano, 1976). However, X-ray observations have shown that the assumption of an isothermal gas breaks down at the cluster outskirts, (Pratt et al., 2007; Piffaretti et al., 2005). To account for this additional complexity Nagai et al. (2007) proposed using a Generalised Navarro-Frenk-White (GNFW) profile for the pressure instead. The profile is scale invariant in that it is independent of absolute

[1]The cluster is assumed to be spherical.

distances and is instead a function of the dimensionless scale $x = R/R_{500}$. The profile takes the form,

$$\mathcal{P}(x) = \frac{P_0}{(c_{500}x)^{\gamma}[1 + (c_{500}x)^{\alpha}]^{(\beta-\gamma)/\alpha}}, \tag{3.6}$$

where $\mathcal{P}(x) = P(r)/P_{500}$ and P_{500} is the characteristic pressure defined by Arnaud et al. (2010).

Here we have a five parameter fit to the pressure profile, $[P_0, c_{500}, \gamma, \alpha, \beta]$. This allows independent specification of the pressure in the cluster core (γ), main-body (α) and outskirts (β). In Table 3.1 we outline the parameters used by *Planck*, as taken from Arnaud et al. (2010). The characteristic parameters of the cluster are M_{500}, P_{500}, R_{500} (see Appendix A) where the 500 denotes the fact they are evaluated within the region where the mean mass density is 500 times greater that the critical density $\rho_{crit}(z)$. The *Planck* team extract the integrated *Y* parameter using the Multifrequency Matched Filter (MMF3) method (Planck Collaboration, 2011b) based on the above self-similar model. The integration is done to the angular cluster extent corresponding to $5R_{500}$, which *Planck* also report (θ_{5R500}). Their errors on the integrated SZ signal, *Y*, combine their estimated measurement error with Monte-Carlo estimates of the error due to uncertainities within the self-similar model (Melin et al., 2006).

3.3.2 SZ Temperature Profile Reconstruction

We now proceed to invert the *Planck* data to provide us with expected *WMAP* temperature profiles - see Appendix A for the details of this derivation. From the *Planck* values for $Y(5R_{500})$ and θ_{5R500}, and using $J(x)$ and $I(x)$, the cylindrical and spherical SZ templates (see eq. A.7) we first obtain $Y_{cyl}(R)$ via eq. A.9,

$$Y_{cyl}(R) = Y_{cyl}(5R_{500})\left(1 - \frac{J(x)}{I(5)}\right). \tag{3.7}$$

From this integrated $Y_{cyl}(R = \theta \cdot D_A(z))$, we want to derive the angular dependence of the Compton *y* parameter, where $y(\theta) = \frac{d}{d\Omega}Y_{cyl}(\theta)$, and so

$$y(\theta) = -\frac{Y_{cyl}(5R_{500})}{I(5)}\frac{d}{d\Omega}\big(J(x)\big). \tag{3.8}$$

The self-similar model therefore predicts an SZ temperature decrement,

Type	P_0	c_{500}	γ	α	β
All:Fitted	$8.403(\frac{h}{0.7})^{-\frac{3}{2}}$	1.177	0.3081	1.0510	5.4905

Table 3.1: Summary of the *Planck* NFW parameters as used in eq. 3.6 and described by Arnaud et al. (2010). These are the same parameters as used by the *Planck* team, the All:Fitted set.

$$\Delta T_{SZ}(\theta) = -T_{cmb} j(x') \frac{Y_{cyl}(5R_{500})}{I(5)} \frac{d}{d\Omega}\big(J(x)\big), \tag{3.9}$$

where $Y_{cyl}(5R_{500})$ is the integrated Y given in the ESZ.

3.3.3 Convolution with the *WMAP* beam profile

The cluster profile is not directly observed by *WMAP* and is instead smoothed by the instrument response. The predicted *WMAP* SZ profile therefore results from the 2-D convolution of eq. 3.9 with the *WMAP* beam profile. Myers et al. (2004) and Bielby & Shanks (2007) assumed that the source is well resolved with respect to the *WMAP* beam. Under this assumption the full form for a 2-D convolution can be approximated by a 1-D convolution[2]. However, the typical cluster sizes used in SZ studies are of the same order as the *WMAP* beams and so this approximation can start to fail. Furthermore, for profiles such as the self-similar model which are very centrally peaked this approximation becomes increasingly invalid. The implementation of the PSF convolution used in this study is fully 2-D and does not rely on such approximations. In Section 3.4.4 we explore the impact of this on the Bielby & Shanks (2007) results.

[2]Taking a Gaussian beam as an example, if σ_{beam} is much smaller than the typical scale of the cluster profile then the θ integral in Bailey & Sparks (1983)'s eq. 2 which describes the non-radial aspect (ie: the 2-D nature) of the convolution is approximately 2π. This effectively reduces the dimensionality of the convolution, which now takes a 1-D Gaussian form.

3.4 SZ Results

3.4.1 *Planck* Intermediate Results

Our final aim is to make a comparison between the *Planck* ESZ and *WMAP* SZ results as described in Section 3.3.1, 3.3.2 and 3.3.3. However this involves reverse engineering the *Planck* SZ $\Delta T(\theta)$ profiles. We therefore first use recently released *Planck* SZ data to check our reverse engineered *Planck* profiles. A series of papers have been released as a follow up to the *Planck* ESZ data. Two papers in particular are relevant to corroborating the *Planck* profiles presented in this study. In Planck Collaboration (2013f) the *Planck* Coma SZ profile has been published. Additionally, the `physical' *Planck* SZ temperature profiles for the 62 local clusters (LSZ) in the Planck Collaboration (2011d) analysis have been published in Planck Collaboration (2013e). Below, we compare our reverse engineered profiles to these *Planck* data.

Planck Collaboration (2013f)

In Fig. 3.1 we now compare our *Planck* Coma SZ profiles to Planck Collaboration (2013f). We have shown two alternative *Planck* models in order to display the sensitivity of our results to the cluster size estimates. This is motivated by the significant difference between the value of $R_{500} = 1.31Mpc$ used in Planck Collaboration (2013f) and the ESZ value, $R_{500} = 1.13Mpc$. Since the value for the integrated SZ signal, $Y(5R_{500})$, is degenerate with cluster size the ESZ value for $Y(5R_{500})$ cannot be assumed. Therefore, in the first instance we do show an expected *Planck* temperature decrement using the ESZ values and calculated using eq. 3.9. However, we also show a model which uses an alternative method for calculating the expected *Planck* profile. Here, the Planck Collaboration (2013f) value of R_{500} is used to calculate Y_{500} which can then be used to set the profile amplitude as shown in eq. A.8. This method is solely dependent on the cluster size estimate, and is further described in Appendix A.

We find agreement between the Coma self-similar SZ model and the observed *Planck* temperature profiles. Although the *Planck* data does seem to have both a lower central amplitude and a slightly wider profile at large angular scales than the self-similar expectation. We note that corresponding differences between the self-

similar model and the *Planck* data can be seen in the Planck Collaboration (2013f) analysis. A flatter inner profile may also be expected if any pixelisation effects cause any further smoothing beyond the stated resolution of $10'$. We also find reasonable agreement between our two estimates of the *Planck* profile that use different cluster size estimates. Although, as expected, the model using the Planck Collaboration (2013f) value of R_{500} does provide a better fit to the *Planck* data. We conclude that the agreement between our *Planck* expectation and the underlying *Planck* profile supports the validity of our inversion of the *Planck* ESZ data to obtain *Planck* temperature profiles.

Planck Collaboration (2013e)

In Fig. 3.2 we compare our *Planck* `physical' SZ profiles for the 62 Planck Collaboration (2011d) clusters to the `physical' *Planck* profiles presented in Planck Collaboration (2013e). As was previously shown in Planck Collaboration (2013e) the *Planck* [100,70,44] GHz profiles are in agreement with the self-similar expectation. We now expand on this by attempting to use these results to verify our method of inverting the *Planck* ERCSC data to obtain *Planck* temperature profiles.

Since we again find that the Planck Collaboration (2011d) estimates of cluster size can be significantly different from the ESZ estimates we have used an alternative method of obtaining expected *Planck* temperature profiles. This method replicates Planck Collaboration (2013e)'s approach in assuming the Arnaud et al. (2010) self-similar model for the cluster and directly evaluating the Compton-y parameter, as outlined in Appendix A. We have further followed Planck Collaboration (2013e)'s Section 4.3 in using the Planck Collaboration (2011d) estimates of θ_{500} and calibrate the central GNFW pressure, P_0, using the X-ray equivalent of the integrated SZ signal, Y_X.

As shown in Fig. 3.2 the two self-similar models convolved with $10'$ FWHM Gaussian beam profiles are in agreement beyond R_{500}. However the inner profile of Planck Collaboration (2013e)'s model (black, solid $\pm$ dotted) is substantially sharper than our model (green, solid). Although our model lies within the Planck Collaboration (2013e)'s $\approx 1\sigma$ dispersion, we are comparing the stacked models (ie: the statistical average) so the error range is a $\sqrt{N} \approx 8$ smaller. We believe this difference is caused by the

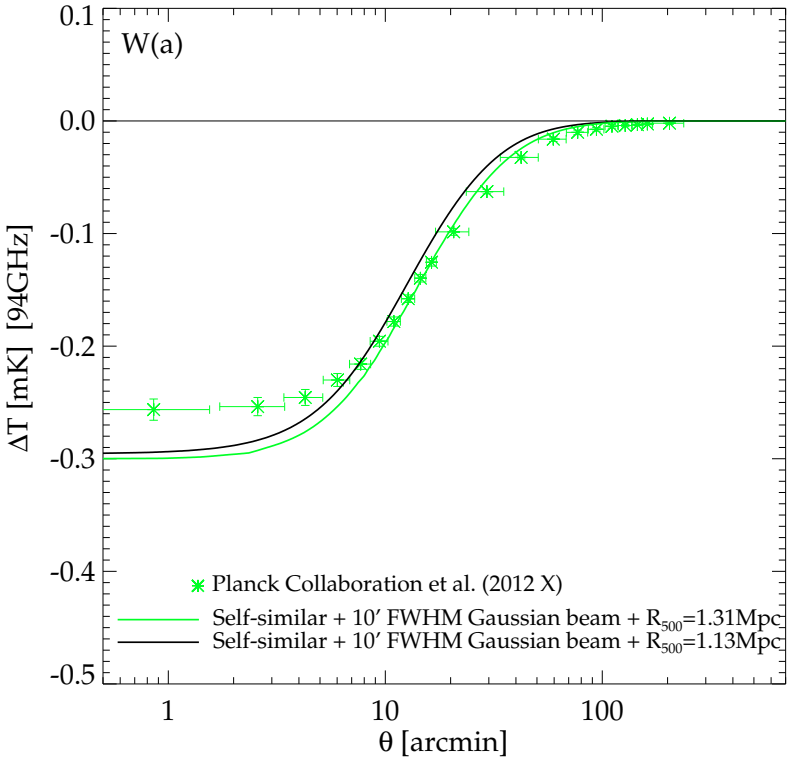

Figure 3.1: (a): The Planck Collaboration (2013f) *Planck* SZ decrement for the Coma cluster converted from RJ temperatures to a thermodynamic temperature at 94GHz. Also shown are the *Planck* temperature decrements from eq. 3.9 using the ESZ value of R_{500} (black, solid) and eq. A.8 using the Planck Collaboration (2013f) value of R_{500} (green, solid). Both models are convolved with a $10'$ FWHM Gaussian beam appropriate to the Planck Collaboration (2013f) data.

different stacking procedure used in Planck Collaboration (2013e) where depending on the noise properties within the bin either logarithmic or linear weightings were used. We have found that using these alternative weightings can accentuate the central peak of the profile, although not to the extent necessary for full agreement with Planck Collaboration (2013e). We currently do not have a full explanation for the difference in central amplitude.

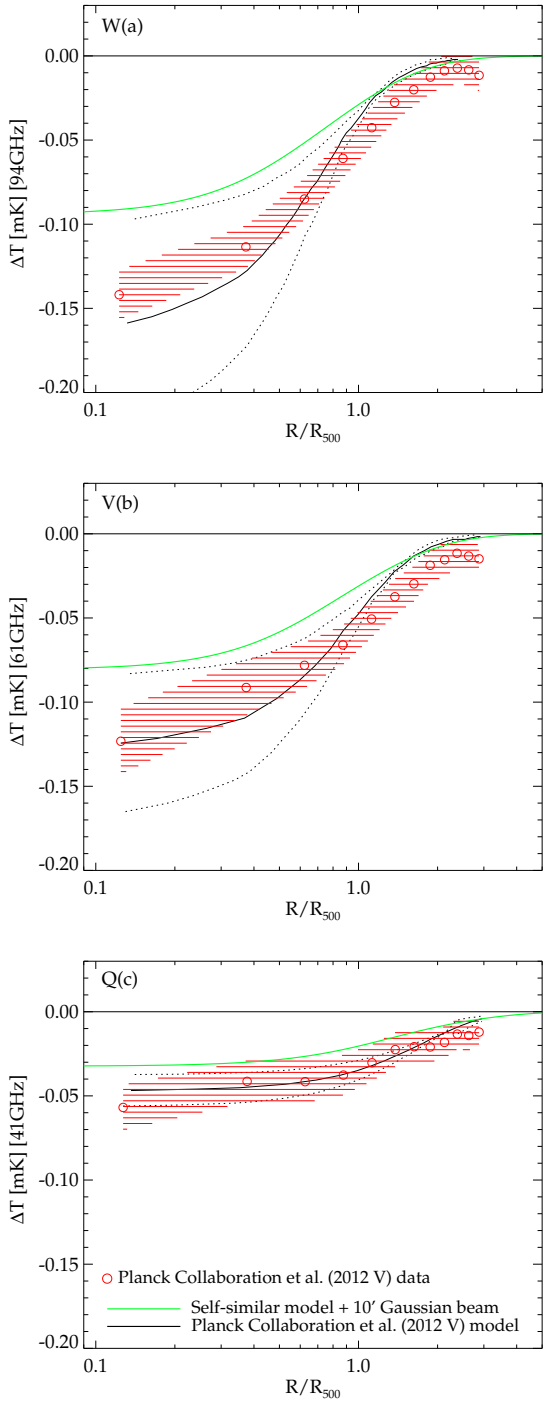

Figure 3.2: (a),(b),(c): The *WMAP*7 [W,V,Q] `physical' SZ decrements for the 62 Planck Collaboration (2011d) clusters compared to the *Planck* temperature decrement from eq. 3.9. The *Planck* profile is shown convolved with a $10'$ FWHM Gaussian (green, solid). We also show the 100GHz *Planck* profiles presented in Planck Collaboration (2013e) converted into thermodynamic temperature at the *WMAP* band centre (red, stripes). The Planck Collaboration (2013e) models (black, solid) are plotted with their associated dispersions (black, dotted).

3.4.2 *WMAP-Planck* ESZ comparison

We next show the stacked *WMAP*7 temperature profiles for 151 clusters listed in the *Planck* ESZ catalogue. We are using the `photometric' approach to background subtraction, with an annulus from $60' - 120'$ being used in W (and scaled according to beamwidth in Q and V). The final models are based on the statistical average of the clusters.

We see in Fig. 3.3 that the *WMAP* data is an excellent fit to the *Planck* expectation. The fit between the *Planck* data and the *WMAP* data is not only good in all three [W,V,Q] bands but at all angular scales. We have further quantified the SZ measurements using jack-knife and bootstrap techniques all of which support *WMAP-Planck* agreement, however we acknowledge these techniques don't include covariance.

In Fig. 3.3 we have shown the *Planck* self-similar models convolved with the power-law beams from Sawangwit & Shanks (2010a). We find that in the case of the W band where the radio source profiles are most different from the Jupiter beam, there is now disagreement with the *WMAP* data with a deficit of $\approx$ 20% in the centre. In the Q and V bands where the radio source profiles are closer to the Jupiter beam, the wider beams give virtually no change in the agreement with the *WMAP* data. We conclude that the *Planck* SZ profiles disagree with the Sawangwit & Shanks (2010a) *WMAP*5 radio source profile fits.

However, the Sawangwit (2011) timing offset derived beam, which provides an excellent fit to the radio source profiles as shown in Fig. 2.8, is significantly less wide than the Sawangwit & Shanks (2010a) beam. As shown in Fig. 3.3 we find that the timing offset beam only marginally reduces the central SZ temperature. We therefore conclude that the *WMAP* SZ results are not at sufficient S/N to differentiate between the timing offset derived and the Jupiter beams.

Finally, we note the Integrated Sachs-Wolfe (ISW) effect is at most a $10\mu K$ effect for clusters/superclusters, (Granett et al., 2008). It is therefore highly unlikely to cause any bias to our SZ cluster analyses. This is too marginal to affect the profiles we recover.

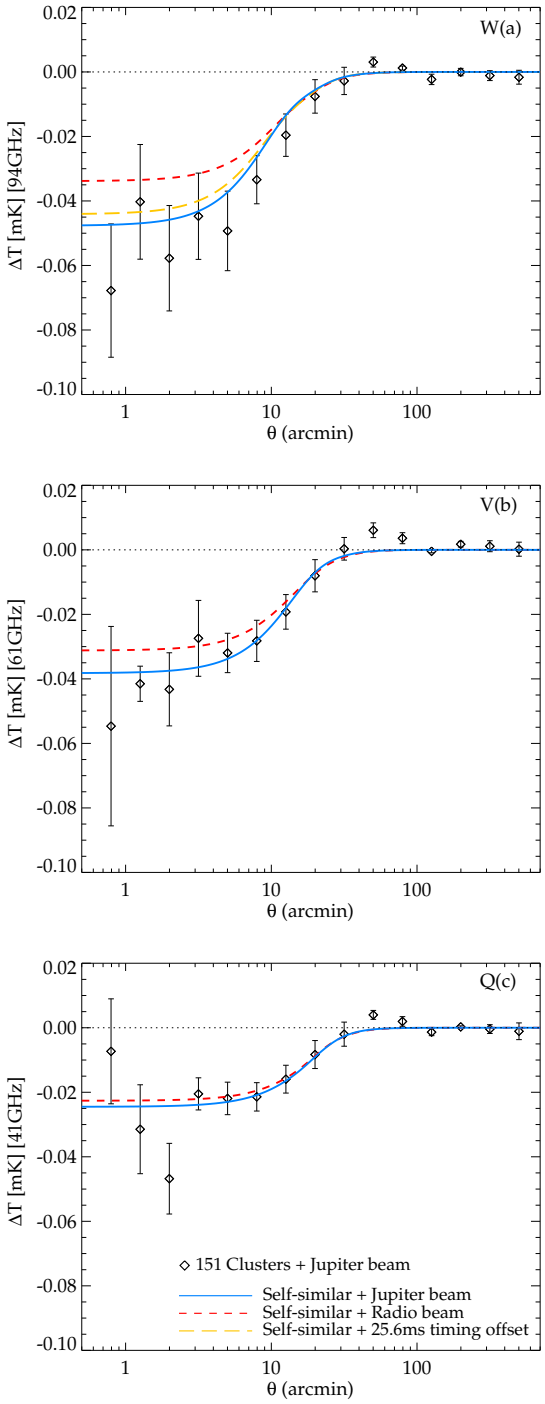

Figure 3.3: (a),(b),(c): The stacked *WMAP*7 [W,V,Q] SZ decrements for 151 *Planck* SZ clusters compared to the stacked *Planck* temperature decrement from eq. 3.9. The *Planck* profile is shown convolved with a *WMAP* Jupiter beam, a beam fitted to the radio source profiles by Sawangwit & Shanks (2010a) and the Sawangwit (2011) timing offset derived beam.

3.4.3 Coma

We have also looked at the *Planck* model fits for the Coma cluster and compared them to *WMAP*. Part of the motivation here is that previous authors, Lieu et al. (2006) and Bielby & Shanks (2007), have used Coma in investigating the consistency of the *WMAP* SZ signal with X-ray predictions.

In Fig. 3.4 we now show the *Planck* self-similar model for Coma (solid blue line) and see that it is substantially overestimated by the *WMAP* data. An analogous situation was found by Komatsu et al. (2011) in that the *WMAP* Coma V and W band profiles (potentially affected by CMB contamination) showed $\mathcal{O}(100\mu K)$ more SZ signal than the optimal combined V and W profiles (free of CMB contamination).

Komatsu et al. (2011) proposed that Coma may sit on $\mathcal{O}(100\mu K)$ downwards CMB fluctuation. Our results are entirely consistent with this interpretation because the *Planck* MMF method is essentially `CMB-free' whereas our *WMAP* Coma data may still be contaminated by CMB fluctuations. On this basis we also show in Fig. (3.4) a simple alteration to the *Planck* Coma SZ self-similar model by including a Gaussian with amplitude $-100\mu K$ and $(\mu, \sigma) = (0', 60')$ to mimic the effect of a downwards CMB contribution centred on Coma (blue, dashed). Agreement with the *WMAP* data is improved when a CMB contamination term is included. We therefore conclude that the difference between the *Planck* and *WMAP* Coma SZ profiles is the result of CMB contamination.

3.4.4 Bonamente et al. (2006) Results

In Bielby & Shanks (2007) a *WMAP* discrepancy with the SZ/X-ray results of Bonamente et al. (2006) was presented. This is of particular interest as the Komatsu et al. (2011) *WMAP* SZ discrepancy was largely associated with the inner profile. The Bonamente et al. (2006) results complement this because they are weighted heavily to small scales because of the high resolution of their interferometric observations. In Fig. 3.5 we have therefore presented a stack of the 36 Bonamente et al. (2006) clusters that are unmasked in the *WMAP* temperature maps. We now find good agreement between the *WMAP* SZ decrements and the Bonamente et al. (2006) SZ/X-ray expectation. This is in contradiction to the results of Bielby & Shanks (2007). We have found this

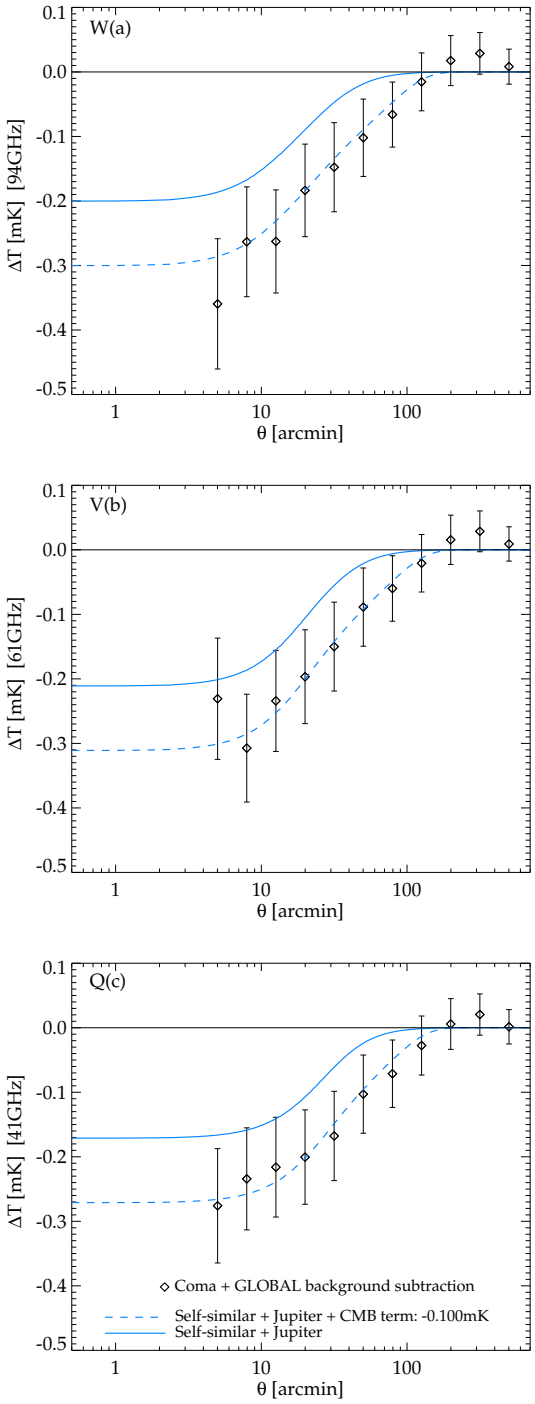

Figure 3.4: (a),(b),(c): The *WMAP*7 [W,V,Q] SZ decrements for the Coma cluster compared to the *Planck* temperature decrement from eq. 3.9. The error within each annulus for this individual cluster is simply the standard deviation of the ESZ clusters and is therefore only indicative. The *Planck* profile is shown convolved with a *WMAP* Jupiter beam (blue, solid). We also show a model incorporating a $100\mu K$ downwards CMB fluctuation (blue, dashed).

is attributable to Bielby & Shanks (2007)'s assumption that the cluster is well resolved with respect to the *WMAP* beam. As discussed in Section 3.3.3 this assumption introduces a systematic error into their 1-D convolution with the *WMAP* beam profiles. We therefore now report no evidence for a *WMAP* SZ discrepancy with respect to the Bonamente et al. (2006) X-ray models.

3.5 Conclusions

We began by showing that our *Planck* profiles are consistent with the *Planck* results of Planck Collaboration (2013e) and Planck Collaboration (2013f). We interpret this as validating our method of inverting the *Planck* ERCSC data to obtain *Planck* SZ temperature profiles.

We therefore proceeded to compare the *Planck*-*WMAP* SZ decrements and found good agreement. Similarly, our *WMAP* SZ profile results are now in agreement with the X-ray data for the Bonamente et al. (2006) sample. This work is now in line with previous authors who when studying the integrated *WMAP* SZ signal Y_{tot} (as opposed to the Compton y-parameter) have found no evidence for a *WMAP* SZ deficit (Melin et al., 2011). We have no explanation for the Komatsu et al. (2011) *WMAP* SZ profile discrepancies at this point.

We note although the *Planck* Early data radio sources provide evidence for a wider *WMAP* beam the *WMAP* SZ profiles are at insufficent S/N to distinquish between the Jupiter beam and the timing-offset derived beam which well described the *WMAP* radio source profiles.

Finally, we note that the recent release of the *Planck* temperature maps enables further research into this topic. The study of the *Planck* SZ profiles will provide richer understanding of cluster physics and possibly illuminate any of the *WMAP* discrepancies found with the *Planck* radio sources.

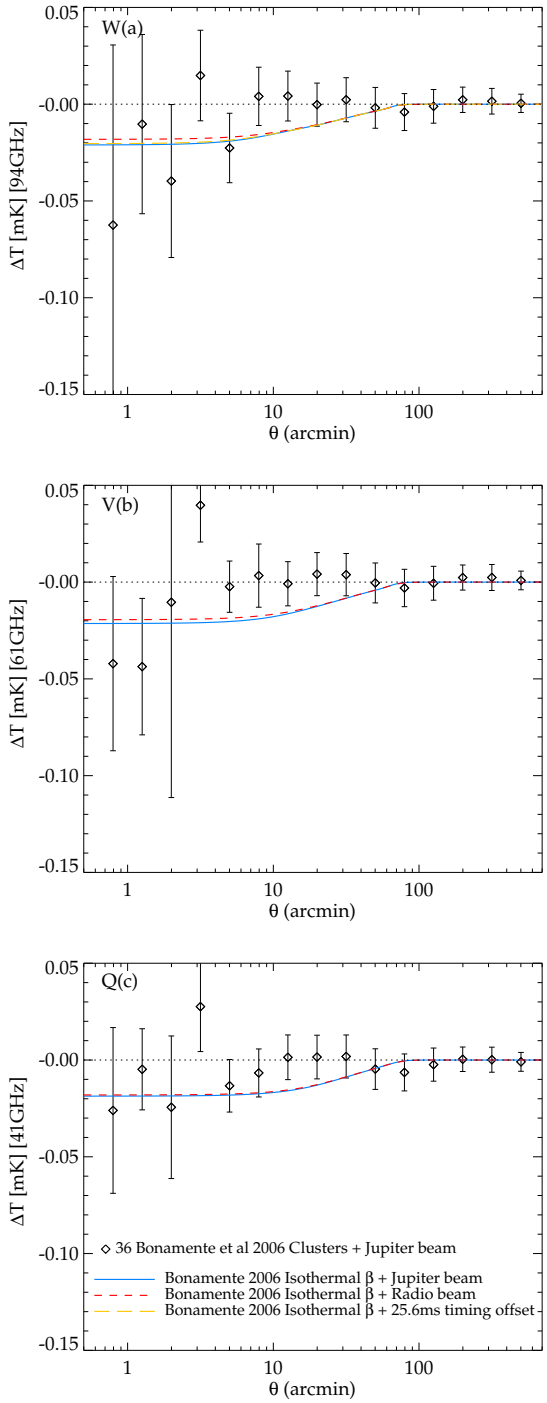

Figure 3.5: (a),(b),(c): The stacked *WMAP*7 [W,V,Q] SZ decrements for the 36 Bonamente et al. (2006) clusters that are unmasked in the *WMAP* temperature maps. This is compared to a stacked isothermal model based on the SZ/X-ray parameters fitted by Bonamente et al. (2006), convolved with the Jupiter beam, a beam fitted to the radio source profiles by Sawangwit & Shanks (2010a) and the Sawangwit (2011) timing offset derived beam.

Chapter 4

The Local Hole revealed by galaxy counts and redshifts

4.1 Introduction

The Cosmological Principle is a fundamental assumption of Cosmology that leads us to describe our universe as statistically homogeneous and isotropic, which uniquely gives the Friedmann-Lemaitre-Robertson-Walker (FLRW) solutions to Einstein's field equations. These metrics are apparently successful, encompassing many current observations of the Universe over huge scales in space, time and energy.

However, at least locally, the validity of the Cosmological Principle is less obvious. Deep redshift surveys such as SDSS (York et al., 2000) and Two-degree Field Galaxy Redshift Survey (2dFGRS, (Colless, 2001)) have revealed a web-like structure to the galaxy distribution with extensive and ongoing clustering at knots and junctions. Indeed, recent redshift surveys have found this LSS persisting up to at least scales of $300h^{-1}Mpc$ (Gott et al., 2005; Murphy et al., 2011). The results are in concordance with ΛCDM N-body simulations with the galaxies displaying the expected hierarchical structure from individual galaxies to galaxy clusters to superclusters (Park et al., 2012; Watson et al., 2013). The visible structures are parsed by large coherent regions of under-density known as voids, which can be of $\mathcal{O}(50Mpc)$. Compared to galaxy clusters, voids were a relatively recent discovery in cosmography as they required large redshift surveys to easily separate galaxies in the same line of sight by redshift. These regions seem to be approximately spherical and underdense in all types of matter (Peebles & Nusser, 2010; Rood, 1988).

The question of the local galaxy density has received renewed attention due to the challenges represented by the recent measurements of a Λ-like accelerated expansion of the universe (Schmidt et al., 1998; Perlmutter et al., 1999). There is the possibility that the role of Λ in producing the dimming of the $m-z$ relationship for SNIa could instead be due to the acceleration induced by a large local under-density. Recently it has been shown that $\mathcal{O}(Gpc)$ local hole models can accurately mimic Λ whilst accounting for independent scale factor measurements (February et al., 2010). However, it remains unclear as to whether these models can equally well simultaneously account for other cosmological datasets[1] - see Biswas et al. (2010); Moss et al. (2011b) and also Regis & Clarkson (2012); Nadathur & Sarkar (2011).

4.1.1 Scale of Homogeneity

The observation of isotropy to $\mathcal{O}(10^{-5})$ in the temperature of the CMB (Wright et al., 1992) is extremely strong evidence for the fundamental isotropy of the universe. An observation of homogeneity for the whole universe is technically impossible for terrestrial cosmologists as we are limited to one lightcone at our location, (Clarkson & Maartens, 2010). However assuming the Copernican principle[2] that our observations are typical, then the isotropy of the CMB is equivalent to homogeneity. So studies of how homogeneous our observations of the universe are is closely related to understanding how typical and representative they are - see Section 1.5 for further discussion of homogeneity.

Results disagree as to whether recent redshift surveys have approached the depths required to describe the universe as statistically homogeneous. Studies of the fractal dimension of the galaxy distribution typically report a homogeneity scale of $\approx 70\mathrm{h}^{-1}$Mpc (Sarkar et al., 2009; Scrimgeour et al., 2012; Hogg et al., 2005). However, other studies instead find the presence of LSS beyond these scales and indeed persisting to the relevant survey depths (Labini, 2010; Célérier & Thieberger, 2005).

Efforts to use the number or flux dipole in a similar manner to the peculiar velocity

[1] Baryon acoustic oscillations (BAO), $H(z)$, Kinetic Sunyaev-Zel'dovich (kSZ), Lithium abundance, CMB fluctuations and Cosmic shear

[2] It might in principle be able to observe the Copernican principle (Goodman, 1995; Maartens, 2011; Caldwell & Stebbins, 2008)

dipole have been in concordance with the ΛCDM Standard Model (Bilicki et al., 2011; Blake & Wall, 2002a). Gibelyou & Huterer (2012) report that the NVSS number dipole is unexpectedly large, however they attribute this to potential systematic errors.

Studies of the structure of our local peculiar velocity field have used the scale at which the bulk peculiar velocity is that of the CMB dipole as a proxy for the scale of homogeneity. Some authors have reported a relatively local origin within $\approx 60\mathrm{h}^{-1}$Mpc for the dipole (Erdoğdu et al., 2006). However,

However, there have been claims of a local underdensity manifesting as a local rise in SNIa based measurements of H_0 (Zehavi et al., 1998; Jha et al., 2007). Although some authors attribute these results to systematics associated with dust these results are consistent with other work where bulk flows out to $z < 0.06$ are found using SNIa (Feindt et al., 2013; Colin et al., 2011; Wojtak et al., 2013) and the tension between local and CMB determinations of H_0 (Planck Collaboration, 2013c). Indeed, other recent studies have suggested that there are bulk flows at much larger scales (Abate & Feldman, 2012; Watkins et al., 2009; Feldman et al., 2010). These results though are in contrast with a series of papers, (Nusser et al., 2011; Branchini et al., 2012), where a method similar to one used here is pioneered and bulk flows consistent with ΛCDM were found.

Furthermore, attempts to infer the bulk velocity field with respect to the CMB have typically returned values incompatible with homogeneity (Kashlinsky et al., 2008; Lavaux et al., 2013). These results are however disputed by some authors (Keisler, 2009; Osborne et al., 2011).

Finally, reconstructions of Star Formation histories (SFH) have been proposed as a method for testing for departures from homogeneity (Heavens et al., 2011). Indeed, Hoyle et al. (2013) used a sample of high redshift ($0.2 < z < 0.5$) luminous red galaxies in this manner and found no evidence for inhomogeneity over this redshift range.

4.1.2 Number Counts

By counting the number of galaxies as a function of magnitude and redshift, strong constraints can be imposed on galaxy evolution, galaxy distribution and Cosmology. The existence of LSS in the form of superstructures such as filaments can be readily

detected in these counts (Frith et al., 2003).

In the Standard Model with Λ, number counts for $z < 1$ are well described by simple Pure Luminosity Evolution (PLE) models where galaxies form at high redshift and evolve according to their galaxy star-formation rate, with e-folding times assumed to be $\tau = 1-2.5$Gyr for redder types and $\tau = 9$Gyr for bluer types. These PLE models are successful across a wide range of passbands and to considerable redshift depth (Shanks et al., 1984; Metcalfe et al., 2001, 2006; Hill & Shanks, 2010)

However, the above PLE models cannot simultaneously account for bright and faint magnitude counts (Liske et al., 2003; Metcalfe et al., 2001). Specifically, the counts in the range $10 < B < 17$mag are significantly steeper than expected from a non-evolving model. Indeed the counts at fainter magnitudes are less steep relative to such a model. As long as the PLE model counts were normalised at $B \approx 18$mag the PLE models then fit in the range $18 < B < 28.5$ (Metcalfe et al., 2001) but attempts to fit at $B < 17$ inevitably overshoot beyond $B > 17$ and it seemed puzzling that the evolution rate should increase at lower redshift. It was therefore suggested that the steepness of the bright counts may be caused by a local under-density (Shanks et al., 1984). Luminosity functions (LF) measured in redshift surveys are reasonably consistent in form but there exists considerable variation in ϕ^* (Liske et al., 2003; Cross et al., 2001). This uncertainty is in part due to the failure of non-evolving (or simple PLE) models to fit bright and faint counts simultaneously and is known as the normalisation problem. There is supporting evidence for a faint count normalisation from several previous studies (Driver et al., 1995; Glazebrook et al., 1995), complemented by results from the latest and deepest number counts (Keenan et al., 2010; Barro et al., 2009) and luminosity functions (Keenan et al., 2012, 2013).

A further argument against the steep bright counts being caused by $z < 0.1$ galaxy evolution is that the steepness is observed across the NIR and optical bands (B,R,I,H,K) (Metcalfe et al., 2001, 2006). In models where SFR dominates the evolution, we should expect the bluer bands to be more affected than the redder bands and this effect is seen at fainter magnitudes but not at brighter magnitudes.

Using early (partial) Two Micron All-Sky Survey (2MASS) data releases, Frith embarked on a series of analyses at bright NIR magnitudes to investigate the strong local LSS hypothesis. Frith et al. (2003) observed evidence for the reality of the pro-

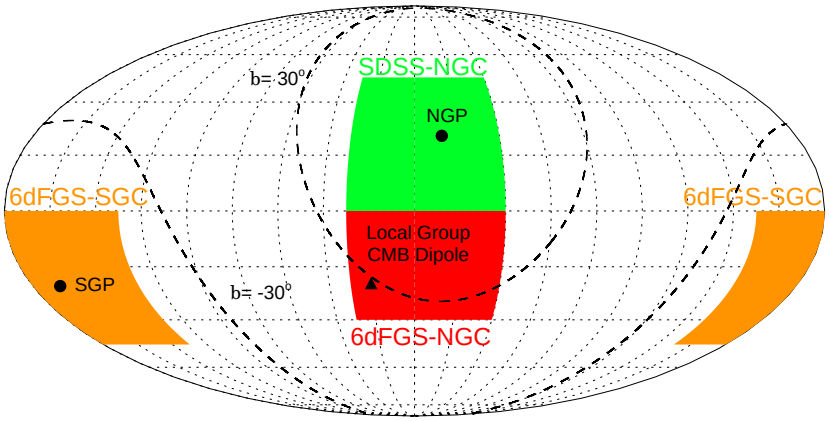

Figure 4.1: A Mollweide projection of the fields used in this study using the celestial coordinate system. The 6dFGS-NGC field is the filled area in red, the 6dFGS-SGC field is the filled area in orange and the SDSS-NGC is the filled area in green. Also shown are the Northern and Southern Galactic poles, the Local Group CMB dipole pointing and lines of $b = 30°$ and $b = -30°$ galactic latitude.

posed local under-density with the underdensities in the 2dFGRS redshift distribution accounting well for the underdense 2MASS number counts - see also Busswell et al. 2004. The galaxy distribution was found to be patchy with large regions of under- and over-density. Across the whole sky a coherent $\approx 15 - 20\%$ under-density, a local hole, on the scale of $\mathcal{O}(300Mpc)$ was consistent with these data.

Frith et al. (2006) also found further evidence that the faint normalisation is correct in the H band. Using a set of 2MASS mocks, the full sky under-density was found to represent a 2.5σ fluctuation for a ΛCDM model.

In this study we attempt to extend the Frith et al. (2005b) analysis of the local hole hypothesis. We first check out the connection between $n(z)$ and $n(m)$ in substantially bigger areas than available to Frith et al. We also test whether there is an under-density in the mass as well as the galaxy counts by estimating a velocity field using the Metcalfe et al. (2001) luminosity function and the $\overline{z}(m)$ Hubble diagram technique of Soneira (1979) which we outline below.

4.2 Techniques

4.2.1 Number-magnitude and number-redshift distributions

We will first compare the number-redshift and number-magnitude distributions with those that assume homogeneous models. We assume simple LFs as described by Metcalfe et al. (2001) and so predict the differential number redshift relation $n(z)$ using

$$n(z)dz = 4\pi r(z)^2 \frac{dr}{dz} dz \int_{M(m_b,z)}^{M(m_f,z)} \Phi(M) dM, \tag{4.1}$$

where m_b and m_f are the bright and faint survey magnitude limits respectively, $r(z)$ is the comoving radial coordinate, $\Phi(M)$ is the differential Schechter (1976) luminosity function in comoving units with characteristic absolute magnitude and density, $M^*(z)$ and $\phi^*(z)$ and slope α. Our models for the redshift dependence of $M^*(z)$ include K plus E corrections from Bruzual & Charlot (2003) models with ϕ^* and α held constant for individual galaxy types for the homogeneous models. We shall generally normalise the homogeneous $n(z)$ model to exceed the observed $n(z)$ by the ratio of homogeneous model counts to the observed $n(m)$. We shall then simply divide the observed $n(z)$ by the homogeneous model $n(z)$ to determine how the galaxy density $\phi^*(z)$ varies with redshift.

The homogeneous number-magnitude relation is then similarly calculated as,

$$n(m)\Delta m = \int_0^\infty 4\pi r(z)^2 \frac{dr}{dz} dz \int_{M(m_b,z)}^{M(m_f,z)} \Phi(M) dM, \tag{4.2}$$

where $m = (\frac{m_b+m_f}{2})$, $\Delta m = m_f - m_b$. We can then also input $\phi^*(z)$ from $n(z)$ into the $n(m)$ model to check for consistency between any under- or over-densities found in $n(z)$ and $n(m)$.

4.2.2 Hubble Diagrams from galaxy redshift surveys

Hubble's law relates cosmological redshifts to distance. Usually the distances come from standard candles or rods for individual galaxies. But here we aim to use the galaxy luminosity function as the standard candle for magnitude limited samples of

galaxies using the average redshift as a function of magnitude, $\overline{z}(m)$, following Soneira (1979). In essence the method assumes a universal LF which is an approximation, ignoring environmental effects etc. But the bigger the volumes averaged the more this assumption will apply and the LF can then be used as a statistical standard candle.

Soneira (1979) working at small redshifts, assumed a Euclidean Cosmology and the redshift-distance relation, $z = br^p + y$, where the peculiar velocity y distribution is described by $Q(y)$, and derived

$$\overline{z}(m) \propto 10^{0.2pm}. \tag{4.3}$$

Clearly for a linear Hubble law, $p = 1$ and the aim of Soneira's analysis was to determine p. Here we use the same technique out to higher redshift where the potential effects of Cosmology, K correction and evolution cannot be ignored. We can describe $\overline{z}(m)$ in complete generality using the volume element dV/dr, the differential LF $\Phi(M)$, the peculiar velocity distribution $Q(y)$ and K plus E corrections,

$$\overline{z}(m) = \frac{\int_{-\infty}^{\infty} dy \int_{0}^{\infty} z(r,y)Q(y)\Phi(m - 5logd_L - 25 - KE(z))\frac{dV}{dr}dr}{\int_{-\infty}^{\infty} dy \int_{0}^{\infty} Q(y)\Phi(m - 5logd_L - 25 - KE(z))\frac{dV}{dr}dr}.$$

We initially only make the simplest set of assumptions about $Q(y)$, that it is normalised to one and with a mean of zero, i.e. non-streaming,

$$\int_{-\infty}^{\infty} Q(y)dy = 1, \quad \int_{-\infty}^{\infty} yQ(y)dy = 0. \tag{4.4}$$

In the case of velocity flows we have more complicated forms of $Q(y)$. The simplest such case is a bulk flow where all galaxies are moving coherently,

$$\int_{-\infty}^{\infty} yQ(y)dy = \frac{v_{\text{flow}}}{c}. \tag{4.5}$$

The implication for $\overline{z}(m)$ is that,

$$\overline{z}(m) = \overline{z}_{hubble}(m) + \frac{v_{\text{flow}}}{c}. \tag{4.6}$$

Therefore $\overline{z}(m)$ is dependent on galaxy streaming velocity.

$\overline{z}(m)$ is calculated in magnitude bins. We have chosen to use both $\delta m = 0.5$ and $\delta m = 0.1$. The larger $\delta m = 0.5$ binning is preferred because these have slightly smaller errors and reduced covariance between bins. However, we have also presented results for $\overline{z}(m)$ with the smaller magnitude binning size of $\delta m = 0.1$ to investigate the sensitivity of $\overline{z}(m)$ to individual elements of LSS, which the larger binning suppresses.

4.3 Modelling

We now need to model $n(z)$, $n(m)$ and $\overline{z}(m)$ first in the homogeneous case so below we present details of the galaxy evolution models and the luminosity function parameters.

4.3.1 Galaxy Evolution Models

A galaxy's apparent magnitude is dependent on both evolution and SED, hence modelling $\overline{z}(m)$ requires us to account for the $k(z)$ and $e(z)$ effects. The K plus E corrections used in this study are calculated using the stellar synthesis models set out in Bruzual & Charlot (2003). We have used an $x = 3$ IMF for early types to mimic the PLE galaxy models set out by Metcalfe et al. (2001, 2006).

In this study we will usually present results in the NIR and at low redshift, where the $e(z)$ and $k(z)$ corrections are relatively small and can be reasonably well determined. This is because the NIR is dominated by old stars and hence is insensitive to different star formation histories. (Bruzual & Charlot, 2003; Cole et al., 2001). We have verified this by experimenting with alternative forms for the $k(z)$ and $e(z)$ correction and found that the results are not sensitive to the exact form used.

4.3.2 Luminosity Functions

Our basic LF will be taken from Metcalfe et al. (2001). This is a type dependent LF that is inferred from the optical and translated into the NIR using the mean colours (see Table 4.1). Modelling of the number counts, redshift distributions and $\overline{z}(m)$ using this LF has been done using the full number count program described by Metcalfe et al. (1996).

Type	$\phi\ (h^3 Mpc^{-3})$	α	$M^*_{\mathsf{R}} - 5\log(h)$	R-K
E/S0	$7.416 \cdot 10^{-3}$	-0.7	-20.93	2.48
Sab	$3.704 \cdot 10^{-3}$	-0.7	-20.75	2.52
Sbc	$4.960 \cdot 10^{-3}$	-1.1	-20.87	2.45
Scd	$2.184 \cdot 10^{-3}$	-1.5	-20.70	2.13
Sdm	$1.088 \cdot 10^{-3}$	-1.5	-20.62	1.58

Table 4.1: Parameters for the zero redshift luminosity function as assumed here (Metcalfe et al., 2001, 2006). We will use a ΛCDM Cosmology with Ω_Λ=0.7, Ω_m=0.3 and $h = 0.7$.

4.3.3 Radial Inhomogeneity - LSS Correction

The derivation of $\overline{z}(m)$ shown earlier assumes radial homogeneity, $\overline{z}(\overline{r}) = \overline{z}(r)$ which leads to a sensitivity to over/under-densities, as was indeed originally noted by Soneira (1979). For example, the presence of a local hole would be expected to cause a boost to $\overline{z}(m)$ at bright magnitudes (small distances), even with no induced peculiar motion. This is because at a bright apparent magnitude, m, the ratio of galaxies outside the hole (with high z) and galaxies inside the hole (at low z) would be expected to increase with hole density contrast and scale. The inverse would be expected in the presence of a local over-density.

We can model this effect by varying the normalisation, ϕ^* of the LF we use. To do this we will include radial density profiles derived from our $n(z)$ distributions. Rather than allowing this measure to extend to the survey limits where the effect of redshift incompleteness and survey systematics become more prominent, we set a scale, z_{global} where we transition to the expected homogeneous value. We use values of z_{global}=0.15 and z_{global}=0.25 for the K and r bands respectively.

$$\phi^*(z) = \begin{cases} \frac{n(z)_{\mathsf{obs}}}{n(z)_{\mathsf{model}}} \phi^*_{\mathsf{global}} & \text{if } z \leq z_{\mathsf{global}} \\ \phi^*_{\mathsf{global}} & \text{if } z > z_{\mathsf{global}} \end{cases} \tag{4.7}$$

We are assuming the density variations in the $n(z)$ are real and using this to correct the $\overline{z}(m)$ model prediction for the effect of large-scale structure before looking for

residuals that can be interpreted as peculiar velocities, v_{pec}. We shall also use the same technique to correct our homogeneous model $n(m)$ prediction for the effect of large-scale structure to make consistency checks between $n(m)$ and $n(z)$.

In a future work to be published as Whitbourn (2013) we use simple maximum likelihood estimates of the luminosity function also to estimate $\phi^*(z)$ simultaneously. We find that the Metcalfe et al. (2001) LF used here is in good agreement with these ML estimates. The $\phi^*(z)$ density runs with redshift also agree with those reported below.

4.3.4 Error calculation and scaling

As a first approximation it is possible to assume Poisson errors for the number counts and standard errors for $\overline{z}(m)$. This though is unrealistic for real galaxy distributions since galaxies cluster. To account for this we have therefore calculated jack-knife errors. These were calculated using $10^\circ \times 10^\circ$ sub-fields. For N fields denoted *k*, the errors on a statistic f as a function of the variable x are,

$$\sigma_f^2(x) = \frac{N-1}{N} \sum_k^N \Big(f_k(x) - \overline{f}(x) \Big)^2, \tag{4.8}$$

where $f_k(x)$ is the average of the fields excluding field k. We have experimented with both more survey specific sub-fields and alternative methods such as field-to-field resampling and find approximately equivalent results in these cases.

4.4 Data - Surveys

In this section a compilation is given of the key characteristics of the imaging and redshift surveys used throughout this work. We shall generally use pseudo-total magnitudes, usually estimated by integrating a fitted analytic surface brightness profile to large radii - for details see individual surveys below. We shall use magnitudes zero-pointed in the $Vega$ system throughout. This is primarily for ease since the $2MASS$ photometry is quoted in this system. Where necessary we have converted from AB to Vega using the following offsets from Hill et al. (2011) and Blanton & Roweis (2007),

$$K_{vega} = K_{AB} - 1.90, \tag{4.9}$$
$$r_{vega} = r_{AB} - 0.16.$$

The NIR is minimally affected by dust extinction but we have applied extinction corrections using the extinction maps of Schlegel et al. (1998). We note that our results are insensitive to whether we apply the correction at all. This applies in r as well as K since the r band data used below are restricted to higher galactic latitudes

In terms of the redshift surveys, we choose to work in the Local group rest-frame. All redshifts have therefore been corrected to the Local group barycenter using $(l_{LG}, b_{LG}) = (93^{\circ}, -4^{\circ})$ and $v_{LG} = 316 kms^{-1}$ (Karachentsev & Makarov, 1996),

$$cz_{LG} = cz_{\odot} + v_{LG}\big[\sin(b)\sin(b_{LG}) + \cos(b)\cos(b_{LG})\cos(l - l_{LG})\big]. \tag{4.10}$$

4.4.1 Imaging Surveys

We next discuss the main characteristics of the imaging surveys used in this work. The details of the tests we have done on the magnitude scales, star-galaxy separation etc are given in Appendix B.

2MASS

2MASS (Skrutskie et al., 2006)) is a photometric survey in the NIR (J,H,K_s). The final eXtended Source Catalogue (2MASS-XSC) comprises of 1,647,459 galaxies over approximately the whole sky (99.998% sky coverage), with a photometric calibration varying by as little as 2-3% (Jarrett et al., 2003). 2MASS is currently thought to be magnitude complete to $K < 13.5$ (Bell et al., 2003; Chodorowski et al., 2008).

The 2MASS-XSC data used in this study comes from the `All-Sky Data Release' at the Infrared Processing and Analysis Center (IPAC) server. Galaxies have been included according to the following quality tags: `*cc_flg* $= 0$', `*cc_flg* $= Z$' to avoid contamination or confusion. The XSC catalogue consists solely of 2MASS objects with e-score and g-score < 1.4 to ensure the object really is extended and extragalactic.

It has been reported that the completeness and photometry of 2MASS-XSC galaxies with angular diameter greater than 10′ may be affected by the limit on the 2MASS scan size Jarrett et al. (2003). We have therefore applied a bright magnitude cut of K>10 for $n(m)$, $n(z)$ and $\overline{z}(m)$.

For the 2MASS survey, we shall use a corrected form (see Appendix B) of their extrapolated isophotal, *k_m_ext*, magnitude. This total type magnitude is based on an integration over the radial surface brightness profile. The lower radial boundary is defined by the isophotal μ = 20mag $arcsec^{-2}$ radius and an upper boundary by four disk scale lengths unless that is greater than 5 of the above minimum isophotal radii.

GAMA

The Galaxy And Mass Assembly (GAMA, Driver et al. (2009)) survey includes galaxies selected from UKIRT Infrared Deep Sky Survey - Large Area Survey (UKIDSS-LAS) and SDSS photometric targeting. It aims to create a catalogue of $\approx 350,000$ galaxies with comprehensive photometry from the UV band to the radio. GAMA DR1 is based on three 45deg^2 equatorial regions, chosen for their overlap with SDSS (stripes 9-12) and UKIDSS-LAS data. It comprises self consistent (ugrizJHK) imaging of 114,441 galaxies with 50,282 science quality redshifts.

As of GAMA DR1, only the Kron type K magnitude, *K_KRON* has been provided, and therefore we use this magnitude type. Whilst the NIR GAMA photometric data comes from UKIDSS, the final catalogue has been re-reduced for a variety of reasons outlined by Hill et al. (2011).

The GAMA data used here comes from the DR1 release, GAMACoreDR1, described by Driver et al. (2011) and archived at (`http://www.gama-survey.org/database/YR1public.php`). We have selected all galaxies in GAMA DR1, including those based on band specific detections.

SDSS

The Sloan Digital Sky Survey (SDSS, York et al. (2000)) covers $\approx$ $8500deg^2$ of the Northern sky in the u,g,r,i,z bands. As of DR9 the survey comprises 208,478,448 galaxies and is magnitude complete to r_{petro} <22.04.

For consistency, we have chosen to work with the same magnitude type for both spectroscopic and photometric SDSS samples. We therefore use the `cmodel' type magnitude as recommended by SDSS [3]. This total type magnitude is estimated by determining de Vaucouleurs or exponential profiles for each object in each band. The likelihood of either profile is then determined and the linear combination that best fits is then used to infer the total flux. A photometric sample has been selected using the quality criteria developed by Yasuda et al. (2001) for galaxy number counts. Namely, we reject saturated and non-primary objects and require a photometric classification as a galaxy in at least two of the g, r, i bands.

4.4.2 Redshift Surveys

Next we describe the main characteristics of the redshift surveys used in this work. In Appendix C we discuss the tests we have made on the magnitude dependent spectroscopic incompleteness of these surveys and how such effects can be corrected in the redshift distributions, $n(z)$.

6dFGS

The Six Degree Field Galaxy (6dFGS, Jones et al. (2004)) is a redshift survey over $\approx 17,000 deg^2$ i.e. most of the Southern sky, excluding $|b| < 10$. The survey was based on pre-existing overlapping survey photometry and was primarily selected in 2MASS K. The full survey comprises a catalogue of 125,071 galaxies with reliable redshifts. The survey has a median redshift of $z_{\text{median}} = 0.053$ (Jones et al., 2009) to its nominal limit of $K \leq 12.65$. We, however, shall be conservative and impose a $K < 12.5$ magnitude cut to minimise any completeness issues with the 6dFGS data. The 6dFGS data used in this study comes from the final DR3 release described in Jones et al. (2009) and is archived at (`http://www-wfau.roe.ac.uk/6dFGS/`). Galaxies have been included according to the following quality tags; *quality* ≥ 3, *quality* $\neq 6$.

It is historically relevant to note that the 6dFGS survey was started before the final 2MASS photometry was released. Intermediate 2MASS photometry at low galactic latitudes was relatively shallow and suffered from poor spatial resolution. To work around

[3] `https://www.sdss3.org/dr8/algorithms/magnitudes.php\#which\_mags`

this the 6dFGS team adopted a pseudo-total magnitude for redshift targeting. Other researchers used an alternative J-K inferred isophotal magnitude, hence referred to as a Cole type (Cole et al., 2001). With this type of estimator the less noisy J band is used to approach the true K band magnitude as $K_{cole} = J_{ext} - (J_{iso} - K_{iso})$. This type was indeed found to have greater accuracy compared to the accurate photometry of Loveday (2000). However, the final release of the 2MASS catalogue provided the total estimator, *k_m_ext* as described earlier. The 6dFGS team recommend this magnitude for science use. However, it remains the case that 6dFGS was targeted in a slightly different magnitude and that previous work has been conducted in a variety of magnitudes.

SDSS - Spectroscopic Survey

The spectroscopic sample was selected to a limit of $r_{petro} < 17.61$ finally comprising 1,457,002 confirmed galaxy redshifts, with a median redshift, $z_{\text{median}} = 0.108$. The SDSS spectroscopic sample was targeted on the basis of Petrosian magnitudes (Strauss et al., 2002). We however are working with the cmodel type magnitude for consistency with the SDSS photometric sample. To avoid selection and completeness effects we therefore work with the conservative magnitude limit r_{cmodel} <17.2.

We have also created a K limited SDSS spectroscopic sample by matching with 2MASS. The SDSS astrometric error is of order $\mathcal{O}(0.1'')$ (Hill et al., 2011; Finlator & et al., 2000) we therefore set a $1''$ matching limit. For this K limited SDSS sample we are in effect applying the multi-band selection that $K < 13.5$ and $r < 17.61$. This additional constraint does not bias the sample we select since even for a galaxy at the 2MASS limit it will require a relatively blue r-K colour of 4.11 to avoid selection in the joint sample. Indeed, Bell et al. (2003) found that at most 1% of galaxies were affected in a similar joint SDSS-2MASS sample.

The SDSS data used in this study come from the DR9 main sample described in Ahn et al. (2012) and is archived at (`http://skyserver.sdss3.org/CasJobs/`) In order to select a fair and high quality sample of galaxies we have used the following selection criteria; *class='GALAXY'*, *(zWarning = 0 OR ((zWarning*&$(4)) \geq 0)$, $legacy\_target1$&$(64|128|256)) \leq 0$, *mode=1* and *sciencеprimary=1*.

Survey	z_{median}	Mag limit	Area (deg^2)
6dFGS	0.053	$K_s < 12.5$	17000
SDSS-MAIN	0.108	$r < 17.61$	8500
GAMA	0.18	$r < 19.24$	150
2MASS	-	$K_s < 13.5$	$\sim$ Full Sky
SDSS-MAIN	-	$r < 22.04$	8500

Table 4.2: A summary of the properties of the redshift and imaging surveys used; (6dFGS, Jones et al. (2004)), (SDSS, York et al. (2000)) (GAMA, Driver et al. (2009)) and (2MASS, Jarrett et al. (2003)).

Field	RA (J2000)	DEC (J2000)	Area (deg^2)
6dFGS-NGC	[150,220]	[-40,0]	2578.03
6dFGS-SGC	[0-50,330-360]	[-50,0]	3511.29
SDSS-NGC	[150,220]	[0,50]	3072.38
GAMA G09	[129,141]	[-1,3]	47.98
GAMA G12	[174,186]	[-2,2]	47.99
GAMA G15	[211.5,223.5]	[-2,2]	47.99

Table 4.3: A summary of the main geometric properties of the Target fields used.

4.4.3 Target Fields

Three fields were chosen to cover most of the northern and southern galactic caps at high latitudes while maintaining the basic division between the northern SDSS and southern 6dFGS redshift survey areas, as shown in Fig. 4.1 and Tables 4.2 and 4.3. The three fields are termed SDSS-NGC, 6dFGS-NGC and 6dFGS-SGC as shown in Fig. 4.1. These fields contain various regions of interest. The 6dFGS-NGC contains the CMB Local group dipole pointing, the direction of Great Attractor and the Shapley-8 supercluster. The 6dFGS-SGC region contains the Perseus-Pisces supercluster, whilst the SDSS-NGC region contains the Coma cluster.

4.5 Redshift Distributions

We first probe the local galaxy clustering environment directly via galaxy redshift distributions. Fig. 4.2 shows the $n(z)$ distributions consistently limited at $K < 12.5$ for our three target regions. Here we are using 2MASS magnitudes matched to 6dFGS redshifts in the case of 6dFGS-NGC and 6dFGS-SGC data and SDSS redshifts in the case of SDSS-NGC. Errors have been estimated from jack-knife errors within the 3 target regions. The red lines shows the homogeneous $n(z)$ model estimated assuming the Metcalfe et al. (2001) LF and the K plus E corrections as outlined in Section 4.3. These models have been normalised so as to maintain the $K < 12.5$ $n(m)$ underdensities stated in Table 4.4 and corrected for redshift incompleteness (including any dependence of incompleteness on magnitude) using the method described in Appendix C.

We then divided the observed $n(z)$ by this suitably normalised homogeneous model to see over- and under-densities directly as a function of redshift. The results are shown in Fig. 4.3 and the significant non-uniformity we see reflects the presence of LSS in our local universe. With this $K < 12.5$ normalisation all three regions are typically underdense for $z < 0.05$ - see Table 4.4. The 6dFGS-SGC region, which corresponds to the Automatic Plate Measuring (APM) area (Maddox et al., 1990), is the most underdense at $40 \pm 5\%$. The error here comes from jack-knife estimates. The SDSS-NGC region is also significantly underdense at the $14 \pm 5\%$ level. While the 6dFGS-NGC region still shows under-density, it is not significantly so ($4 \pm 10\%$). The error is bigger here because of the influence of the Shapley-8 supercluster in this region. Therefore on scales out to ≈ 150h^{-1}Mpc we conclude that the redshift distributions are consistently underdense by $\approx 4 - 40\%$ with the South Galactic cap showing the biggest under-density.

Clearly a lot depends on the accuracy of the $n(K)$ model normalisation. Frith et al. (2006) argued on the basis of a comparison of 2MASS $H < 12.5$ magnitude counts to much fainter counts from Calar Alto OmegaCAM that the Metcalfe et al. (2001) LF model normalisation was supported by these data. However, this count was only based on an area of $0.25 deg^2$. In Section 4.6.2 we shall test if this normalisation is consistent with the new K band galaxy count data from the much bigger $150 deg^2$

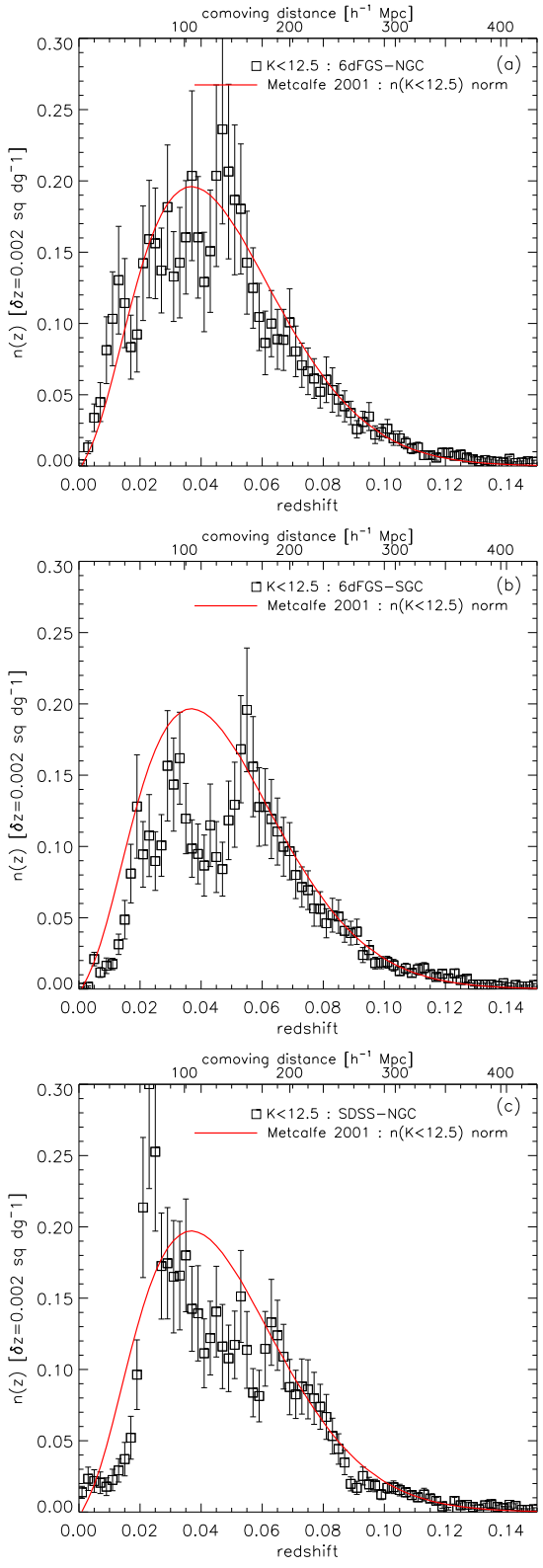

Figure 4.2: K band galaxy $n(z)$ with $K < 12.5$ and $\delta z = 0.002$ normalised using the $K < 12.5$ galaxy number counts. The red line represents the homogeneous Metcalfe et al. (2001) LF prediction. The points (black, square) show data with jack-knife derived errors. a) 6dFGS-NGC region (6dFGS, galactic north), b) 6dFGS-SGC region (6dFGS, galactic south), c) SDSS-NGC (SDSS-2MASS, galactic north).

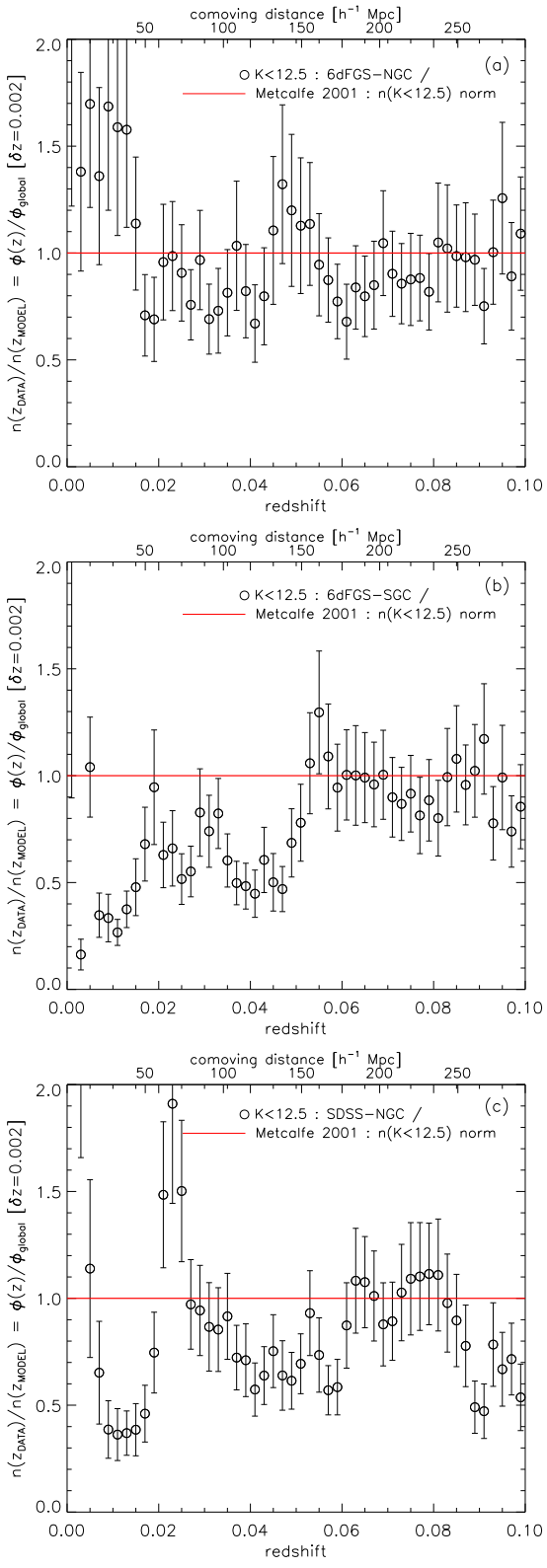

Figure 4.3: K band galaxy $\phi^*(z)/\phi_{\text{global}}$ with $K < 12.5$ and $\delta z = 0.002$ normalised using the $K < 12.5$ galaxy number counts. The red line represents the homogeneous Metcalfe et al. (2001) LF prediction. The points (black, circle) show data with jack-knife derived errors. a) 6dFGS-NGC region (6dFGS, galactic north), b) 6dFGS-SGC region (6dFGS, galactic south), c) SDSS-NGC (SDSS-2MASS, galactic north).

area of the GAMA survey.

It is also still possible that a larger-scale under-density persists beyond $z = 0.05$ out to $z \approx 0.1$. The underdensities then vary between 6-25% as seen in Table 4.4. We find a weighted average under-density of $15 \pm 3\%$ for $K < 12.5$ (with or without a $z < 0.1$ cut). Certainly a similar conclusion was reached by Frith et al. (2005a) who had the advantage of the 2dFGRS $n(z)$ which reached fainter magnitudes and higher redshifts but only covering a significantly smaller region of sky. Again, the $n(z)$ model normalisation is even more crucial in measuring any under-density at $0.05 < z < 0.1$ because a lot depends on the position of the homogeneous model (red line) in Fig. 4.4. This can be probed both by galaxy counts to $K = 15.8$ in the 150 deg^2 GAMA regions and $n(z)$ to $K = 13.5$ by virtue of the deeper redshift survey data in the SDSS-NGC regions. But first we return to check that our $n(z)$ results are consistent with the *form* of the number counts to $K = 13.5$.

4.6 Number Counts

4.6.1 2MASS galaxy counts to $K = 13.5$

Fig. 4.4 show the number counts to $K < 13.5$ for our 3 regions. In Appendix B we check for a scale-error in the 2MASS magnitudes and the statistics of star-galaxy separation as function of magnitude. In fact, we do find a marginal scale error between $10 < K < 13.5$ and all the magnitudes in Fig. 4.4 have been corrected for this scale error. With or without this correction, all fields exhibit an under-density relative to the homogeneous prediction (red line) until at least $K \approx 12.5$ and any convergence is only seen when the counts reach $K = 13.5$.

Using the $\phi^*(z)/\phi_{\text{global}}$ correction for radial inhomogeneity found earlier we show the LSS corrected model counts as the green line in Fig. 4.5 where observed counts have been normalised by the homogeneous model. We see that accounting for the inhomogeneities in the $n(z)$ in Fig. 4.3 has improved the model fit. This suggests a consistency between variations in the $n(z)$ and $n(m)$ and a mutual agreement in the redshift under-density reported in Section 4.5.

These under-densities are either due to poor normalisation of the models at fainter

Field	Sample limit	Under-density
6dFGS-NGC	$z < 0.05$	0.96 ± 0.10
6dFGS-SGC	$z < 0.05$	0.60 ± 0.05
SDSS-NGC	$z < 0.05$	0.86 ± 0.05
6dFGS-NGC	$z < 0.1$	0.94 ± 0.07
6dFGS-SGC	$z < 0.1$	0.75 ± 0.04
SDSS-NGC	$z < 0.1$	0.86 ± 0.04
6dFGS-NGC	$K < 12.5$	0.96 ± 0.07
6dFGS-SGC	$K < 12.5$	0.76 ± 0.03
SDSS-NGC	$K < 12.5$	0.88 ± 0.03
6dFGS-NGC	$K < 13.5$	1.03 ± 0.04
6dFGS-SGC	$K < 13.5$	0.92 ± 0.02
SDSS-NGC	$K < 13.5$	0.97 ± 0.02
SDSS-NGC	$r < 17.2$	0.96 ± 0.02

Table 4.4: A summary of the number count normalisations derived using the homogeneous Metcalfe et al. (2001) LF prediction. These also correspond to under- and over-densities to the specified limits. The $z < 0.05$ and $z < 0.1$ entries assume $K < 12.5$.

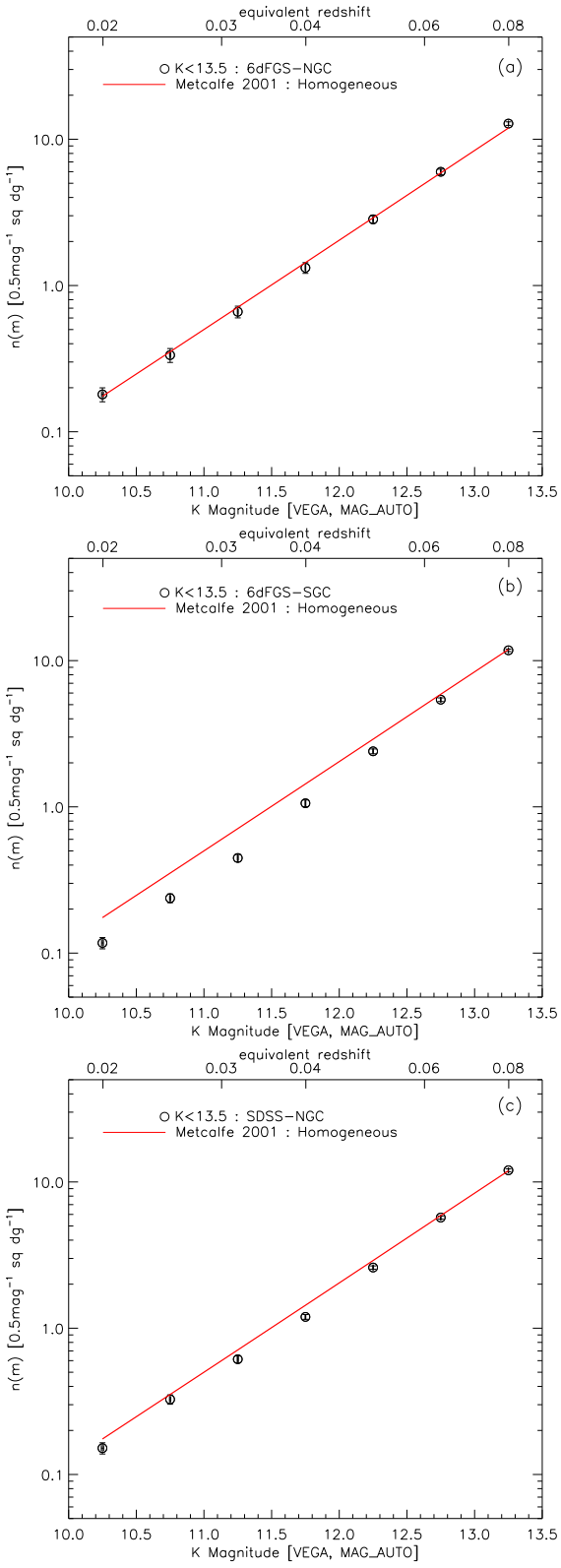

Figure 4.4: K band galaxy $n(m)$ from the 2MASS survey with $\delta m = 0.5$. The red line represents the homogeneous Metcalfe et al. (2001) LF prediction. The points (black, circle) show data with jack-knife derived errors. a) 6dFGS-NGC region (6dFGS, galactic north), b) 6dFGS-SGC region (6dFGS, galactic south), c) SDSS-NGC (SDSS-2MASS, galactic north).

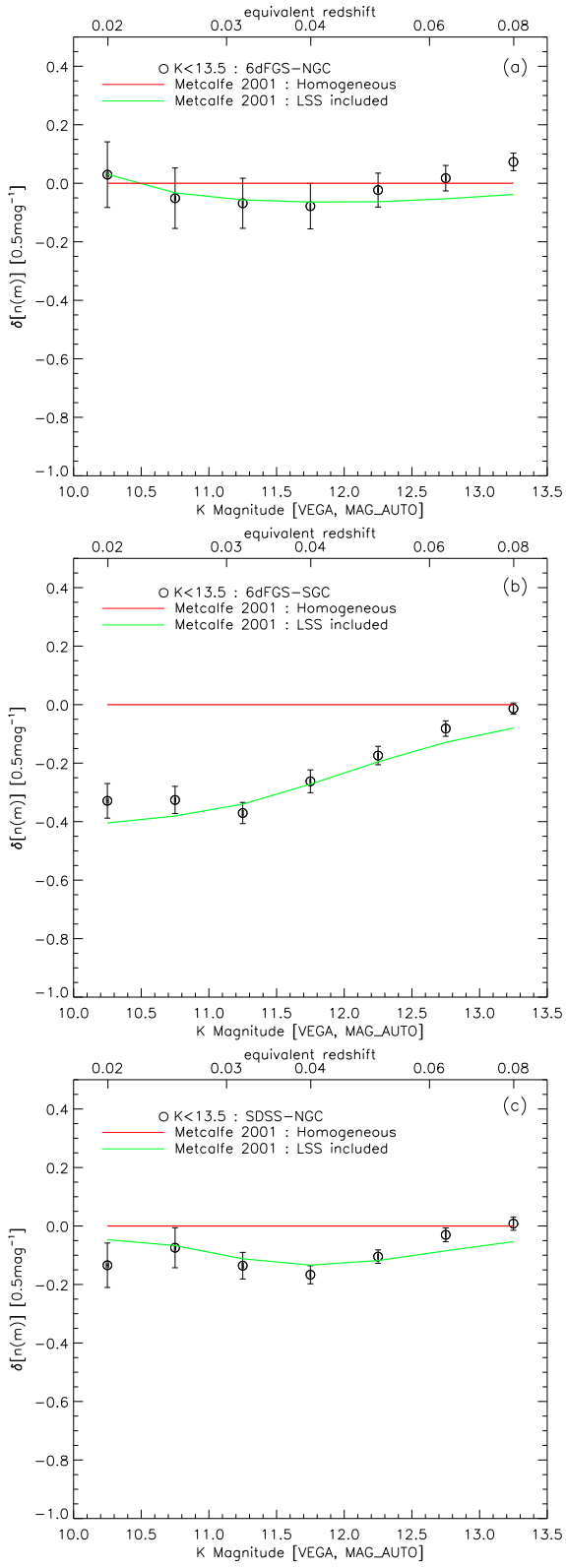

Figure 4.5: K band galaxy $n(m)$ density contrast from the 2MASS survey with $\delta m = 0.5$. The red line represents the homogeneous Metcalfe et al. (2001) LF prediction and the green line the LSS-corrected Metcalfe et al. (2001) LF prediction. The points (black, circle) show data with jack-knife derived errors. a) 6dFGS-NGC region (6dFGS, galactic north), b) 6dFGS-SGC region (6dFGS, galactic south), c) SDSS-NGC (SDSS-2MASS, galactic north).

magnitudes, evolutionary brightening of galaxies at $z \approx 0.1$ or large-scale inhomogeneities. Note that the above scale error correction tends to make the $K = 13.5$ galaxy counts ≈ 0.05mag brighter, slightly improving the fit to the homogeneous model. The generally improved agreement between LSS corrected model and observed counts argues that the steep number count slopes are not caused by systematics in the magnitudes or in star-galaxy separation.

However, in all three regions the number counts are only becoming consistent with homogeneity at the $K = 13.5$ 2MASS survey limit, rather than the $K = 12.5$ limit we used for the $n(z)$. This leaves the possibility open that the under-density may extend beyond the scales we have used in our LSS corrections and that the local volume remains underdense beyond $\approx 150-300$h^{-1}Mpc. We interpret the consistency between $n(m)$ and $n(z)$ as evidence for a local hole-like under-density at least out to $z \approx 0.08$.

4.6.2 Deeper K counts from GAMA

We next use the GAMA survey over the full $3 \times 48 deg^2$ regions surveyed by the GAMA project to test the overall normalisation of the homogeneous models for $n(z)$ and $n(m)$. We first calibrate the GAMA K Kron magnitudes to the 2MASS K k_m_ext magnitude scale by comparing the galaxy photometry. Using the `*mpfitexy*' routine we find that all three GAMA regions are consistent with a one-to-one relation at $\approx 1\sigma$ as shown in Fig. B.3. However, again using the `*mpfitexy*' routine we find and apply the ≈ -0.02mag zeropoint offsets detailed in Table B.1.

We therefore compare the GAMA K counts and the 3 GAMA fields of 2MASS galaxy counts to the homogeneous models of Metcalfe et al. (2001) in Fig. 4.6. We see that the model fits the data well in the range $14 < K < 15.5$, supporting the normalisation we have used from Table 4.1. The sensitivity to different LF's is shown using the Cole et al. (2001) LF, here we see this LF is not appropriately normalised to the faint K band counts unlike the Metcalfe et al. (2001) LF. We therefore conclude that the Metcalfe et al. (2001) normalisation we have used is reinforced by the deeper K galaxy counts in the $150 deg^2$ of the GAMA region.

We have also included an alternative homogeneous model with the same underlying

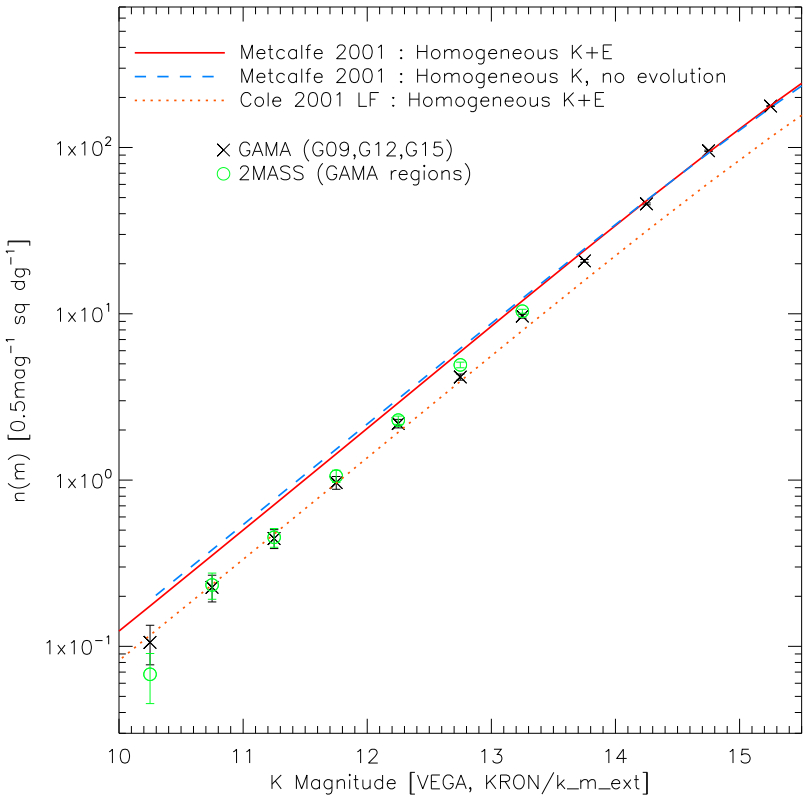

Figure 4.6: K band galaxy number counts comparing GAMA and 2MASS over the GAMA regions. The red line represents the homogeneous Metcalfe et al. (2001) LF prediction which at deep magnitudes is well normalised to the galaxy number counts. The blue dashed line shows the homogeneous Metcalfe et al. (2001) LF prediction without evolution corrections whilst the yellow dotted line shows the homogeneous Cole et al. (2001) LF prediction. The points show the 2MASS (green, circle) and GAMA (black, cross) data with Poisson errors.

LF but without any evolutionary corrections so as to illustrate modelling uncertainties. The relative insensitivity of the model to evolutionary corrections is reflective of the significant advantage of working in the K band.

4.7 $N(z)$ to $K = 13.5$ and r$= 17.2$ in the SDSS-NGC region

It is possible to go to deeper z-survey limits in the SDSS-NGC region because of the fainter magnitude limit in this region, compared to 6dFGS. Figs. 4.7 and 4.8 show the $n(z)$ and $\phi^*(z)$ for this region to the $K = 13.5$ limit of 2MASS. We normalize the $n(z)$ by the 96% ratio of data-model number magnitude counts in this region to this limit - see Table 4.4. We note that the same basic features in $n(z)$ are seen at low redshift but new over- and under-densities appear at higher redshift. We note particularly the peak at $z \approx 0.08$. We see that it takes to $z \approx 0.13$ before the model fits the data. Indeed, the K band counts in Fig. 4.4(c) only appear to converge at $K = 13.5$. We checked the difference that a no-evolution model made to the $n(z)$ fit and it was small. The no-evolution $n(K)$ model is also little different from the evolutionary model. The advantage of the K band is that it is less susceptible to evolutionary uncertainties.

Nevertheless, we also present the full $n(z)$ to $r = 17.2$ in the SDSS-NGC region. Here the $n(z)$ results are slightly more ambiguous. The $n(z)$ evolutionary model is compared to the data in Figs. 4.9 and 4.10. The normalisation factor to $r < 17.2$ from the $n(r)$ is 0.96 ± 0.02. The $r < 17.2$ $\phi(z)$ again shows evidence for under-density but here the observed $\phi^*(z)$ generally is flatter, decreasing more slowly towards $z = 0$ than in K. Also it shows less indication of convergence at $z \approx 0.1$.

Clearly the normalising factor inferred from the r-band count is crucial here and we show $n(r)$ to $r < 22$ for the SDSS-NGC region in Figs. 4.11 and 4.12. These counts are consistent with the Yasuda et al. (2001) analysis of the SDSS commissioning data for the magnitude range $15 < r < 20$. A similar behaviour is seen in Fig. 4.12 as in Fig. 4.10 in that the observed $n(r)$ takes till $r \approx 20$ to reach the homogeneous model. This is reinforced by the approximate agreement of the counts with LSS corrected model based on the $r < 17.2$ $n(z)$. Thus there is at least consistency between the suggestions from $n(z)$ and $n(m)$ for the under-density extending beyond $z = 0.1$.

Furthermore, there is uncertainty caused by the increased possibility of evolution in the r band. A no-evolution model for $n(m)$ is therefore also shown in Fig. 4.11. This model has a flatter slope and therefore reaches agreement with $n(r)$ at a brighter

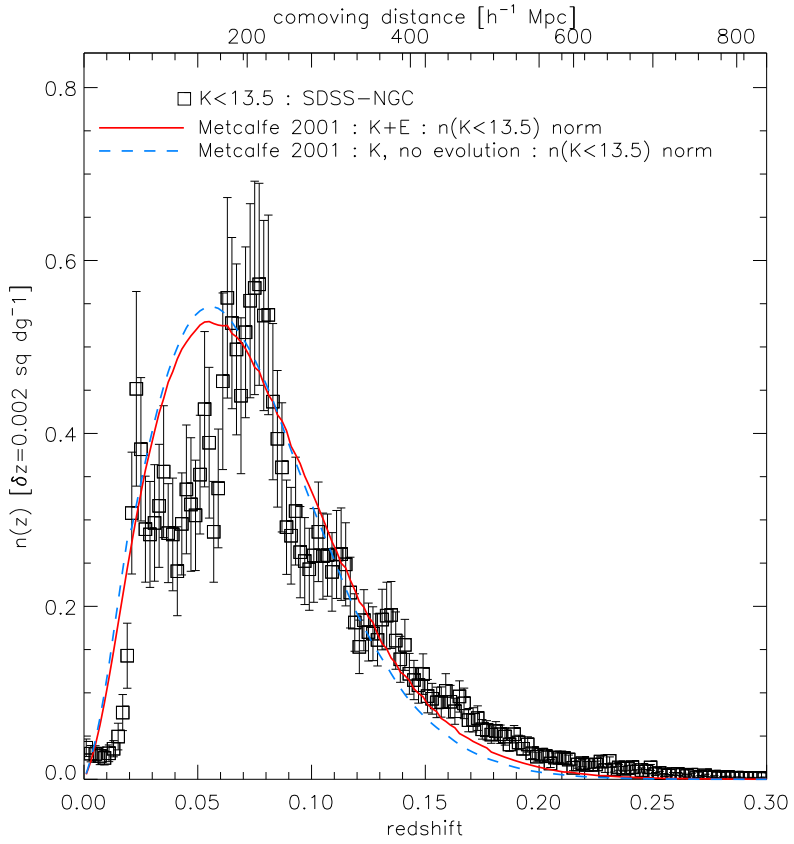

Figure 4.7: K band galaxy $n(z)$ with $K < 13.5$ and $\delta z = 0.002$ normalised using the $K < 13.5$ galaxy number counts. The red line represents the homogeneous Metcalfe et al. (2001) LF prediction The points (black, square) show the SDSS-NGC data with jack-knife derived errors.

$r = 19$ magnitude. Thus here there would be stronger evidence for a void within say 150h^{-1}Mpc but the evidence for a more extended under-density would be less than with the evolutionary model. It should also be noted that within the classes of models considered here, an evolutionary model gives a better fit to $n(r)$ at $r > 20$.

Uncertainties in the count normalisation and the evolutionary model thus appear to be more significant in the r band and this reinforces the advantage of working in K. The K band counts may also be more sensitive to over- and under-densities, being more dominated by strongly clustered early-type galaxies. We conclude that the evidence in the K band for a local hole out to 300h^{-1} Mpc can be regarded as more reliable than the more ambiguous evidence for a flatter under-density to greater distances from the $r < 17.2$ $n(z)$.

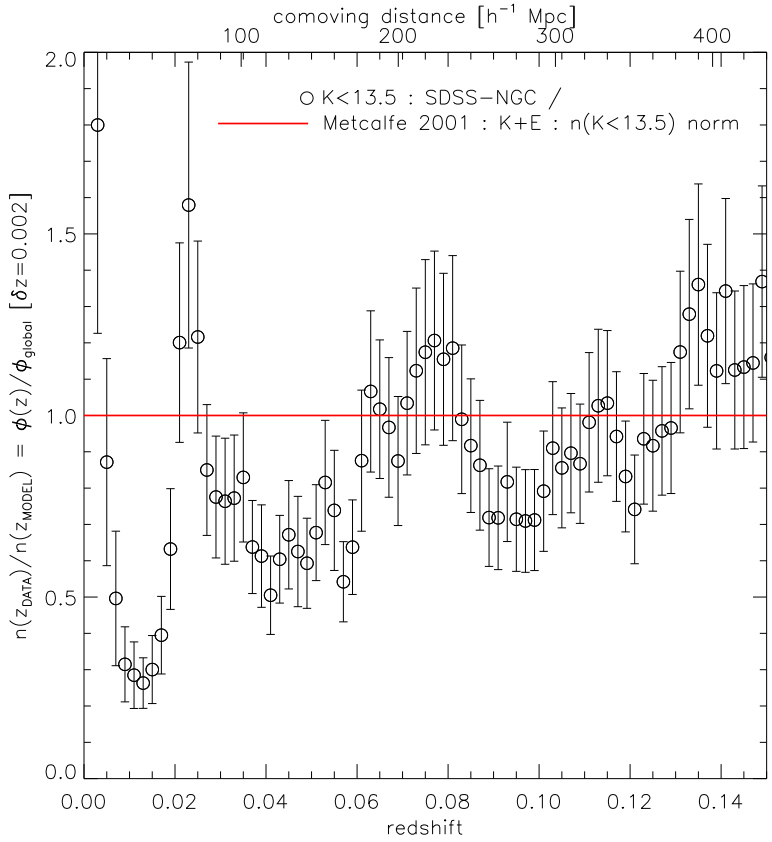

Figure 4.8: K band galaxy $\phi^*(z)/\phi_{\text{global}}$ with $K < 13.5$ and $\delta z = 0.002$ normalised using the $K < 13.5$ galaxy number counts. The red line represents the homogeneous Metcalfe et al. (2001) LF prediction. The points (black, circle) show the SDSS-NGC data with jack-knife derived errors.

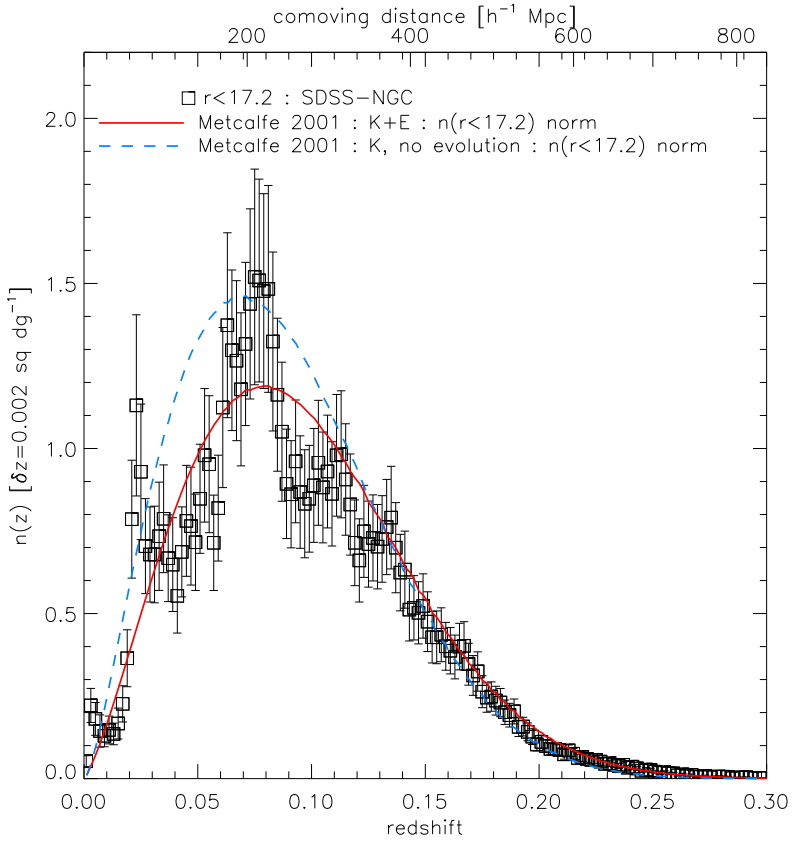

Figure 4.9: r band galaxy $n(z)$ with $r < 17.2$ and $\delta z = 0.002$ normalised using the $r < 17.2$ galaxy number counts. The red line represents the homogeneous Metcalfe et al. (2001) LF prediction. The points (black, square) show the SDSS-NGC data with jack-knife derived errors.

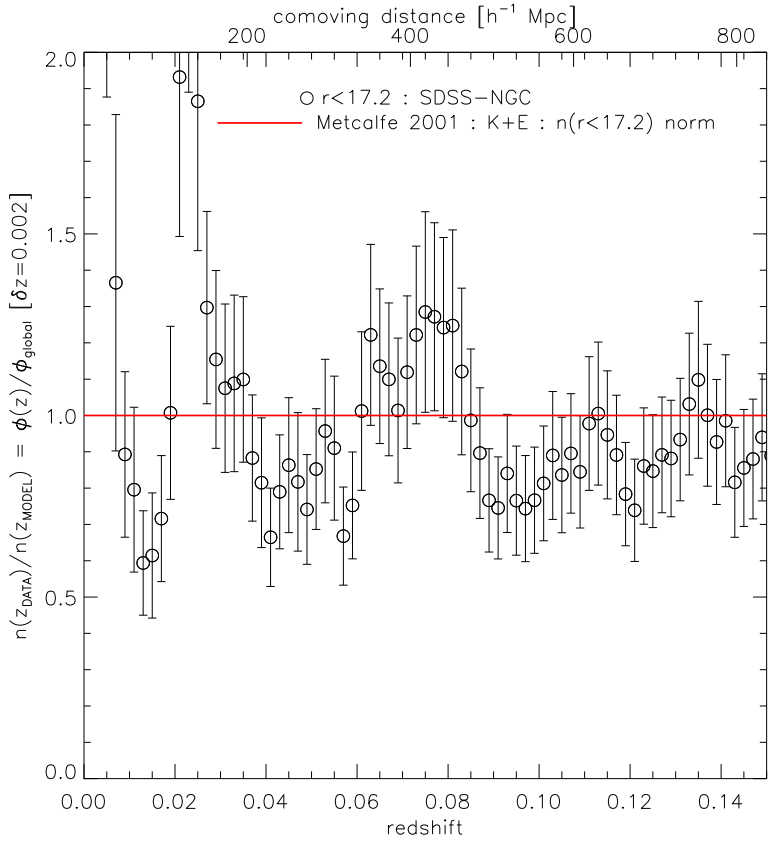

Figure 4.10: r band galaxy $\phi^*(z)/\phi_{\text{global}}$ with $r < 17.2$ and $\delta z = 0.002$ normalised using the $r < 17.2$ galaxy number counts. The red line represents the homogeneous Metcalfe et al. (2001) LF prediction. The points (black, circle) show the SDSS-NGC data with jack-knife derived errors.

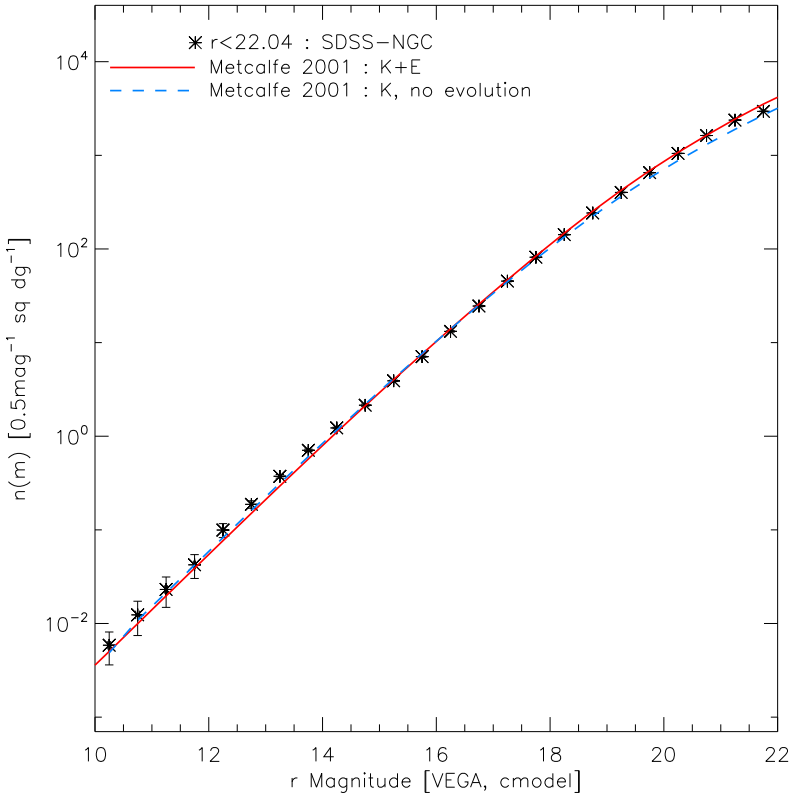

Figure 4.11: r band galaxy $n(m)$ with $\delta m = 0.5$. The red line represents the homogeneous Metcalfe et al. (2001) LF prediction and the blue line the no-evolution homogeneous Metcalfe et al. (2001) LF prediction. The points (black, asterix) show the SDSS-NGC data with jack-knife derived errors.

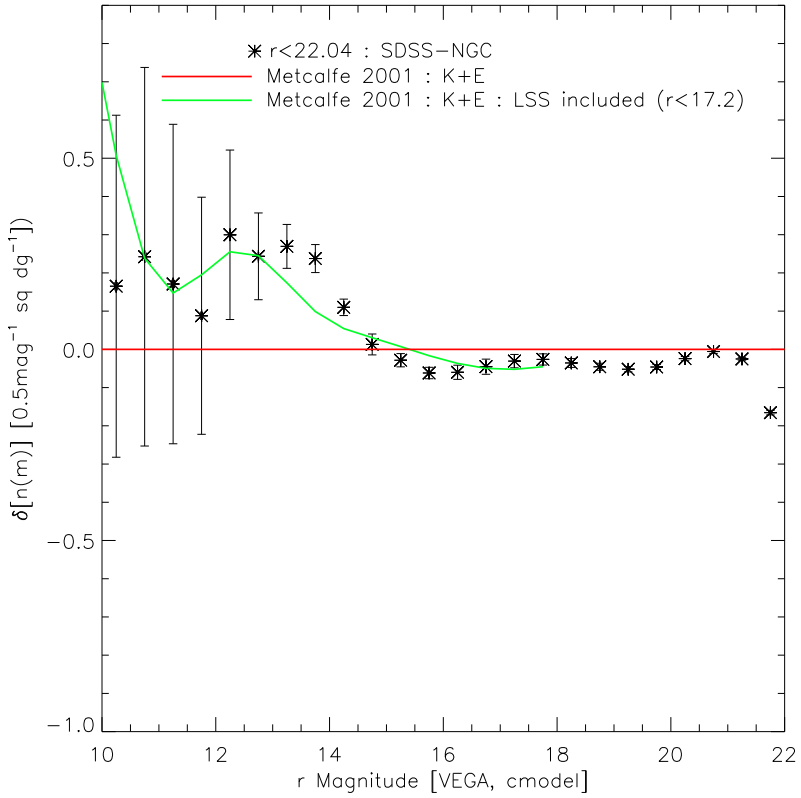

Figure 4.12: r band $n(m)$ based density contrast with $\delta m = 0.5$. The red line represents the homogeneous Metcalfe et al. (2001) LF prediction and the green line the LSS-corrected Metcalfe et al. (2001) LF prediction. The points (black, asterix) show the SDSS-NGC data with jack-knife derived errors.

4.8 The Hubble Diagram

Fig. 4.13 shows $\overline{z}(m)$ for our three fields. The homogeneous prediction for each region is shown as the red line and the LSS corrected model, based on the $\phi^*(z)$ found earlier, is shown as the green line. In all three cases we see that the green line gives an improved, although not perfect, fit to the data. But the importance of the LSS correction is clear since the under-prediction of the observed $\overline{z}(m)$ particularly in the 6dFGS-SGC region might otherwise be interpreted as immediately implying peculiar motion which is clearly not the case. As expected, the 6dFGS-SGC region shows the biggest LSS (red-green) correction between the 3 regions since it showed the biggest low-redshift under-density in Fig. 4.3 but the other two regions also tend to behave similarly. We also note the tentative `spike' in $\overline{z}(m)$ in the 6dFGS-NGC region at $K \approx 11.5$, which is the approximate location of the Shapley-8 supercluster. But even with $\delta m = 0.1$mag bins, this technique does not have the resolution to detect backside infall etc.

To examine these $\overline{z}(m)$ relations in more detail, we next subtract the LSS corrected `Hubble law' prediction from the data in Fig. 4.13. This means we are in effect plotting $v_{pec}$. The results are shown in Fig. 4.14 for a magnitude bin of $\delta m = 0.5$. For comparison purposes we also show the $\overline{z}(m)$ for the final $K = 12.25$ bin when using the original 2MASS `k_m_ext' magnitude and without the spectroscopic completeness corrections described in Appendix C. The difference between these results means we cannot place too much weight on this final bin when interpreting these data.

Since the models indicated by the green lines assume galaxies are at rest in the Local Group frame then this is tantamount to assuming that all galaxies and the Local Group are moving with a coherent bulk notion. We now investigate an alternative hypothesis that the Local Group is moving with 633kms^{-1} relative to more distant galaxies i.e. the CMB dipole motion in the Local Group frame. The relative average recession velocity of these distant galaxies should then be correspondingly reduced in the direction of our motion relative to the CMB and increased in the opposite direction. This `dipole' non-bulk motion model is then represented by the blue lines in Fig. 4.14.

We immediately see that in two out of three regions the bulk motion prediction agrees with the data much better than the non-bulk motion model where only the

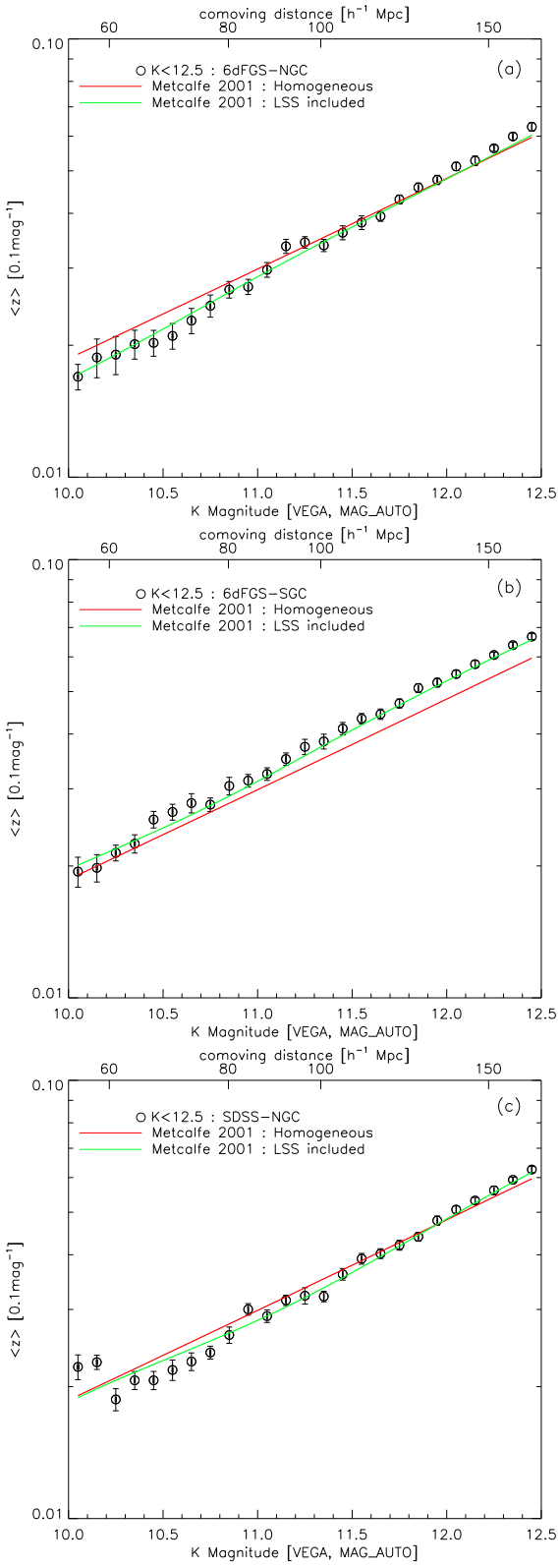

Figure 4.13: K band $\overline{z}(m)$ with $\delta m = 0.1$. The red line represents the homogeneous Metcalfe et al. (2001) LF prediction and the green line the LSS-corrected Metcalfe et al. (2001) LF prediction. The points (black, circle) show data with jack-knife derived errors. a) 6dFGS-NGC region (6dFGS, galactic north), b) 6dFGS-SGC region (6dFGS, galactic south), c) SDSS-NGC (SDSS-2MASS, galactic north).

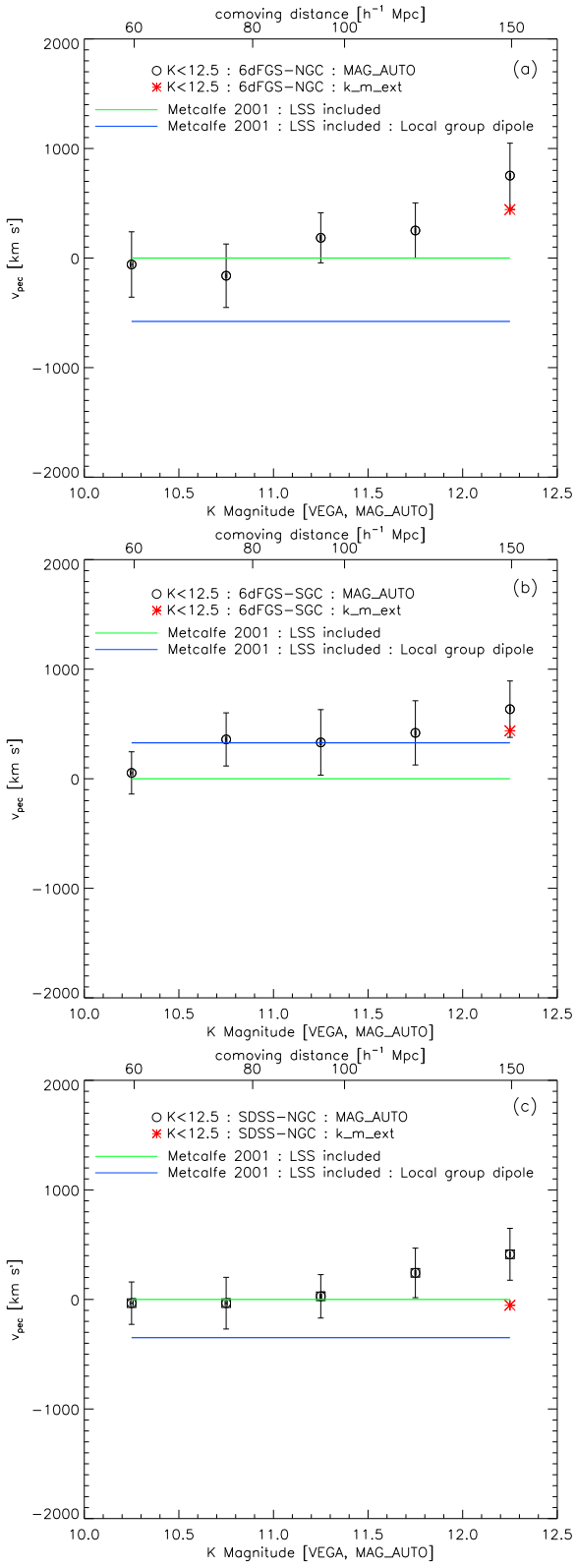

Figure 4.14: K band $\overline{z}(m)$ with $\delta m = 0.5$. The green line represents the LSS-corrected Metcalfe et al. (2001) LF prediction and the blue line the CMB dipole flow LSS-corrected Metcalfe et al. (2001) LF prediction. The points (black, circle) show data with jack-knife derived errors. The red asterisk shows the final bin without corrections. a) 6dFGS-NGC region (6dFGS, galactic north), b) 6dFGS-SGC region (6dFGS, galactic south), c) SDSS-NGC (SDSS-2MASS, galactic north).

Local Group is moving with 633kms^{-1} with respect to the CMB. Even in the third region in the 6dFGS SGC direction, although the data agrees better with the non-bulk motion model, it is also still in reasonable agreement with the bulk motion model. The significance of the rejection of the non-bulk motion model has been estimated using the $K = 11.75$ bin. This is necessary as the smoothing by the galaxy luminosity function causes different magnitude bins to be highly covariant and also the final bin may be less reliable as discussed above. The level of rejection of the non-bulk motion model in the 6dFGS-NGC and SDSS-NGC regions is at the 3.1σ and 2.3σ levels respectively. This suggests that at least in the 6dFGS-NGC and SDSS-NGC directions we may be seeing a bulk motion with convergence to the CMB dipole not yet reached at our $K < 12.5$mag survey limits. Combining the measurements across all three regions we find a overall rejection of the non-bulk motion model at the 3.9σ level. In contrast, the bulk motion model is consistent with the data overall at the 1.5σ level. The fit of the bulk motion model indicates that the scale of convergence is larger than the ≈ 150h^{-1}Mpc scale probed at $K < 12.5$. However, it should be noted that the residual dipole effect is small relative to the LSS correction.

It is somewhat counter-intuitive that the regions which are less underdense on average (6dFGS-NGC, SDSS-NGC) agree with the bulk motion model whilst the most underdense region (6dFGS-SGC) agrees with the dipole based non-bulk motion model. However, this might be consistent with a faster local expansion in the most underdense area. In this view the agreement of 6dFGS-SGC $\overline{z}(m)$ with the non-bulk motion model (blue line) would be accidental with the real interpretation being a bulk motion (green line) combined with a faster local expansion resulting in an excess v_{pec} as is observed. We note that in the other two regions there is at least no inconsistency with a faster local expansion rate relative to the bulk motion model. But it should still be noted that our simple models do not include peculiar velocities generated by structures like Shapley-8 in 6dFGS-NGC which would produce apparently higher expansion rates even beyond their nominal redshift, due to the smoothing of $\overline{z}(m)$ by the galaxy luminosity function.

We conclude that the successful fit of a bulk motion model fit to $\overline{z}(m)$ may be consistent with the $\approx$150h^{-1}Mpc scale coherent under-density found in $n(z)$ and $n(m)$ across our three regions. The question of whether the 300h^{-1}Mpc void is visible

dynamically in $\overline{z}(m)$ is less clear because that statistic does not reach $z \approx 0.1$. Clearly the SNIa Hubble diagram probes out to larger redshifts where it is a more probable standard candle than our galaxy samples. The question then of whether there is dynamical evidence of a Local Hole is of course intertwined with the cosmological model that is assumed.

4.9 Conclusions

We have used $n(m)$ from 2MASS and $n(z)$ from 6dFGS and SDSS limited at $K < 12.5$ over much of the sky at high galactic latitudes to probe the local large-scale structure, extending the work of Frith et al. (2005b). We looked at three volumes and found that that in the 6dFGS-SGC region, which broadly corresponds to the area previously covered by the APM survey, there is a clear $\approx 40\%$ under-density out to 150h^{-1}Mpc. In the SDSS-NGC volume an $\approx 15\%$ under-density is seen again out to 150h^{-1}Mpc although this is broken by the Coma cluster producing a strong over-density at ≈ 75h^{-1}Mpc in front of large under-densities behind it. A $\approx 5\%$ under-density is seen in the 6dFGS-NGC area out to about 150h^{-1}Mpc. The implied local under-density in $n(z)$ and $n(m)$ averaged over the 3 fields out to $K < 12.5$ is $\approx 15 \pm 3\%$. Modelling the K number counts using the ratio of a homogeneous model normalised to these over- and under-densities to define $\phi^*(z)$, produced good agreement with the under-densities seen in the number counts to $K = 12.5$, particularly in the 6dFGS-SGC area. This agreement between $n(m)$ and $n(z)$ supports the reality of these local inhomogeneities out to ≈ 150h^{-1}Mpc depth.

While ΛCDM may allow structures on 200-300h^{-1}Mpc scales (Yadav et al., 2010; Park et al., 2012; Watson et al., 2013), Frith et al. (2005b) calculated that a 24% under-density to $K < 12.5$ over the 4000deg^2 APM (6dFGS-SGC) area would be inconsistent with the ΛCDM model at the 4-4.5σ level, depending on whether the calculation was based on a theoretical ΛCDM or observed 2MASS $w(\theta)$ - see their Table 1. However, when these authors take into account the previous uncertainties in the K band count normalisation, this significance then reduced to 2-3σ. Here, we have confirmed the 6dFGS-SGC under-density to be $24 \pm 3\%$ at $K < 12.5$ in only a slightly smaller area (3511deg^2) and further confirmed that our number count normalisation is accurate

from the deeper GAMA data, in an area $\approx 600\times$ larger than that available to Frith et al. (2005b). So the existence of such a coherent under-density in the South Galactic cap appears to imply an $\approx 4\sigma$ discrepancy with the ΛCDM model, in terms of the large-scale power that it predicts.

The use of the luminosity function of Metcalfe et al. (2001) is a potential area of weakness in these studies. However, in Whitbourn (2013) we use maximum likelihood techniques to estimate the luminosity function and $\phi^*(z)$ simultaneously for the r and K limited samples. They find that our assumed luminosity function is either in good agreement with the self-consistently estimated luminosity function (r-band) or where it differs slightly (K-band) the $\phi^*(z)$ results prove robust and unaffected. In any case, for the K-band, the density profiles as derived using alternative LF's such as Cole et al. (2001), as normalised to the respective number counts, are only marginally different.

The three fields studied here are wide-field, with each representing $\approx 1/15$ of the sky. However, they are considerably smaller than the full sky 2MASS sample from which they are drawn. We have therefore investigated whether these regions are typical and hence representative of the full sky by considering the redshift distribution of the 2MRS, a recently released spectroscopic companion to 2MASS which is complete to the shallower depth of $K \approx 11.25$ (Huchra et al., 2012). We find both that the density profiles in these regions are representative in terms of the variation observed across the sky in the 2MRS sample. Equally, the number density flucations in these regions are not exceptional with respect to estimates of cosmic-variance (as derived using the `cosmicvariance' routine from the Cosmology Routine Library [4]). Indeed, there seems to be mild evidence that the 6dFGS-NGC and SDSS-NGC fields are $\approx 1\sigma$ overdense compared to the expectation for fields of their size in the 2MRS survey.

We then made a Hubble diagram using the $\overline{z}(m)$ technique of Soneira (1979). Before we could detect peculiar velocities we had to make LSS corrections to make the model for $\overline{z}(m)$ take account of the inhomogeneities already found. In the 6dFGS-SGC region we found that the LSS-corrected $\overline{z}(m)$ prefers a solution that includes a 633kms^{-1} CMB velocity component for the Local Group relative to galaxies in this direction. In the 6dFGS-NGC and SDSS-NGC regions the more distant galaxies still preferred

[4] http://www.mpa-garching.mpg.de/~komatsu/CRL/fluctuation/erroronmeandensity/cosmicvariance

the solution without the CMB velocity added to the Local Group and so can be said to prefer a bulk motion solution where the local motion towards the CMB dipole direction has not converged.

The local under-densities we have found will imply faster local expansions. Indeed, we noted that such a scenario is not inconsistent with the results we found with $\overline{z}(m)$. Such a faster local expansion could help alleviate the tension at the $\approx 5\%$ level between recent local and CMB measures of H_0 (Planck Collaboration, 2013c). The naive expectation for the effect on H_0 can be derived by assuming linear theory, $\delta H_0/H_0 = -\frac{1}{3}\Omega_m^{0.6}/b \times \delta\rho_g/\rho_g$ where the bias, $b \approx 1$, for the standard model. Then the $15 \pm 3\%$, $z < 0.05$, $K < 12.5$, under-density we report suggests an $\approx 2 - 3\%$ increase in H_0. Indeed, this level of variation is not inconsistent with estimates of the cosmic variance of H_0 in ΛCDM (Kalus et al., 2013; Marra et al., 2013; Wojtak et al., 2013). However, for the Southern Galactic cap region where we found a deeper underdensity of $\approx 40\%$, a larger H_0 correction of $6 - 7\%$ would be implied.

Finally, we investigated the evidence for an even larger local under-density out to $\approx 300\mathrm{h}^{-1}$Mpc. We first determined the $n(m)$ normalisation at fainter $K \approx 16$mag and $r \approx 20.5$mag from GAMA and SDSS. We found excellent agreement with the K model counts at $K \approx 15$. This normalisation implies that the under-density in the SDSS-NGC volume may extend to $\approx 300\mathrm{h}^{-1}$Mpc and even deeper if the SDSS-NGC $r < 17.2\, n(z)$ is to be believed. However, there is increased uncertainty in r due to the likelihood of increased evolutionary effects as well as the count model normalisation uncertainty. Although $\overline{z}(m)$ at these limits cannot test further this $300\mathrm{h}^{-1}$Mpc under-density dynamically, we have noted that any cosmology that fits the SNIa Hubble diagram before accounting for the Local Hole must fail at some level afterwards.

Chapter 5 | *Conclusions*

In this thesis we have investigated how observations of LSS can be used to test the validity of the ΛCDM model. In particular, we have studied:

- Whether foreground contaminants in the *WMAP* CMB temperature maps provide any evidence for instrumental effects or tension with X-ray cluster observations.
- The scale of LSS in the local density field as inferred using galaxy distributions and whether this LSS could affect/mimic the dimming observed in the SNIa Hubble diagram.

This has been motivated by the fact that the CMB power spectrum and the SNIa Hubble diagram are both foundational pieces of evidence for the concordance ΛCDM model which makes their rigorous and robust testing essential. In this Chapter we now review our findings on these questions and finish with a brief sketch of a future outlook.

5.1 Main Results

5.1.1 *WMAP* beam profile

In Chapter 2 we examined radio point-sources in the *WMAP* maps. Firstly, we attempted to determine whether the 1-D profile recovered from a stack of these point-sources was consistent with the *WMAP* instrumental beam as inferred using observations of Jupiter. We found for sources from the *Planck* Early Data Release that the profiles in the *WMAP* Q, V and particularly at W bands appear wider than expected when compared to the Jupiter beam, normalised either directly to the radio source profiles or using *Planck* fluxes. We investigated whether this was a selection effect due to the preferential detection of sources on positive CMB fluctuation (an Eddington

bias), using the *WMAP*-CMBfree and NVSS catalogues which should be unaffected by Eddington bias. We found results consistent with those found for the *Planck* sources, implying that Eddington bias was negligible. This conclusion was reinforced by our simulations of the *WMAP* and NVSS source detection which again indicated that Eddington bias is negligible and that in principle the *WMAP* beam could be accurately recovered. We also noted that our matching to and use of the 5GHz source position implied that astrometric errors could not be responsible for the wider beam. Equally, we used the higher resolution of *Planck* to determine that the radio sources we were stacking were genuinely point-like with respect to the *WMAP* beam. Finally, we considered possible explanations for these effects and noted that a timing offset between the *WMAP* astrometric and temperature data as proposed by Liu & Li (2011) resulted in a broadened effective beam, which was in fact consistent with the wider radio source beam we observe. We then proceeded to investigate what effect such a systematic error could have on estimation of the power spectrum. We showed that such effects could indeed be substantial, thus illustrating the importance of systematic errors. However, we also noted that the implied power spectrum was in strong tension with alternative determinations of the CMB power spectrum at high ℓ from ground-based observatories.

5.1.2 *Planck*-*WMAP* flux comparisons

In Chapter 2 we also investigated the accuracy of the *WMAP* flux determination using the *Planck* Early Data Release and ground based observations. We found strong evidence for a non-linear relation in the *WMAP* Q, V and particularly at W bands between *WMAP* and *Planck* and ground-based fluxes. This situation was in contrast to comparisons of *Planck* and the ground-based fluxes where good agreement with linearity was found. We then proceeded to investigate the robustness of our fitting procedure to systematic and random errors. We used jacknife and bootstrap resampling to test whether we were underestimating the error but instead found that our error estimates were in fact appropiate. We also found that the type of flux estimator used was unimportant and hence the flux flux accuracy was not a relevant systematic error. We also investigated whether variability of the sources in conjunction with different

selection sensitivity could explain the non-linearity. We used Monte-Carlo simulations to investigate this but found that our test may be unbiased and that again our error estimates were plausible. We also investigated CO emission in the *Planck* 100GHz band along with the slightly different band-passes between *Planck* and *WMAP* could be responsible for a genuine flux difference. However, we found that the non-linearity was independent of galactic latitude, which implied that CO emission was not a significant factor. We then noted the particular importance for investigating this non-linearity of the five bright sources selected by Weiland et al. (2011) for their low background, lack of variability and history of prior observation. Including these sources in the flux comparison suggested a flux offset rather than a non-linearity. Intriguingly, the size of such an offset is in agreement with the larger beam solid angle we also report. We finished by noting that in either the offset or non-linearity case the faint *WMAP* source fluxes underestimate the *Planck* and other independent flux estimates.

5.1.3 *Planck* SZ clusters

In Chapter 3 we examined the *WMAP* temperature profiles of the SZ clusters reported in the *Planck* Early SZ sample. We described how to invert the fitting template and the integrated SZ signal reported by *Planck* and construct a *WMAP* expected profile. We then tested the validity of this inversion by comparison to the *Planck* temperature profiles reported for Coma, and an X-ray selected sub-sample of the Early SZ sample in Planck Collaboration (2013f) and Planck Collaboration (2013e) respectively. We found acceptable agreement over all angular scales of the profile.

We therefore proceeded to compare the *WMAP* and *Planck* stacked SZ profiles for the Early SZ sample. Contrary to previous reports of a *WMAP* SZ deficit we found that the observed *WMAP* SZ profiles were consistent with those of *Planck*. We therefore reinvestigated these claims of a SZ deficit relative to the X-ray based expectation by studying the temperature profiles of the X-ray clusters of Bonamente et al. (2006). We again found reasonable agreement and hence concluded there is no evidence for a *WMAP* SZ deficit. Although we have no explanation for all reports of such an SZ deficit we were able to attribute some of the claims to a fault assumption regarding the resolution of the cluster.

We also individually investigated the Coma cluster, which is of particular interest because of its relative SZ brightness and large angular scale, where we found evidence for a systematic offset between the *Planck* expectation and the *WMAP* profile. Since the *Planck* SZ signal is estimated from a CMB-free map this scenario is possible if the Coma cluster is centred on $\approx -0.1mK$ downwards CMB fluctuation.

Finally, we studied the effect of the instrumental beam on the recovered SZ profile. Whilst the effect was noticable, particularly in the inner profile, the data was at insufficent S/N to reflect on the wider beam we measured using the radio point-sources.

5.1.4 Galaxy counts and the Local Hole

In Chapter 4 we have examined K and r limited galaxy n(z) and n(m) from 6dFGS/2MASS+SDSS to investigate a proposed local under-density, the `Local Hole'. Comparing galaxy n(z) distributions to homogeneous models in 3 large regions of the sky, we find evidence for $\approx 10-30\%$ under-densities in all 3 regions out to scales of ≈ 150h^{-1}Mpc. Using GAMA to check the galaxy n(K) normalisation at fainter magnitudes we then find evidence for a large-scale $\approx 15\%$ under-density extending to ≈ 300h^{-1}Mpc in the deeper SDSS region. We have further used the redshift data to map peculiar velocities over the same areas using the average redshift-magnitude, $\overline{z}(m)$, technique of Soneira (1979). After accounting for the direct effect of large-scale structure on $\overline{z}(m)$ we can then search for peculiar velocities. Taking all three regions into consideration, the data reject at the $\approx 4\sigma$ level the idea that we have recovered the CMB rest frame in the volume probed. Therefore, there is consistent evidence from galaxy counts and Hubble diagram for a local ≈ 150h^{-1}Mpc mass under-density that deeper counts and redshifts suggest may extend till ≈ 300h^{-1}Mpc.

5.2 Current & Future Outlook

The development of improved instrumentation at the turn of the 20th Century is one of the pivotal factors in the foundation of Cosmology. Indeed, the pattern of improvements to our technology leading to new and enhanced understanding is a common one. In fact, recent observational advances are a good example of this. Over the

last two decades significant developments in multi-object fibre spectrographs have enabled revolutionary deep and wide-field redshift surveys. Complementing this has been the development of digital photometry which has led to the provision of stable and accurate magnitudes. Furthermore, regular access to space missions has enabled the astronomy community to overcome the atmospheric constraints imposed on terrestrial observers. This explosive expansion in the size, richness and availability of astronomical data has been made possible by the exponential growth in computing power and storage capacity. Similarly, the development of the internet and networking has created unprecendented opportunities for collaborative working, data-sharing and dissemination of research. Comprehensive surveys such as SDSS and 2DFGRS and satellites such as *WMAP* and *Planck*, which have been at the forefront of this technological innovation, have provided fundamental advances in our understanding of galaxy evolution and galaxy clustering.

The next decade will undoubtedly see an acceleration of current technological trends. The results of which will be surveys and missions such as the SKA, DES, *Euclid* that will again result in unprecendentedly detailed and large datasets. However, whilst this abundance of data in itself promises further revolutionary progress, it also poses fundamental challenges for the practice of astronomy. It may well be the case that neither instrumentation nor statistical precision will act as the main constraint on further understanding. Instead (and ironically), in the age of `Precision Cosmology' accuracy will be increasingly limited by knowledge of systematic errors rather than precision (Croft & Dailey, 2011; Planck Collaboration, 2013a).

Finally, whilst the concordance ΛCDM model is a superlatively successful, it is also the case that it is in many respects implausible and ill-understood - see Section 1.4. It may well be the case that the further development of the field will be dependent on theoretical innovations that clarifies the model's physical content. This confrontation of Cosmology with fundamental physics promises revolutionary advances in physics and brings us closer to understanding of the Universe's origin and eventual fate.

J. R. Whitbourn

January 16, 2014

Appendix A | *SZ Self Similar Model*

In the self-similar SZ model as employed in the *Planck* ESZ, the fundamental parameters of a cluster are P_{500}, M_{500} and R_{500}. Using the terminology of Arnaud et al. (2010),

$$M_{500} = \frac{4\pi}{3} R_{500}^3 500 \rho_{crit}, \tag{A.1}$$

$$R_{500} = D_a(z) \frac{\theta_{5R_{500}}}{5}. \tag{A.2}$$

A Y_{500} parameter corresponding to these is also defined,

$$Y_{500} = \frac{\sigma_t}{m_e c^2} \frac{4\pi R_{500}^3}{3} P_{500}, \tag{A.3}$$

where P_{500} is the characteristic pressure defined in Arnaud et al. (2010) and Y_{500} can be interpreted as a characteristic integrated SZ signal. In eq. A.3 the units of Y_{500} are Mpc^2, but are easily convertible to the arcmin^2 units used in the ESZ and throughout this paper[1]. This Y_{500} is a distinct quantity from $Y(R_{500})$ as found by evaluating eq. 3.5. The introduction of Y_{500} is well motivated because, as shown by Arnaud et al. (2010), it allows a scale-free description of eq. 3.5's Y_{sph} and Y_{cyl} in terms of $x = R/R_{500}$ as follows,

$$Y_{sph}(x) = Y_{500} I(x), \tag{A.4}$$

$$Y_{cyl}(x) = Y_{sph}(5R_{500}) - Y_{500} J(x). \tag{A.5}$$

where $I(x)$ and $J(x)$ are the spherical and cylindrical scaling functions,

[1] $Y[Mpc^2] = \frac{1}{60^2}(\frac{\pi}{180})^2 (D_a[Mpc])^2 Y[arcmin^2]$.

$$I(x) = \int_0^x 3\mathcal{P}(u)u^2 du, \tag{A.6}$$

$$J(x) = \int_x^5 3\mathcal{P}(u)(u^2 - x^2)^{1/2} u du. \tag{A.7}$$

We therefore find that

$$Y_{cyl}(x) = Y_{500}(I(5) - J(x)). \tag{A.8}$$

Finally, we can use the above to calculate $Y_{cyl}(R)$ and the Compton *y* parameter, where $y(\theta) = \frac{d}{d\Omega} Y_{cyl}(\theta)$. We now describe three methods for doing so.

1. Using $Y(5R_{500})$ as an amplitude: Since $Y_{cyl}(5R_{500}) = Y_{sph}(5R_{500}) = I(5)Y_{500}$, eq. A.8 can be expressed as,

$$Y_{cyl}(R) = Y_{cyl}(5R_{500})\left(1 - \frac{J(x)}{I(5)}\right). \tag{A.9}$$

This is the method we adopt in this paper, it is dependent on both $Y(5R_{500})$ and θ_{5R500}.

2. Using Y_{500} as an amplitude: Y_{500} can be calculated using M_{500} and P_{500}. We can therefore directly evaluate $Y_{cyl}(R)$ using eq. A.8. This method is independent of the *Planck* provided $Y(5R_{500})$ and instead solely uses θ_{5R500}.

3. Avoiding the integrated SZ signal: The Compton y-parameter can be expressed as (Planck Collaboration, 2013e),

$$y(r) = \frac{\sigma_t}{m_e c^2} \int_r^{R_{tot}} \frac{2P(r')r'dr'}{(r'^2 - r^2)^{1/2}}. \tag{A.10}$$

We can therefore directly evaluate the Compton y-parameter if a self-similar cluster profile is assumed for $P(r)$. This method is independent of the *Planck* provided $Y(5R_{500})$ and instead solely uses θ_{5R500}.

Appendix B | *Magnitude Accuracy*

B.1 2MASS k_m_ext

Here we aim to test for scale and zeropoint errors in our 2MASS k_m_ext magnitudes. We therefore compare to the previous galaxy photometry of Loveday (2000) where pseudo-total MAG_BEST magnitudes were measured using SExtractor. In Fig. B.1 we show the resulting comparison after matching the Loveday (2000) galaxies to 2MASS with a $3''$ matching radius.

First, assuming no scale error we find a marginally significant zeropoint offset of k_m_ext-MAG_BEST=0.04 ± 0.02mag. Then we test for non-linearity by fitting for a scale-error using the `*mpfitexy*' routine considering errors in both magnitudes. We find a slope of k_m_ext = (1.05 ± 0.02)MAG_BEST. Whilst this is only significant at the $\approx 2\sigma$ level, we nevertheless applied this correction factor to the k_m_ext magnitude thereby placing the 2MASS data on the Loveday (2000) system. Although this has the effect of slightly steepening the 2MASS counts in Fig. 4.4 the effect on the overall conclusions is negligble.

We further check the 2MASS k_m_ext magnitude by comparing to the 2MASS Kron magnitude (k_m_e) for the Loveday (2000) galaxies in Fig. B.2. Both these 2MASS magnitudes are pseudo-total and so a one-to-one relationship might be expected. First we find a simple offset of k_m_ext-Kron=-0.05 ± 0.01mag. Although this is significant, for this work offsets are less important than scale errors. We test for such a scale error as above and find a slope of k_m_ext = (1.02 ± 0.01)Kron thus the k_m_ext and Kron magnitudes seem reasonably consistent with a one-to-one relation.

We note that in Fig. 4.6 we have not corrected the 2MASS+GAMA magnitudes onto the Loveday (2000) system. This is conservative since the effect would be to imply a slightly higher ($\approx 3\%$) normalisation for our Metcalfe et al. (2001) LF and homogeneous

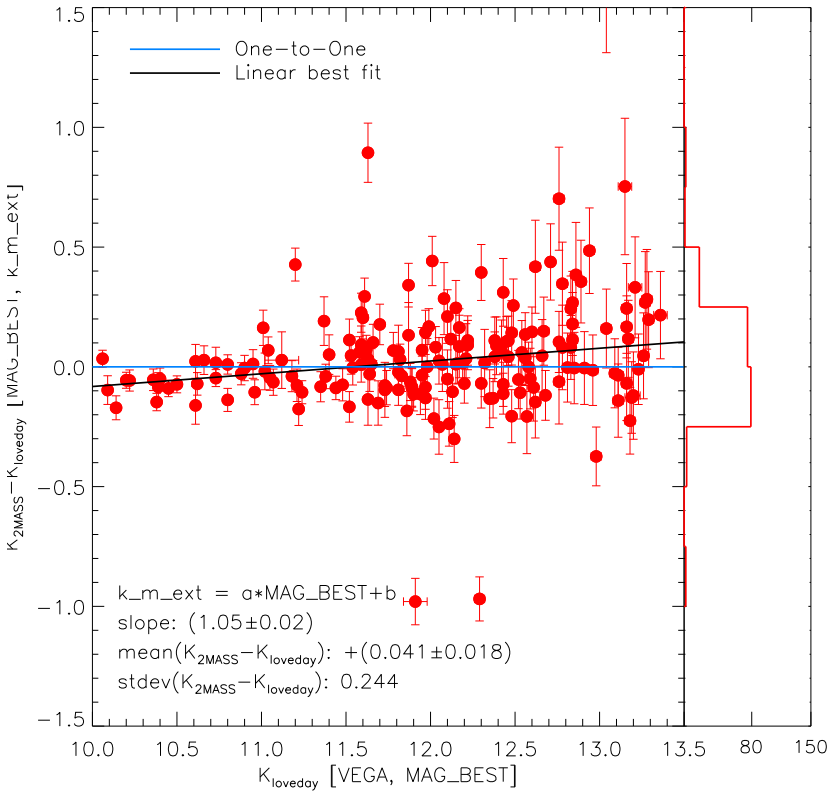

Figure B.1: K band magnitude comparison for 181 common galaxies of the deep K data of Loveday (2000) who have provided the MAG_BEST magnitude from SExtractor to the corresponding 2MASS k_m_ext magnitude. The derived slope using the `*mpfitexy*' routine and both the mean and standard deviation of the residuals are stated.

counts model.

B.2 SDSS cmodel

We now test the SDSS cmodel magnitude using Kron magnitudes from the extended William Herschel Deep Field (WHDF) region Cousins R band data of Metcalfe et al. (2001, 2006). Although some non-linearity is seen in Fig. B.4 this is due to saturation of the WHDF bright magnitudes. In the range $17 < r < 22$ visually there seem little evidence of a scale error and this is confirmed by an analysis using `*mpfitexy*' where we find a slope of r_{cmodel} = $(1.02 \pm 0.01)R_{WHDF}$. If we then assume no scale error we find a simple zeropoint offset of r_{cmodel}-R_{WHDF}=(0.07 ± 0.01)mag. However, for

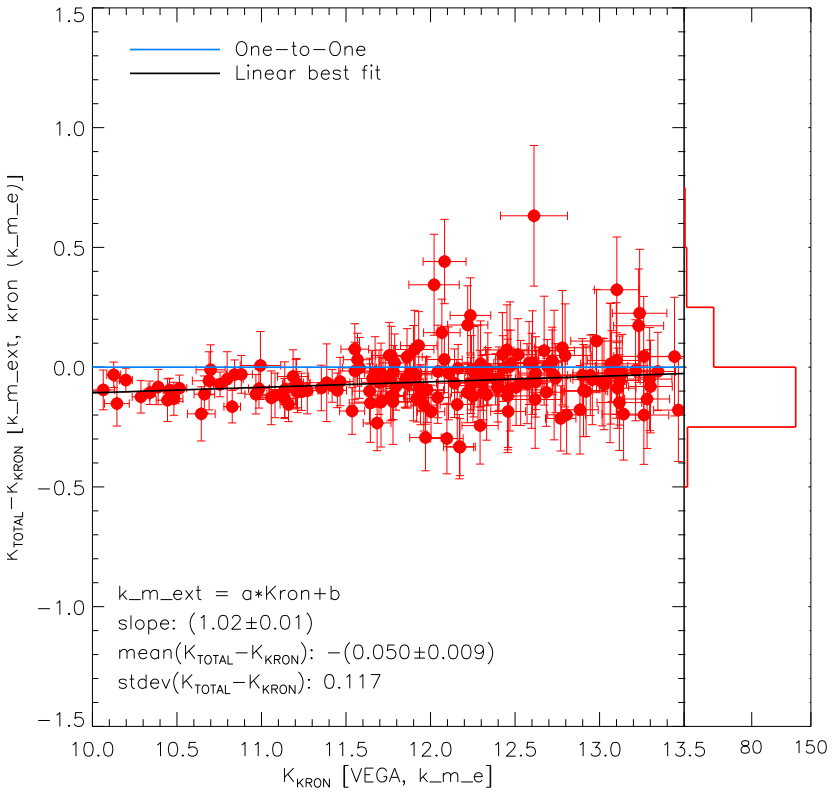

Figure B.2: An internal K band magnitude comparison of the 2MASS k_m_ext and the elliptical Kron (k_m_e) magnitudes for 181 common galaxies of the deep K data of Loveday (2000). The derived slope using the `*mpfitexy*' routine and both the mean and standard deviation of the residuals are stated.

Field	Number	$K_{2MASS} - K_{GAMA}$
G09	567	(-0.02 ± 0.01)
G12	750	(-0.03 ± 0.01)
G15	725	(-0.02 ± 0.01)

Table B.1: A summary of the zeropoint corrections applied to the GAMA data to calibrate onto the 2MASS photometric scale as derived using the `mpfiexy' routine when assuming no scale error.

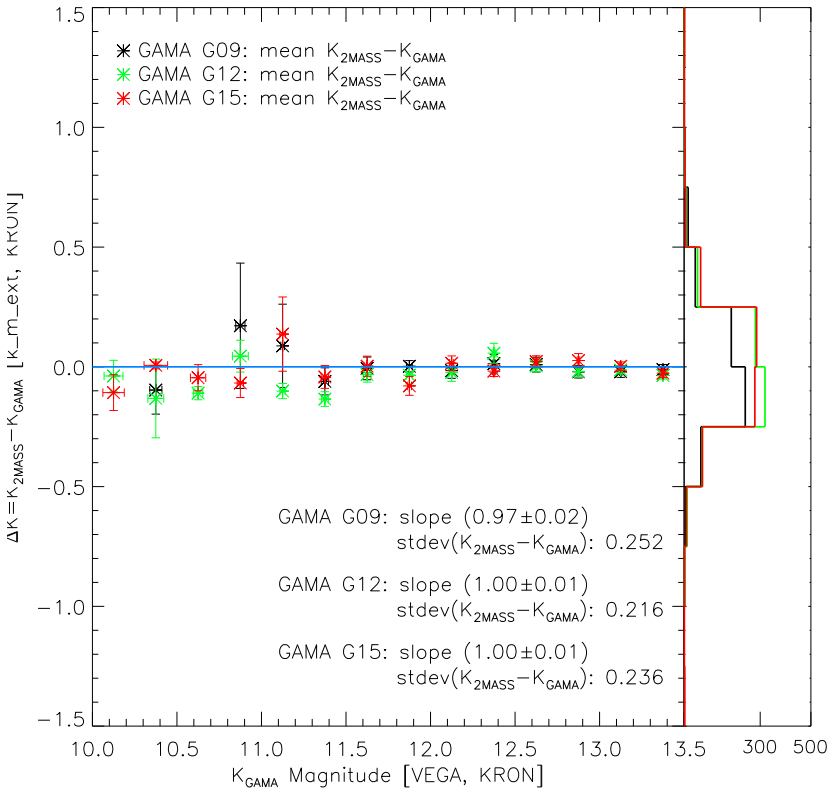

Figure B.3: K band magnitude comparison between GAMA Kron and 2MASS k_m_ext magnitudes over the GAMA regions. The derived slope using the `*mpfitexy*' routine and the standard deviation of the residuals are stated.

the SDSS r band count in Fig. 4.12 we have in fact assumed the larger offset of r_{cmodel}-R_{WHDF}=0.12mag to ensure the counts at $r > 21$ are in agreement with the homogeneous model as might be expected at this depth.

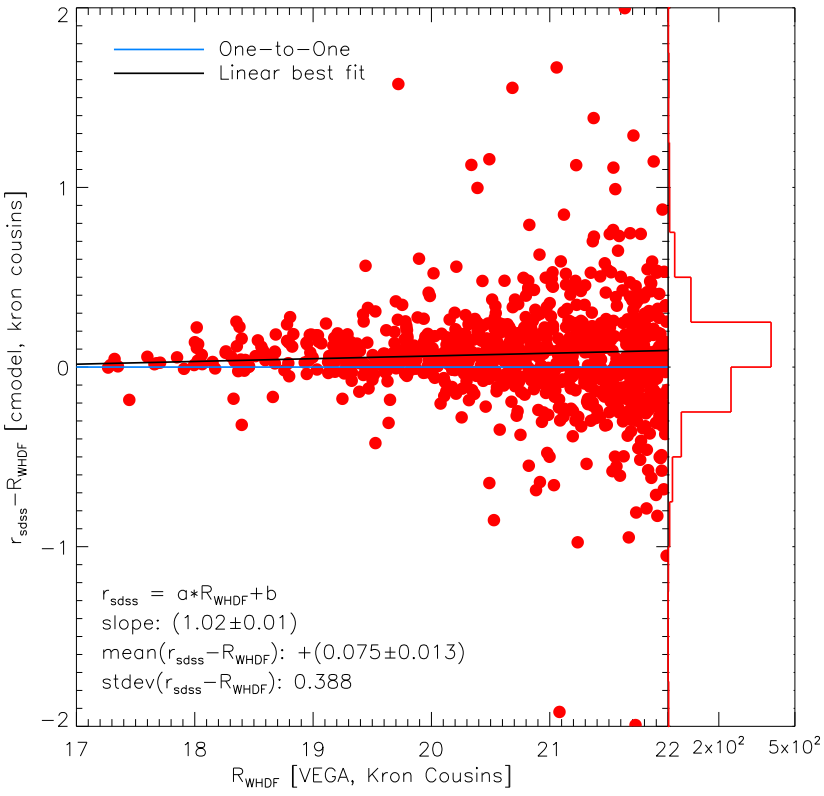

Figure B.4: Magnitude comparison between WHDF Kron Cousins R and SDSS cmodel r over the extended WHDF region. The derived slope using the `*mpfitexy*' routine and both the mean and standard deviation of the residuals are stated.

Appendix C | *Incompleteness effects*

C.1 Photometric Incompleteness

C.1.1 2MASS

2MASS is $\approx 97.5\%$ complete to $K < 13.57$ as described at `http://www.ipac.caltech.edu/2mass/releases/allsky/doc/sec6_1k.html`. Star-galaxy separation for $|b|$ >20deg has been determined by eye to be >99% reliable to at least $K < 12.8$ and only falling to 97% by K=13.5 as outlined at `http://www.ipac.caltech.edu/2mass/releases/allsky/doc/sec6_5b2.html`.

C.1.2 SDSS

The SDSS r band photometric catalogue is magnitude limited to $r < 22.04$ and has been validated by comparison to COMBO-17 as discussed at `http://www.sdss3.org/dr9/imaging/other_info.php#completeness`. Any significant incompleteness is only present at magnitudes r>21 which is far fainter than the scales relevant for studying a local 300h^{-1}Mpc under-density.

Equally, SDSS have studied the validity of their star-galaxy separation relative to COMBO-17 at `http://www.sdss3.org/dr9/imaging/other_info.php#stargalaxy`. Significant issues in classification arise at bright magnitudes $r < 15$ and at faint magnitudes r>20. Only the problem at the bright end is relevant for interpreting the number counts at the Local Hole scales. However, the agreement between the spectroscopically derived $\phi^*(z)$ models and the photometric number counts suggests that star-galaxy separation is not biasing the bright end results.

C.2 Spectroscopic Incompleteness

In Figs. C.2 and C.1 we show respectively the spectroscopic incompleteness of the K and r samples used in this paper. Also reported are the ratios of the total number of spectroscopic to photometric galaxies for each sample. We can see that the incompleteness increases for brighter galaxies, particularly in the case of the r and K band SDSS-NGC samples. This is caused by the relative importance of image artifacts and fibre-constraints for large/bright galaxies in SDSS (McIntosh et al., 2006; Bell et al., 2003).

We first correct the number of galaxies in the data $n(z)$ to the same total as in the corresponding data $n(m)$ by multiplying the data $n(z)$ by the ratio of the total number of photometric to spectroscopic galaxies in each sample. Next, we account for the magnitude dependence of spectroscopic incompleteness in the model $n(z)$ as shown in Figs. C.1 and C.2. We do this by adjusting $\Phi(M)$ using a magnitude dependent completeness factor $f(m)$ in the modelling procedure as in eq. 4.1,

$$\begin{aligned}\Phi(M) &\equiv \Phi(m - 5\log d_L(z) - 25 - K(z) - E(z)), \\ &\rightarrow f(m)\Phi(m - 5\log d_l(z) - 25 - K(z) - E(z)),\end{aligned} \tag{C.1}$$

while conserving galaxy numbers in the model $n(z)$. A similar technique was then applied to correct $\overline{z}(m)$.

Finally, even at the low redshift end the change due to this procedure is less than 1% in the $n(z)$ for both the K and r limited spectroscopic datasets. It is therefore irrelevant for interpreting the density profiles shown in Figs 4.3, 4.8 and 4.10. However, the effect is somewhat more appreciable in $\overline{z}(m)$, especially for the SDSS-NGC K sample where the completeness correction can cause bins to vary by as much as 100 kms^{-1}. This is due to the stronger variations in spectroscopic incompleteness for this sample.

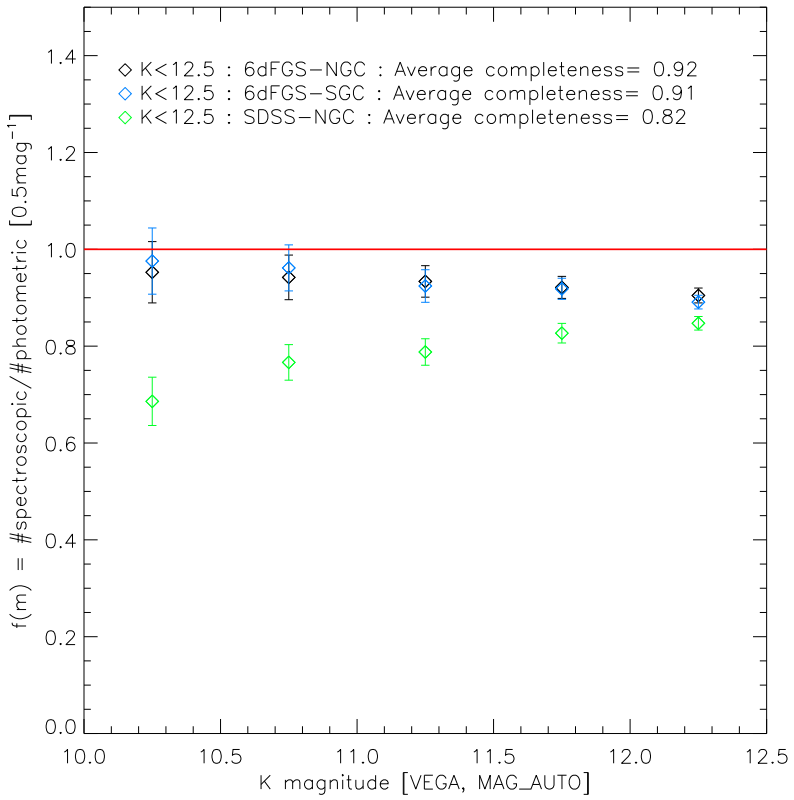

Figure C.1: K band spectroscopic incompleteness as a function of magnitude as derived from the ratio of spectroscopic (6dFGS & SDSS) and photometric (2MASS) number counts with $\delta m = 0.1$. Poisson errors are shown.

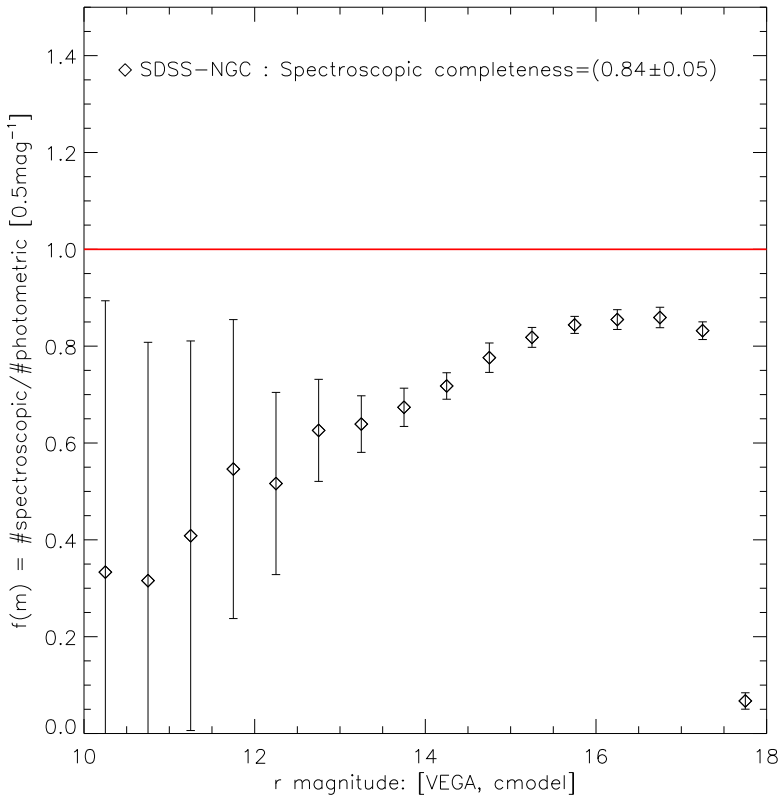

Figure C.2: r band spectroscopic incompleteness as a function of magnitude as derived from the ratio of spectroscopic (SDSS) and photometric (SDSS) number counts with $\delta m = 0.1$. Poisson errors are shown.

Bibliography

Abate, A. & Feldman, H. A. 2012, MNRAS, 419, 3482, http://arxiv.org/abs/1106.5791

Ahn, C. P., Alexandroff, R., Allende Prieto, C., & et al. 2012, ApJS, 203, 21, http://arxiv.org/abs/1207.7137

Arnaud, M., Pratt, G. W., Piffaretti, R., et al. 2010, A&A, 517, A92, http://arxiv.org/abs/0910.1234

Aumont, J., Conversi, L., Thum, C., & et al. 2010, A&A, 514, A70

Bailey, M. E. & Sparks, W. B. 1983, MNRAS, 204, 53P

Barro, G., Gallego, J., Pérez-González, P. G., et al. 2009, A&A, 494, 63, http://arxiv.org/abs/0811.3104

Bell, E. F., McIntosh, D. H., Katz, N., & Weinberg, M. D. 2003, ApJS, 149, 289, http://arxiv.org/abs/arXiv:astro-ph/0302543

Bennett, C. L., Hill, R. S., Hinshaw, G., & et al. 2003, ApJS, 148, 97, http://arxiv.org/abs/arXiv:astro-ph/0302208

Bennett, C. L., Hill, R. S., Hinshaw, G., & et al. 2011, ApJS, 192, 17, http://arxiv.org/abs/1001.4758

Bernardeau, F., Colombi, S., Gaztañaga, E., & Scoccimarro, R. 2002, Phys. Rep., 367, 1, http://arxiv.org/abs/arXiv:astro-ph/0112551

Bertone, G. 2010, Nature, 468, 389, http://arxiv.org/abs/1011.3532

Bertschinger, E. 1998, ARA&A, 36, 599

Bielby, R. M. & Shanks, T. 2007, MNRAS, 382, 1196, http://arxiv.org/abs/arXiv:astro-ph/0703470

Bilicki, M., Chodorowski, M., Jarrett, T., & Mamon, G. A. 2011, ApJ, 741, 31, http://arxiv.org/abs/1102.4356

Biswas, T., Notari, A., & Valkenburg, W. 2010, J. Cosmology Astropart. Phys., 11, 30, http://arxiv.org/abs/1007.3065

Blake, C. & Wall, J. 2002a, Nature, 416, 150, http://arxiv.org/abs/arXiv:astro-ph/0203385

Blake, C. & Wall, J. 2002b, MNRAS, 337, 993, http://arxiv.org/abs/arXiv:astro-ph/0208350

Blanton, M. R. & Roweis, S. 2007, AJ, 133, 734, http://arxiv.org/abs/arXiv:astro-ph/0606170

Bonamente, M., Joy, M. K., LaRoque, S. J., et al. 2006, ApJ, 647, 25, http://arxiv.org/abs/arXiv:astro-ph/0512349

Branchini, E., Davis, M., & Nusser, A. 2012, MNRAS, 424, 472, http://arxiv.org/abs/1202.5206

Bruzual, G. & Charlot, S. 2003, MNRAS, 344, 1000, http://arxiv.org/abs/arXiv:astro-ph/0309134

Busswell, G. S., Shanks, T., Frith, W. J., et al. 2004, MNRAS, 354, 991, http://arxiv.org/abs/arXiv:astro-ph/0302330

Caldwell, R. R. & Stebbins, A. 2008, Physical Review Letters, 100, 191302, http://arxiv.org/abs/0711.3459

Carroll, S. M. 2001, Living Reviews in Relativity, 4

Cavaliere, A. & Fusco-Femiano, R. 1976, A&A, 49, 137

Célérier, M., Bolejko, K., & Krasiński, A. 2010, A&A, 518, A21+, http://arxiv.org/abs/0906.0905

Célérier, M. N. & Thieberger, R. 2005, in 22nd Texas Symposium on Relativistic Astrophysics, ed. P. Chen, E. Bloom, G. Madejski, & V. Patrosian, 364--367

Challinor, A. & Lasenby, A. 1999, ApJ, 513, 1, http://arxiv.org/abs/arXiv:astro-ph/9804301

Chen, X. & Wright, E. L. 2009, ApJ, 694, 222, http://arxiv.org/abs/0809.4025

Chodorowski, M. J., Coiffard, J., Bilicki, M., Colombi, S., & Ciecielag, P. 2008, MNRAS, 389, 717, http://arxiv.org/abs/0706.0619

Clarkson, C., Ellis, G., Faltenbacher, A., et al. 2011, ArXiv e-prints, http://arxiv.org/abs/1109.2484

Clarkson, C. & Maartens, R. 2010, Classical and Quantum Gravity, 27, 124008, http://arxiv.org/abs/1005.2165

Clifton, T. & Zuntz, J. 2009, MNRAS, 400, 2185, http://arxiv.org/abs/0902.0726

Clowe, D., Bradač, M., Gonzalez, A. H., et al. 2006, ApJL, 648, L109, http://arxiv.org/abs/arXiv:astro-ph/0608407

Cole, S., Norberg, P., Baugh, C. M., & et al. 2001, MNRAS, 326, 255, http://arxiv.org/abs/arXiv:astro-ph/0012429

Coles, P. 2003, The Wave Mechanics of Large-Scale Structure, ed. N. G. Sánchez & Y. N. Parijskij (Kluwer Academic Publishers), 219

Colin, J., Mohayaee, R., Sarkar, S., & Shafieloo, A. 2011, MNRAS, 414, 264, http://arxiv.org/abs/1011.6292

Colless, M. a. 2001, MNRAS, 328, 1039, http://arxiv.org/abs/arXiv:astro-ph/0106498

Condon, J. J., Cotton, W. D., Greisen, E. W., et al. 1998, AJ, 115, 1693

Croft, R. A. C. & Dailey, M. 2011, ArXiv e-prints, http://arxiv.org/abs/1112.3108

Cross, N., Driver, S. P., Couch, W., & et al. 2001, MNRAS, 324, 825, http://arxiv.org/abs/arXiv:astro-ph/0012165

Das, S., Louis, T., Nolta, M. R., & et al. 2013, ArXiv e-prints, http://arxiv.org/abs/1301.1037

Driver, S. P., Hill, D. T., Kelvin, L. S., & et al. 2011, MNRAS, 413, 971, http://arxiv.org/abs/1009.0614

Driver, S. P., Norberg, P., Baldry, I. K., & et al. 2009, Astronomy and Geophysics, 50, 050000, http://arxiv.org/abs/0910.5123

Driver, S. P., Windhorst, R. A., Ostrander, E. J., et al. 1995, ApJL, 449, L23+, http://arxiv.org/abs/arXiv:astro-ph/9511132

Eddington, A. S. 1913, MNRAS, 73, 359

Efstathiou, G., Sutherland, W. J., & Maddox, S. J. 1990, Nature, 348, 705

Ellis, G. F. R., Bassett, B. A. C. C., & Dunsby, P. K. S. 1998, Classical and Quantum Gravity, 15, 2345, http://arxiv.org/abs/arXiv:gr-qc/9801092

Erdoğdu, P., Lahav, O., Huchra, J. P., et al. 2006, MNRAS, 373, 45, http://arxiv.org/abs/arXiv:astro-ph/0610005

Famaey, B. & McGaugh, S. S. 2012, Living Reviews in Relativity, 15, 10, http://arxiv.org/abs/1112.3960

February, S., Larena, J., Smith, M., & Clarkson, C. 2010, MNRAS, 405, 2231, http://arxiv.org/abs/0909.1479

Feindt, U., Kerschhaggl, M., Kowalski, M., & et al. 2013, ArXiv e-prints, http://arxiv.org/abs/1310.4184

Feldman, H. A., Watkins, R., & Hudson, M. J. 2010, MNRAS, 407, 2328, http://arxiv.org/abs/0911.5516

Finlator, K. & et al. 2000, AJ, 120, 2615, http://arxiv.org/abs/arXiv:astro-ph/0010052

Fixsen, D. J., Hinshaw, G., Bennett, C. L., & Mather, J. C. 1997, ApJ, 486, 623, http://arxiv.org/abs/arXiv:astro-ph/9704176

Foreman, S., Moss, A., Zibin, J. P., & Scott, D. 2010, ArXiv e-prints, http://arxiv.org/abs/1009.0273

Frith, W. J., Busswell, G. S., Fong, R., Metcalfe, N., & Shanks, T. 2003, MNRAS, 345, 1049, http://arxiv.org/abs/arXiv:astro-ph/0302331

Frith, W. J., Metcalfe, N., & Shanks, T. 2006, MNRAS, 371, 1601, http://arxiv.org/abs/arXiv:astro-ph/0509875

Frith, W. J., Outram, P. J., & Shanks, T. 2005a, in Astronomical Society of the Pacific Conference Series, Vol. 329, Nearby Large-Scale Structures and the Zone of Avoidance, ed. A. P. Fairall & P. A. Woudt, 49--+

Frith, W. J., Shanks, T., & Outram, P. J. 2005b, MNRAS, 361, 701, http://arxiv.org/abs/arXiv:astro-ph/0411204

Gibelyou, C. & Huterer, D. 2012, MNRAS, 427, 1994, http://arxiv.org/abs/1205.6476

Glazebrook, K., Ellis, R., Santiago, B., & Griffiths, R. 1995, MNRAS, 275, L19, http://arxiv.org/abs/arXiv:astro-ph/9503101

Gold, B., Odegard, N., Weiland, J. L., & et al. 2011, ApJS, 192, 15, http://arxiv.org/abs/1001.4555

Goodman, J. 1995, PhRvD, 52, 1821, http://arxiv.org/abs/arXiv:astro-ph/9506068

Gott, III, J. R., Jurić, M., Schlegel, D., et al. 2005, ApJ, 624, 463, http://arxiv.org/abs/arXiv:astro-ph/0310571

Granett, B. R., Neyrinck, M. C., & Szapudi, I. 2008, ApJL, 683, L99, http://arxiv.org/abs/0805.3695

Gregory, P. C., Scott, W. K., Douglas, K., & Condon, J. J. 1996, ApJS, 103, 427

Griffith, M. R. & Wright, A. E. 1993, AJ, 105, 1666

Hajian, A., Acquaviva, V., Ade, P. A. R., & et al. 2011, ApJ, 740, 86, http://arxiv.org/abs/1009.0777

Heavens, A. 2008, Journal of Physics Conference Series, 120, 022001

Heavens, A. F., Jimenez, R., & Maartens, R. 2011, J. Cosmology Astropart. Phys., 9, 35, http://arxiv.org/abs/1107.5910

Hill, D. T., Kelvin, L. S., Driver, S. P., & et al. 2011, MNRAS, 412, 765, http://arxiv.org/abs/1009.0615

Hill, M. D. & Shanks, T. 2010, ArXiv e-prints, http://arxiv.org/abs/1007.3126

Hill, R. S., Weiland, J. L., Odegard, N., et al. 2009, ApJS, 180, 246, http://arxiv.org/abs/0803.0570

Hinshaw, G., Spergel, D. N., Verde, L., & et al. 2003, ApJS, 148, 135, http://arxiv.org/abs/arXiv:astro-ph/0302217

Hogg, D. W., Eisenstein, D. J., Blanton, M. R., et al. 2005, ApJ, 624, 54, http://arxiv.org/abs/arXiv:astro-ph/0411197

Hoyle, B., Tojeiro, R., Jimenez, R., et al. 2013, ApJL, 762, L9, http://arxiv.org/abs/1209.6181

Hu, W. & Dodelson, S. 2002, ARA&A, 40, 171, http://arxiv.org/abs/arXiv:astro-ph/0110414

Huchra, J. P., Macri, L. M., Masters, K. L., & et al. 2012, ApJS, 199, 26, http://arxiv.org/abs/1108.0669

Jaffe, A. H. 2010, Bayesian analysis of cosmic microwave background data, ed. M. P. Hobson, A. H. Jaffe, A. R. Liddle, P. Mukeherjee, & D. Parkinson, 229

Jarosik, N., Bennett, C. L., Dunkley, J., & et al. 2011, ApJS, 192, 14, http://arxiv.org/abs/1001.4744

Jarosik, N., Bennett, C. L., Halpern, M., & et al. 2003, ApJS, 145, 413, http://arxiv.org/abs/arXiv:astro-ph/0301164

Jarrett, T. H., Chester, T., Cutri, R., Schneider, S. E., & Huchra, J. P. 2003, AJ, 125, 525

Jha, S., Riess, A. G., & Kirshner, R. P. 2007, ApJ, 659, 122, http://arxiv.org/abs/astro-ph/0612666

Jones, D. H., Read, M. A., Saunders, W., Colless, M., & et al. 2009, MNRAS, 399, 683, http://arxiv.org/abs/0903.5451

Jones, D. H., Saunders, W., Colless, M., Read, M. A., & et al. 2004, MNRAS, 355, 747, http://arxiv.org/abs/arXiv:astro-ph/0403501

Kalus, B., Schwarz, D. J., Seikel, M., & Wiegand, A. 2013, A&A, 553, A56, http://arxiv.org/abs/1212.3691

Karachentsev, I. D. & Makarov, D. A. 1996, AJ, 111, 794

Kashlinsky, A., Atrio-Barandela, F., Kocevski, D., & Ebeling, H. 2008, ApJL, 686, L49, http://arxiv.org/abs/0809.3734

Keenan, R. C., Barger, A. J., & Cowie, L. L. 2013, ApJ, 775, 62, http://arxiv.org/abs/1304.2884

Keenan, R. C., Barger, A. J., Cowie, L. L., et al. 2012, ApJ, 754, 131, http://arxiv.org/abs/1207.1588

Keenan, R. C., Trouille, L., Barger, A. J., Cowie, L. L., & Wang, W. 2010, ApJS, 186, 94, http://arxiv.org/abs/0912.3090

Keisler, R. 2009, ApJL, 707, L42, http://arxiv.org/abs/0910.4233

Keisler, R., Reichardt, C. L., Aird, K. A., & et al. 2011, ApJ, 743, 28, http://arxiv.org/abs/1105.3182

Kibble, T. W. B. & Lieu, R. 2005, ApJ, 632, 718, http://arxiv.org/abs/arXiv:astro-ph/0412275

Komatsu, E., Smith, K. M., Dunkley, J., & et al. 2011, ApJS, 192, 18, http://arxiv.org/abs/1001.4538

Kostov, V. 2010, J. Cosmology Astropart. Phys., 4, http://arxiv.org/abs/1002.3408

Krasiński, A. 2013, ArXiv e-prints, http://arxiv.org/abs/1309.4368

Labini, F. S. 2010, in American Institute of Physics Conference Series, Vol. 1241, American Institute of Physics Conference Series, ed. J.-M. Alimi & A. Fuözfa, 981--990

Lavaux, G., Afshordi, N., & Hudson, M. J. 2013, MNRAS, 430, 1617, http://arxiv.org/abs/1207.1721

Lieu, R., Mittaz, J. P. D., & Zhang, S.-N. 2006, ApJ, 648, 176, http://arxiv.org/abs/arXiv:astro-ph/0510160

Limon, M. 2009, Wilkinson Microwave Anisotropy Probe (*WMAP*): Five Year Explanatory Supplement, http://lambda.gsfc.nasa.gov/product/map/dr3/pub_papers/fiveyear/supplement/WMAP_supplement.pdf [Online; accessed 14-September-2013]

Liske, J., Lemon, D. J., Driver, S. P., & et al. 2003, MNRAS, 344, 307, http://arxiv.org/abs/arXiv:astro-ph/0207555

Liu, H. & Li, T.-P. 2011, ApJ, 732, 125, http://arxiv.org/abs/1101.2720

Lonsdale, C. J., Doeleman, S. S., & Phillips, R. B. 1998, AJ, 116, 8

Loveday, J. 2000, MNRAS, 312, 557, http://arxiv.org/abs/arXiv:astro-ph/9907179

Maartens, R. 2011, Royal Society of London Philosophical Transactions Series A, 369, 5115, http://arxiv.org/abs/1104.1300

Macías-Pérez, J. F., Mayet, F., Aumont, J., & Désert, F.-X. 2010, ApJ, 711, 417, http://arxiv.org/abs/0802.0412

Maddox, S. J., Efstathiou, G., Sutherland, W. J., & Loveday, J. 1990, MNRAS, 243, 692

Malik, P. 2011, MPhys Thesis, http://etheses.dur.ac.uk/4449/ [Online; accessed 14-September-2013]

Marra, V., Amendola, L., Sawicki, I., & Valkenburg, W. 2013, Physical Review Letters, 110, 241305, http://arxiv.org/abs/1303.3121

Mather, J. C., Cheng, E. S., Cottingham, D. A., & et al. 1994, ApJ, 420, 439

McIntosh, D. H., Bell, E. F., Weinberg, M. D., & Katz, N. 2006, MNRAS, 373, 1321, http://arxiv.org/abs/arXiv:astro-ph/0511737

Melin, J.-B., Bartlett, J. G., & Delabrouille, J. 2006, A&A, 459, 341, http://arxiv.org/abs/arXiv:astro-ph/0602424

Melin, J.-B., Bartlett, J. G., Delabrouille, J., et al. 2011, A&A, 525, A139, http://arxiv.org/abs/1001.0871

Metcalfe, N., Shanks, T., Campos, A., Fong, R., & Gardner, J. P. 1996, Nature, 383, 236, http://arxiv.org/abs/arXiv:astro-ph/9609121

Metcalfe, N., Shanks, T., Campos, A., McCracken, H. J., & Fong, R. 2001, MNRAS, 323, 795, http://arxiv.org/abs/arXiv:astro-ph/0010153

Metcalfe, N., Shanks, T., Weilbacher, P. M., et al. 2006, MNRAS, 370, 1257

Moffat, J. W. 2009, ArXiv e-prints, http://arxiv.org/abs/0910.2723

Moss, A., Scott, D., & Sigurdson, K. 2011a, J. Cosmology Astropart. Phys., 1, 1, http://arxiv.org/abs/1004.3995

Moss, A., Zibin, J. P., & Scott, D. 2011b, PhRvD, 83, 103515, http://arxiv.org/abs/1007.3725

Mroczkowski, T., Bonamente, M., Carlstrom, J. E., & et al. 2009, ApJ, 694, 1034, http://arxiv.org/abs/0809.5077

Murphy, D. N. A., Eke, V. R., & Frenk, C. S. 2011, MNRAS, 413, 2288, http://arxiv.org/abs/1010.2202

Myers, A. D., Shanks, T., Outram, P. J., Frith, W. J., & Wolfendale, A. W. 2004, MNRAS, 347, L67, http://arxiv.org/abs/arXiv:astro-ph/0306180

Nadathur, S. & Sarkar, S. 2011, PhRvD, 83, 063506, http://arxiv.org/abs/1012.3460

Nagai, D., Vikhlinin, A., & Kravtsov, A. V. 2007, ApJ, 655, 98, http://arxiv.org/abs/arXiv:astro-ph/0609247

Nolta, M. R., Wright, E. L., Page, L., & et al. 2004, ApJ, 608, 10, http://arxiv.org/abs/arXiv:astro-ph/0305097

Nusser, A., Branchini, E., & Davis, M. 2011, ApJ, 735, 77, http://arxiv.org/abs/1102.4189

Osborne, S. J., Mak, D. S. Y., Church, S. E., & Pierpaoli, E. 2011, ApJ, 737, 98, http://arxiv.org/abs/1011.2781

Ostriker, J. P. & Steinhardt, P. J. 1995, ArXiv Astrophysics e-prints, http://arxiv.org/abs/arXiv:astro-ph/9505066

Page, L., Barnes, C., Hinshaw, G., et al. 2003a, ApJS, 148, 39, http://arxiv.org/abs/arXiv:astro-ph/0302214

Page, L., Jackson, C., Barnes, C., & et al. 2003b, ApJ, 585, 566, http://arxiv.org/abs/arXiv:astro-ph/0301160

Park, C., Choi, Y.-Y., Kim, J., et al. 2012, ApJL, 759, L7, http://arxiv.org/abs/1209.5659

Peacock, J. A. 1999, Cosmological Physics

Peacock, J. A. 2013, in Astronomical Society of the Pacific Conference Series, Vol. 471, Origins of the Expanding Universe: 1912-1932, ed. M. J. Way & D. Hunter, 3

Peebles, P. J. E. 1993, Principles of physical cosmology, ed. Peebles, P. J. E.

Peebles, P. J. E. & Nusser, A. 2010, Nature, 465, 565, http://arxiv.org/abs/1001.1484

Perlmutter, S., Aldering, G., Goldhaber, G., & et al. 1999, ApJ, 517, 565, http://arxiv.org/abs/arXiv:astro-ph/9812133

Piffaretti, R., Jetzer, P., Kaastra, J. S., & Tamura, T. 2005, A&A, 433, 101, http://arxiv.org/abs/arXiv:astro-ph/0412233

Planck Collaboration. 2011a, Explanatory Supplement to the Planck Early Release Compact Source Catalogue, http://www.sciops.esa.int/SA/PLANCK/docs/ERCSC_explanatory_supplement.pdf [Online; accessed 14-September-2013]

Planck Collaboration. 2011b, A&A, 536, A8, http://arxiv.org/abs/1101.2024

Planck Collaboration. 2011c, A&A, 536, A10, http://arxiv.org/abs/1101.2043

Planck Collaboration. 2011d, A&A, 536, A11, http://arxiv.org/abs/1101.2026

Planck Collaboration. 2013a, ArXiv e-prints, http://arxiv.org/abs/1303.5062

Planck Collaboration. 2013b, ArXiv e-prints, http://arxiv.org/abs/1303.5075

Planck Collaboration. 2013c, ArXiv e-prints, http://arxiv.org/abs/1303.5076

Planck Collaboration. 2013d, ArXiv e-prints, http://arxiv.org/abs/1303.5083

Planck Collaboration. 2013e, A&A, 550, A131, http://arxiv.org/abs/1207.4061

Planck Collaboration. 2013f, A&A, 554, A140, http://arxiv.org/abs/1208.3611

Pratt, G. W., Böhringer, H., Croston, J. H., et al. 2007, A&A, 461, 71, http://arxiv.org/abs/arXiv:astro-ph/0609480

Press, W. H., Teukolsky, S. A., Vetterling, W. T., & Flannery, B. P. 1992, Numerical recipes in FORTRAN. The art of scientific computing

Primack, J. R. 2009, in American Institute of Physics Conference Series, Vol. 1166, American Institute of Physics Conference Series, ed. D. B. Cline, 3--9

Refregier, A., Spergel, D. N., & Herbig, T. 2000, ApJ, 531, 31, http://arxiv.org/abs/arXiv:astro-ph/9806349

Regis, M. & Clarkson, C. 2012, General Relativity and Gravitation, 44, 567, http://arxiv.org/abs/1003.1043

Rood, H. J. 1988, ARA&A, 26, 245

Rose, H. G. 2001, ApJL, 560, L15, http://arxiv.org/abs/arXiv:astro-ph/0106489

Roukema, B. F. 2010, A&A, 518, A34, http://arxiv.org/abs/1004.4506

Sarkar, P., Yadav, J., Pandey, B., & Bharadwaj, S. 2009, MNRAS, 399, L128, http://arxiv.org/abs/0906.3431

Sawangwit, U. 2011, PhD thesis, Durham University, http://etheses.dur.ac.uk/3280/ [Online; accessed 14-September-2013]

Sawangwit, U. & Shanks, T. 2010a, MNRAS, 407, L16, http://arxiv.org/abs/0912.0524

Sawangwit, U. & Shanks, T. 2010b, ArXiv e-prints, http://arxiv.org/abs/1006.1270

Sawangwit, U., Shanks, T., Cannon, R. D., et al. 2010, MNRAS, 402, 2228, http://arxiv.org/abs/0911.1352

Schechter, P. 1976, ApJ, 203, 297

Schlegel, D. J., Finkbeiner, D. P., & Davis, M. 1998, ApJ, 500, 525, http://arxiv.org/abs/arXiv:astro-ph/9710327

Schmidt, B. P., Suntzeff, N. B., Phillips, M. M., & et al. 1998, ApJ, 507, 46, http://arxiv.org/abs/arXiv:astro-ph/9805200

Schultz, K. W. & Huffenberger, K. M. 2012, MNRAS, 424, 3028, http://arxiv.org/abs/1111.7311

Schwarz, D. J. 2010, ArXiv e-prints, http://arxiv.org/abs/1003.3026

Scrimgeour, M. I., Davis, T., Blake, C., James, & et al. 2012, MNRAS, 425, 116, http://arxiv.org/abs/1205.6812

Seljak, U. & Zaldarriaga, M. 1996, ApJ, 469, 437, http://arxiv.org/abs/arXiv:astro-ph/9603033

Shanks, T., Stevenson, P. R. F., Fong, R., & MacGillivray, H. T. 1984, MNRAS, 206, 767

Skrutskie, M. F., Cutri, R. M., Stiening, R., & et al. 2006, AJ, 131, 1163

Soneira, R. M. 1979, ApJL, 230, L63

Strauss, M. A., Weinberg, D. H., Lupton, R. H., & et al. 2002, AJ, 124, 1810, http://arxiv.org/abs/arXiv:astro-ph/0206225

Strauss, M. A. & Willick, J. A. 1995, Phys. Rep., 261, 271, http://arxiv.org/abs/arXiv:astro-ph/9502079

Sunyaev, R. A. & Zeldovich, I. B. 1980, ARA&A, 18, 537

Szapudi, I., Pan, J., Prunet, S., & Budavári, T. 2005, ApJL, 631, L1, http://arxiv.org/abs/arXiv:astro-ph/0505389

Szapudi, I., Prunet, S., & Colombi, S. 2001, ApJL, 561, L11

Tegmark, M. & de Oliveira-Costa, A. 1998, ApJL, 500, L83, http://arxiv.org/abs/arXiv:astro-ph/9802123

Trimble, V. 2013, ArXiv e-prints, http://arxiv.org/abs/1307.2289

Watkins, R., Feldman, H. A., & Hudson, M. J. 2009, MNRAS, 392, 743, http://arxiv.org/abs/0809.4041

Watson, W. A., Iliev, I. T., Diego, J. M., et al. 2013, ArXiv e-prints, http://arxiv.org/abs/1305.1976

Weiland, J. L., Odegard, N., Hill, R. S., & et al. 2011, ApJS, 192, 19, http://arxiv.org/abs/1001.4731

Weinberg, S. 1976, ApJL, 208, L1

Whitbourn, J. R. & Shanks, T. 2013, The galaxy luminosity function and the Local Hole, in preparation.

Witten, E. 2001, ArXiv High Energy Physics - Theory e-prints, http://arxiv.org/abs/arXiv:hep-th/0106109

Wojtak, R., Knebe, A., Watson, W. A., et al. 2013, ArXiv e-prints, http://arxiv.org/abs/1312.0276

Wright, E. L. 2004, Measuring and Modeling the Universe, 291, http://arxiv.org/abs/arXiv:astro-ph/0305591

Wright, E. L., Chen, X., Odegard, N., & et al. 2009, ApJS, 180, 283, http://arxiv.org/abs/0803.0577

Wright, E. L., Meyer, S. S., Bennett, C. L., & et al. 1992, ApJL, 396, L13

Wright, M. C. H. & Sault, R. J. 1993, ApJ, 402, 546

Yadav, J. K., Bagla, J. S., & Khandai, N. 2010, MNRAS, 405, 2009, http://arxiv.org/abs/1001.0617

Yao, W.-M., Amsler, C., Asner, D., & et al. 2006, Journal of Physics G Nuclear Physics, 33, 1, http://arxiv.org/abs/arXiv:astro-ph/0601168

Yasuda, N., Fukugita, M., Narayanan, V. K., & et al. 2001, AJ, 122, 1104, http://arxiv.org/abs/arXiv:astro-ph/0105545

York, D. G., Adelman, J., Anderson, Jr., J. E., & et al. 2000, AJ, 120, 1579, http://arxiv.org/abs/arXiv:astro-ph/0006396

Zehavi, I., Riess, A. G., Kirshner, R. P., & Dekel, A. 1998, ApJ, 503, 483, http://arxiv.org/abs/astro-ph/9802252

Zwicky, F. 1933, Helvetica Physica Acta, 6, 110